ICE, CLOUD, and Land Elevation Satellite (ICESat-2) Project

Algorithm Theoretical Basis Document (ATBD) For Sea Ice Products

Ron Kwok
Alek Petty
Jesse T. Wimert
Marco Bagnardi
Glenn F. Cunningham
David W. Hancock
Alvaro Ivanoff
Nathan Kurtz

October 30, 2021

National Aeronautics and Space Administration

Goddard Space Flight Center
Greenbelt, Maryland

Abstract

This document describes the theoretical basis of the sea ice processing algorithms and the products that are produced by the ICESat-2 mission. It includes descriptions of the parameters that are provided with each product as well as ancillary geophysical parameters used in the derivation of the along-track and gridded sea ice products.

CM Foreword

This document is an Ice, Cloud, and Land Elevation (ICESat-2) Project Science Office controlled document. Changes to this document require prior approval of the Science Development Team ATBD Lead or designee. Proposed changes shall be submitted in the ICESat-II Management Information System (MIS) via a Signature Controlled Request (SCoRe), along with supportive material justifying the proposed change.
Questions or comments concerning this document should be addressed to:
ICESat-2 Project Science Office
Mail Stop 615
Goddard Space Flight Center
Greenbelt, Maryland 20771

Preface

This document is the Algorithm Theoretical Basis Document for the processing of sea ice data to be implemented at the ICESat-2 Science Investigator-led Processing System (SIPS). The SIPS supports the ATLAS (Advanced Topographic Laser Altimeter System) instrument on the ICESat-2 Spacecraft and encompasses the ATLAS Science Algorithm Software (ASAS) and the Scheduling and Data Management System (SDMS). The science algorithm software will produce Level 0 through Level 4 standard data products as well as the associated product quality assessments and metadata information.

The ICESat-2 Science Development Team, in support of the ICESat-2 Project Science Office (PSO), assumes responsibility for this document and updates it, as required, as algorithms are refined or to meet the needs of the ICESat-2 SIPS. Reviews of this document are performed when appropriate and as needed updates to this document are made. Changes to this document will be made by complete revision.

Changes to this document require prior approval of the Change Authority listed on the signature page. Proposed changes shall be submitted to the ICESat-2 PSO, along with supportive material justifying the proposed change.

Questions or comments concerning this document should be addressed to:

Thomas Neumann, ICESat-2 Project Scientist
Mail Stop 615
Goddard Space Flight Center
Greenbelt, Maryland 20771

Review/Approval Page

Prepared by:

Ron Kwok
Jet Propulsion Laboratory
California Institute of Technology
Pasadena, CA 91109

Alek Petty (since July 2020)
Mail Stop 615
Goddard Space Flight Center
Greenbelt, Maryland 20771

Reviewed by:

<Enter Position Title Here>
<Enter Org/Code Here>

<Enter Position Title Here>
<Enter Org/Code Here>

Approved by:

Thomas Neumann
ICESat-2 Project Scientist
Mail Stop 615
Goddard Space Flight Center
Greenbelt, Maryland 20771

Change History Log

Revision Level	Description of Change	SCoRe No.	Date Approved
1.0	Initial Release		
4.0 (ATL07)	Confirmed that invalid parameters from ATL03 and ATL09 are properly marked, including ocean tides. If an invalid is found, the average for the segment is now set to invalid. The meteorological data from ATL09 for the weak beam has now been properly aligned with the strong beam by using distance instead of time. Dynamically convert MSS values to the tide-free system. Dynamically adjust sea ice coarse track height filters for the tide-free system. *Explanation: moving everything to tide-free system for consistency.* Read free2mean parameters from ATL03, average to sea ice segment rate, and write to ATL07. Fixed error in calculation of sea ice segment length to correctly measure length and remove negative results. Fixed error in the computation of first photon bias.		01/19/2020
4.0 (ATL10)	Calculate freeboard beam along-track slope for ATL10 to be used as a possible filter. The default value of the controllable parameter height_segment_fit_quality_flag_max was updated to 4 (previously set to 3) to reduce amount of filtering. The default upper and lower bounds of the reference surface and ht_thresh2 have been updated to match the release 004 ATL07/10 ATBD.		01/19/2020

	Creating consistency between the permanent tide system for the MSS, geoid, and height data products by placing everything into the tide free system. Updated the product descriptions for geoid and solid Earth tide to reference mean-tide or free-tide, appropriately. Additionally, the ATL10 template has been updated to include descriptions that the affected parameters are now in the tide-free system. The free-to-mean conversions for geoid, MSS and solid Earth tide are added and passed through from ATL07.		
5.0 (ATL07)	The PODPPD flag has been added to the ATL07 product, and is now used to filter heights during 'degraded' geolocation periods of calibration scans. A max_incidence_angle filter was implemented and added as a controllable override. If beam incidence angle exceeds max_incidence_angle, the segment surface type will be set to -1 (photon rates are impacted by off-pointing). A contrast filter has been implemented, but turned off by default. Two new controllable parameters have been added. A new parameter height_segment_n_pulse_seg_used has been added to ATL07 product. This parameter excludes the number of specular returns filtered out of processing, unlike height_segment_n_pulse_seg. New parameters of mean ocean sea level pressure and dynamic inverted barometer effect are calculated in ATL07. These are not currently applied to the heights but could be included in future releases.		07/16/2021

5.0 (ATL10)	The MSS, Geoid, and the two free-to-mean parameters have been calculated at the reference surface-scale and added to ATL10. The along track distance has been calculated and added to the reference surface and lead groups. The reference surface time and location has been updated to be set to the center of the reference surface. Previously, the location was found by simply averaging data from all the segments within the 10km sections which caused some odd behavior (skewed locations towards the sides of the sections). The reference surface lat/lon/time is now determined using interpolation. For reference surfaces set where there are no sea ice segments for a given beam, a filling procedure is used to estimate the reference surface lat/lon by. The filling procedure uses a distance routine to find the lat/lon of a point a given distance from a known point, in a known direction. The new PODPPD flag, and updated segment_type flag, are read from ATL07 and used in filtering which sea ice segments are used in freeboard processing. Now if there is a calibration scan maneuver occurring (degraded or nominal), the freeboard segment in ATL10 is invalidated. In ATL07 a new invalidated surface segment type classification (-1) was introduced during off-pointing (>1 degree) which is also used to invalidate the freeboard segment. The height segment inverted barometer variable was moved to the geophysical group from the height segments group (it was already in the geophysical group in ATL07). The ATL10 QA check for insufficient output failure was updated. The code now checks for the number of valid freeboard ice segments and number of valid, un-interpolated, reference surfaces. Previously, the total number of freeboard ice segments written (valid and invalid) were counted, and number of reference surfaces was not considered. A new controllable parameter, *min_refsurf_count*, was added to control the minimum reference surface count threshold (l3a_fb_const_mod).		07/16/2021

	Read in the new mean ocean sea level pressure (one value for each granule) and dynamic inverted barometer from ATL07.		

List of TBDs/TBRs

Item No.	Location	Summary	Ind./Org.	Due Date

Table of Contents

Abstract iii
CM Foreword iv
Preface vi
Review/Approval Page vii
Change History Log viii
List of TBDs/TBRs ix
Table of Contents xiii
List of Figures xvi
List of Tables xviii
1 INTRODUCTION 1
2 BACKGROUND 2
2.1 Overview: sea ice freeboard and thickness 2
2.2 Photon counting altimetry over sea ice 5
2.2.1 Expected ATLAS performance over sea ice 6
2.2.2 Signal vs. background photons: Examples from MABEL 6
2.2.3 Sea ice in two MABEL file-segments 9
2.2.4 Height distributions 10
2.2.5 Potential error sources 11
3 SEA ICE PRODUCTS 16
3.1 Surface height product (ATL07/L3A) 17
3.1.1 Height segments 17
3.1.2 Parameters in a height segment 17
3.1.3 Input from IS-2 Products (ATL03 and ATL09) 18
3.1.4 External inputs (see Section 7) 19
3.2 Sea Ice Freeboard (ATL10/L3A) 21
3.2.1 Sampling (Swath-segment) 21
3.2.2 Parameters in a freeboard swath-segment 21
3.2.3 External input (see Section 7) 21
3.3 Gridded Sea Ice Freeboard (ATL20/L3B) 23
3.3.1 Grid Parameters 23
3.3.2 External input 23
3.4 Gridded Sea Surface Height - Ice-covered Ocean (ATL21/L3B) 23
3.4.1 Grid Parameters 23
3.4.2 External input 23
4 ALGORITHM DESCRIPTION: ATL07 24
4.1 Input parameters 26
4.1.1 Source: ATL03 26
4.1.2 Source: ATL09 27
4.1.3 External (time-varying/static fields - see Section 7) 28
4.2 Finding the surface 28
4.2.1 Coarse surface-finding 29
4.2.2 Fine surface-finding: Fitting the expected return to the photon cloud 32
4.2.3 Background rates (MHz) 39
4.2.4 Surface height histogram statistics and height quality estimates 40
4.2.5 Expected uncertainties in retrieved surface height 42
4.2.6 Correction for skews in the surface height distributions 44
4.2.7 Variability in the system impulse response 47
4.2.8 First-photon bias 47

4.3 Surface classification (Ice/water discrimination) ... 48
4.3.1 Basis for surface classification ... 48
4.4 Output of surface finding algorithm ... 54
5 ALGORITHM DESCRIPTION: ATL10 ... 57
5.1 Basis for freeboard estimation ... 57
5.1.1 Control parameters ... 58
5.1.2 Dataflow and procedural steps ... 58
5.1.3 Expected uncertainties in freeboard determination ... 61
5.1.4 Procedure to filter and fill missing surface reference (*refsurf*) estimates along track ... 62
5.2 Output of freeboard estimation algorithm ... 65
6 ALGORITHM DESCRIPTION: Gridded Freeboard (ATL20) and Sea surface Height (ATL21) ... 67
6.1 Gridded fields of freeboard and sea surface height ... 67
6.1.1 Control parameters ... 67
6.2 Dataflow and procedural steps (ATL20) ... 67
6.3 Dataflow and procedural steps (ATL21) ... 69
6.3 ... 69
7 ALGORITHM IMPLEMENTATION CONSIDERATIONS ... 72
7.1 Multi-beam Architecture: Surface Finding/Classification ... 72
7.2 Product Coverage (ATL07 and ATL10) ... 73
Northern Hemisphere Sea Ice Cover ... 75
7.2.1 ... 75
7.2.2 Southern Hemisphere Sea Ice Cover ... 75
7.2.3 Seasonal and Regional definitions ... 76
7.3 Parameters Required from ATLAS ... 77
7.3.1 System impulse response ... 77
7.4 Parameters from Ancillary Sources ... 77
7.4.1 Gridded ice concentration ... 77
7.4.2 Mean Sea Surface (Arctic and Antarctic) ... 77
7.4.3 Distance from Land Maps (Arctic and Antarctic) ... 77
8 BROWSE PRODUCTS ... 78
8.1 ATL07 ... 78
8.1.1 Line plots (beams) ... 78
8.1.2 Histogram ... 78
8.2 ATL10 ... 78
8.2.1 Line plots (beams) ... 78
8.2.2 Histogram ... 78
8.3 ATL20 ... 78
8.4 ATL21 ... 78
9 DATA FiLTERING ... 79
9.1 Filtering of granules ... 79
9.2 Test Data ... 79
9.3 Data sets ... **Error! Bookmark not defined.**
10 CONSTRAINTS, LIMITATIONS, AND ASSUMPTIONS ... 81
10.1 Constraints ... 81
10.2 Limitations ... 81
10.3 Assumptions ... 81
11 References ... 83
List of Acronyms ... 85
Glossary ... 87

APPENDIX A: Data dictionaries 92
APPENDIX B: Expectation-Maximization (EM) Procedure 93
APPENDIX C: Construction of table to correct biases due to skews in height distributions ... 94
APPENDIX D: Source/calculation of background rates 96
APPENDIX E: Polar Stereographic Projection and Grid 98
APPENDIX F: Mean Sea Surface, Land Mask and Distance Map (Gridded fields) 100
APPENDIX G: First Photon Bias 102
APPENDIX H: Organization of lead data in ATL10 103
APPENDIX I: Surface finding waveforms and TEP averaging 105

List of Figures

Figure Page
Figure 1 Geometric relationships 3
Figure 2 Near-coincident RADARSAT and ICESat-1 datatakes. (a) Geographic location of data. (b) ICESat track (dashed yellow line) and new leads/openings seen in time-separated RADARSAT images over the same area on the ice cover. (c) ICESat freeboard profile and estimated ice draft (snow: light blue; ice: dark blue). (d) Uncorrected reflectivity along the track. (e) The thickness distribution with three superimposed snow covers (red: climatological mean+10cm; black: mean; green: mean-10cm). (RADARSAT imagery ©CSA 2004). The inset in (d) shows the sigmoidal function for applying snow depth. The vertical scale depends on the climatological snow depth at the geographic location of interest. Yellow bands highlight sea ice leads in the radar and lidar data. 4
Figure 3 Multi-beam profiling of the surface with ICESat-2. The ATLAS instrument consists of 6 lidar beams or three pairs of beams separated by ~3 km across track. For each pair, there is a strong and weak beam separated by ~90 m across track. 5
Figure 4 MABEL flightlines (on April 08, April 10) plotted on an Envisat Synthetic Aperture Radar (SAR) mosaic of the region acquired on April 8. Near-coincident ATM data from Operation IceBridge were acquired on April 10. Inset shows the ER-2 aircraft. MABEL is located in the nose of the platform. The segments discussed in this section are from flightlines south of the Fram Strait. 8
Figure 5 Calculated (black line) and observed (solid circles) solar background rates over the flightlines on April-08 (left) and April-10 (right). See Figure 1 for location of these flightlines. 9
Figure 6 Returns from the sea ice cover (Channel 6) along a cloud-free ~5.5 km MABEL track. (a) DCS (Digital Camera System) image containing the MABEL track. (b) Total photon counts from two height intervals: Surface (-3 to 4 meters) and background (4 to 5000 meters). Photon counts are sums of returns from 125 pulses (~5 m along track). Note the different scales for background (left) and surface (right) counts. (c) Photon heights. Color represents total counts in 125 pulses. (d) Number of pulses needed to aggregate at least 100 signal photons. (e) Retrieved height. Location of this MABEL segment is shown in Figure 4. Transparent light-blue band shows characteristics of photons originating near the sea surface. 13
Figure 7 Same as previous figure, but for a different segment. 14
Figure 8 Elevation distributions of leads (left), open-water (center), and snow-covered surfaces (right) (Channel 6). (a) Photon counts along a cloud-free MABEL file-segment (300,000 pulses and ~13 km): Surface (-3 to 4 meters) and background (4 to 5000 meters); counts are 125-shot total. Note the different scales. (b) Photon heights; color represents total of counts in 125-shot (~5 m along track). (c) Photon counts of sub-segment indicated by a dark black line in (b). (d) Photon elevations within the sub-segment. (e) Elevation distributions within the sub-segment (bin size = 2.5 cm). Quantities in top right corner show the mean and standard deviation of the distributions. The plots in the center panel share the y-axis labels found in the left and right panels. 15
Figure 9 Mean time of flight bias (picoseconds) correction for 3.2 ns dead time as a function of apparent width - foreground (ns) and apparent strength (events/shot). 20
Figure 10 Region for freeboard calculations. 22
Figure 11 Flowchart: Production of ATL07. 25

Figure 12 Flowchart: Coarse surface finding (used for strong beams only). 32
Figure 13 Surface height retrieval using 100 photon aggregates. (a) Photon cloud from a 6.5 km segment of MABEL acquisitions. (b) half-width of Gaussian from retrieval process. (c) Retrieved height. (d) Height distributions and modeled returns (red) (at locations A, B, and C in (c)). (e) Error surface. The light- and dark-gray lines in (e) show the local minima along the x-axis (half-width of Gaussian) and y-axis (elevation offset), respectively. Colors show relative size of the minima. Panels a, b, and c share the same x-axis (labeled in c). 35
Figure Figure 14 Flowchart: Fine surface finding. 40
Figure 15. Two-component mixtures in Mabel height distributions (April 8, 2012). (a) Expectation-Maximization (E-M) procedure provides estimates of the parameters in the Mabel height distributions. (b) Distribution of width (w) from the surface finding procedure as a function of $\Delta\mu$ and α from the EM procedure. (c) Distributions of σ_1, σ_2 .(d) Density of population as a function of $\Delta\mu$ and α from the EM procedure, and the location of the impulse response in the two-component space. 46
Figure 16 Correction of the estimated height from the surface finding procedure for skew in distribution. (a) Distribution of corrections before accounting for the tail in the system impulse response. (b) Potential weighting functions to account for system impulse response. (c) Distribution of corrections after accounting for the tail in the system impulse response. (d) Distribution of corrections applied to the April-8 data..... 47
Figure 17 Decision tree: Surface classification (Winter Arctic and Antarctic). 53
Figure 18 Relationship between sea surface height segments (SSHseg), leads, and the reference surface (refsurf) for computing freeboards..... 57
Figure 19 Freeboard estimation..... 64
Figure 20 Flowchart: Multibeam architecture..... 73
Figure 21 Northern and Southern Hemisphere ice covers. 74
Figure 22 Spot and track naming convention with ATLAS oriented in the forward (instrument coordinate +x) direction. 90
Figure 23 Spot and track naming convention with ATLAS oriented in the backward (instrument coordinate -x) direction..... 91
Figure 24 Coverage of SSM/I Grid. 99

List of Tables

Table **Page**

Table 1 ICESat-2 Instrument parameters and expected signal levels over sea ice (Dec 2014) .. 6
Table 2 Input parameters (Source: ATL03) 26
Table 3 Input parameters (Source: ATL09) 27
Table 4 Control parameters – coarse surface finding 30
Table 5 Control parameters – fine surface finding 36
Table 6 Uncertainties in retrieved surface height (100 photons) 43
Table 7 Control parameters – surface classification (Winter, Spring transition, Summer, Fall transition) 50
Table 8 Output to ATL07 (See Appendix A for details of full product dictionary) 54
Table 9 Control parameters – freeboard estimation 58
Table 10 Uncertainties due to surface tilts 62
Table 11 Control parameters – for filtering/filling of along-track reference surface estimates 62
Table 12 Output to ATL10 (See Appendix A for full product dictionary) 65
Table 13 Control parameters – Gridded products 67
Table 14: Key variables output to ATL20 (See Appendix A for full product dictionary) 68
Table 15 Key variables output to ATL21 (See Appendix A for full product dictionary) 70
Table 16 Coverage of ICESat-2 Products in the Northern Hemisphere 75
Table 17 Coverage of ICESat-2 Products in the Southern Hemisphere 75
Table 18 Parameters from ICESat-2 77
Table 19 Parameters from Ancillary Sources 77
Table 20 Data filters (ATL07, ATL10). *NB: the reference surface heights filter (row 3) is still in testing for R005 data production.* 79
Table 21 Current Test Data Sets 79
Table 22 Grid Dimensions 98
Table 23Northern and Southern Hemisphere Grid Coordinates 99
Table 24 MSS of the Arctic and Southern Oceans (file) 100
Table 25 Land Mask and distance map 100

1 INTRODUCTION

This document describes the theoretical basis of the sea ice processing algorithms and the parameters that are derived from the ATLAS data acquired by the ICESat-2 mission. ATLAS (Advanced Topographic Laser Altimeter System) is the photon counting lidar onboard the ICESat-2 Observatory.

This is a living document intended to provide 1) an up-to-date description of the data products for end users, and 2) comprehensive instructions to the developers of the underlying algorithms. The algorithm development is an on-going process, so there can be times when sections of the ATBD reflect the expected state of the data products and not its current state. We have attempted to clarify these differences in more recent versions of the ATBD.

The ATLAS-based sea ice products include:

1. Along-track sea ice and sea surface heights (Product: ATL07/L3A).
2. Along-track sea ice freeboard (ATL10/L3A).
3. Gridded monthly sea ice freeboard (ATL20/L3B).
4. Gridded monthly sea surface height (ATL21/L3B, *expected spring/summer 2021*).

Section 2 provides an overview of the retrieval approaches and a short discussion of the phenomenology of photon clouds from sea ice using data acquired by the Multiple Altimeter Beam Experimental Lidar (MABEL), a technology demonstrator for the ATLAS instrument.

Section 3 describes the geophysical parameters of interest that reside in each product.

Section 4 specifies the sea ice algorithms used in the derivation of surface heights and surface types (ATL07).

Section 5 specifies the sea ice algorithms used in the derivation of sea ice freeboard (ATL10).

Section 6 specifies the sea ice algorithms used in the derivation of the gridded sea ice products (ATL20/21).

Section 7 addresses specific implementation details/considerations and data requirements that are not addressed in the above sections. Topics include: software architecture for multi-beam system; bounds of geographic and seasonal coverage by the different products in the Arctic and Southern Oceans; and, parameters required by the algorithms that are produced by the ICESat-2 project or from an external source.

Section 8 describes the browse products for ATL07, ATL10, ATL20, ATL21.

Section 9 describes the data filtering/quality assessments.

Section 10 describes the data used to design and test the pre-launch algorithms.

Section 11 discusses the constraints, limitations, and assumptions associated with algorithm performance.

2 BACKGROUND

This section describes the sea ice parameters derived from ICESat2/ATLAS altimetry and provides an overview of the approaches used to retrieve these variables. Also, a short discussion of the phenomenology of photon clouds over sea ice is provided.
When conditions allow, the ICESat-2 sea ice products provide estimates of the following parameters of the ice-covered seas of the northern and southern hemispheres:

1. Surface height and type.
2. Total freeboard.

These parameters are provided in along-track and gridded formats.
Even though a sea ice thickness product will not be available as a routine product from the ICESat-2 mission, one of the ICESat-2 science requirements is to produce sea ice parameters that will facilitate the conversion of freeboard to thickness by future investigations. The next section discusses derivation of freeboard and its conversion to sea ice thickness.

2.1 Overview: sea ice freeboard and thickness

We first describe the geometric relationships between the different parameters used in the freeboard and thickness calculations, and then briefly the approach to estimate ice thickness assuming isostatic equilibrium. From altimetric heights, there are three steps in the estimation of sea ice thickness:

1. Discrimination of ice and open water returns;
2. Retrieval of freeboard; and,
3. Conversion of freeboard to ice thickness.

Total freeboard, as defined here, is the height of the air-snow interface above the local sea surface (Figure 1). For the Arctic Ocean, the total freeboard is typically assumed to consist of a snow layer superimposed on the freeboard of floating sea ice, i.e., a two-layered system. This total freeboard height, h_f, above the sea surface can be written as the sum of two terms:

$$h_f = h_{fs} + h_{fi} \tag{1}$$

where h_{fs} and h_{fi} are the thicknesses of the snow and ice layers above the sea surface; h_{fi} is commonly referred to as the sea ice freeboard. For Antarctic sea ice, the situation is more complex because of layering and snow-ice formation (so called "flooded ice" from freezing of water-soaked snow due to infiltration of rain, meltwater, or seawater above the snow-ice interface) during the winter. The efficacy of using a simple two-layered freeboard model of the Arctic (as shown in figure) as a model for the Antarctic ice cover remains to be demonstrated.
From altimetry, the total freeboard (h_f) can be estimated by differencing the ice surface height, h_s, and from the local sea surface height, h_{ssh},

$$h_f = h_s - h_{ssh}. \tag{2}$$

Both h_s and h_{ssh} are typically measured relative to the level of a particular reference ellipsoid (e.g., WGS84). The ATLAS instrument measures both variables. The space-time varying sea surface height is the sum of contributions from a number of physical processes. It can be written as the sum of the following terms:

$$h_{ssh}(x,t) = h_g(x) + h_a(x,t) + h_T(x,t) + h_d(x,t) + O^2. \tag{3}$$

In this equation, h_g is associated with geoid undulations, h_a represents the sea surface response to atmospheric pressure loading, h_T is due to tides, h_d is the dynamic ocean topography (DOT)

associated with geostrophic surface currents, and higher order terms. All these terms vary in time and space and possess their own characteristic length scales. The reader is referred to *Kwok et al.* [2006] for a brief discussion of the various sea surface models and the expected uncertainties of each of these terms.

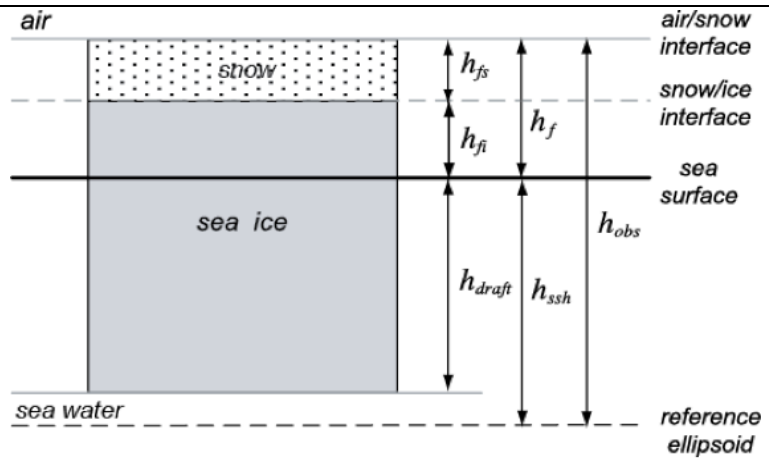

Figure 1 Geometric relationships

Since centimeter-level knowledge of the sea surface height (h_{ssh}) in Equation 3 is lacking, the first step in the retrieval of freeboard is the identification of available sea surface samples in the altimetry data that are usable as ocean surface references. This involves separating the altimetric returns into those from ice and from open water (leads). After identification of the returns into the two surface types, h_f can be then be calculated from the observed heights. Since the sea surface height varies along an altimeter track, an important consideration is the spatial length scale over which one could assume the sea surface height to be nearly constant: this is dependent on the acceptable freeboard uncertainty, the expected spatial variability of sea surface height (i.e., topography), and the expected number of tiepoints (sea surface reference) within an altimeter segment. The spatial variability of h_g deserves special attention as it is more energetic than h_T, h_a, and h_d at all length scales. That is, the small-scale variability of the geoid could introduce significant errors in the freeboard retrieval process if not accounted for. Once h_s and h_{ssh} are determined, ice thickness (h_i) can be estimated with the assumption that the floating sea ice is in isostatic balance:

$$h_i = \left(\frac{\rho_w}{\rho_w - \rho_i}\right)\boldsymbol{h_f} - \left(\frac{\rho_w - \rho_s}{\rho_w - \rho_i}\right)h_{fs}, \tag{4}$$

The densities of ice (ρ_i), snow (ρ_s), and seawater (ρ_w) provide the scaling for hydrostatic equilibrium. ρ_i and ρ_s are both time- and space-varying, and their residuals are sources of error in the calculations. For lidars, the retrieved variable of total freeboard (if no penetration into the snow is expected) is assumed to be the elevation of the air-snow interface differenced from the local sea surface height. That is, the equation as written presumes that no photons scattered are from the interior of the snow pack or the water column. Figure 2 illustrates the ice thickness computed using freeboard and sea surface heights derived from ICESat-1. In the calculation of ice thickness, snow depth (h_{fs}) required to determine snow loading is an input from an external source. Currently, an experimental sea ice thickness product is planned and produced shortly after data release.

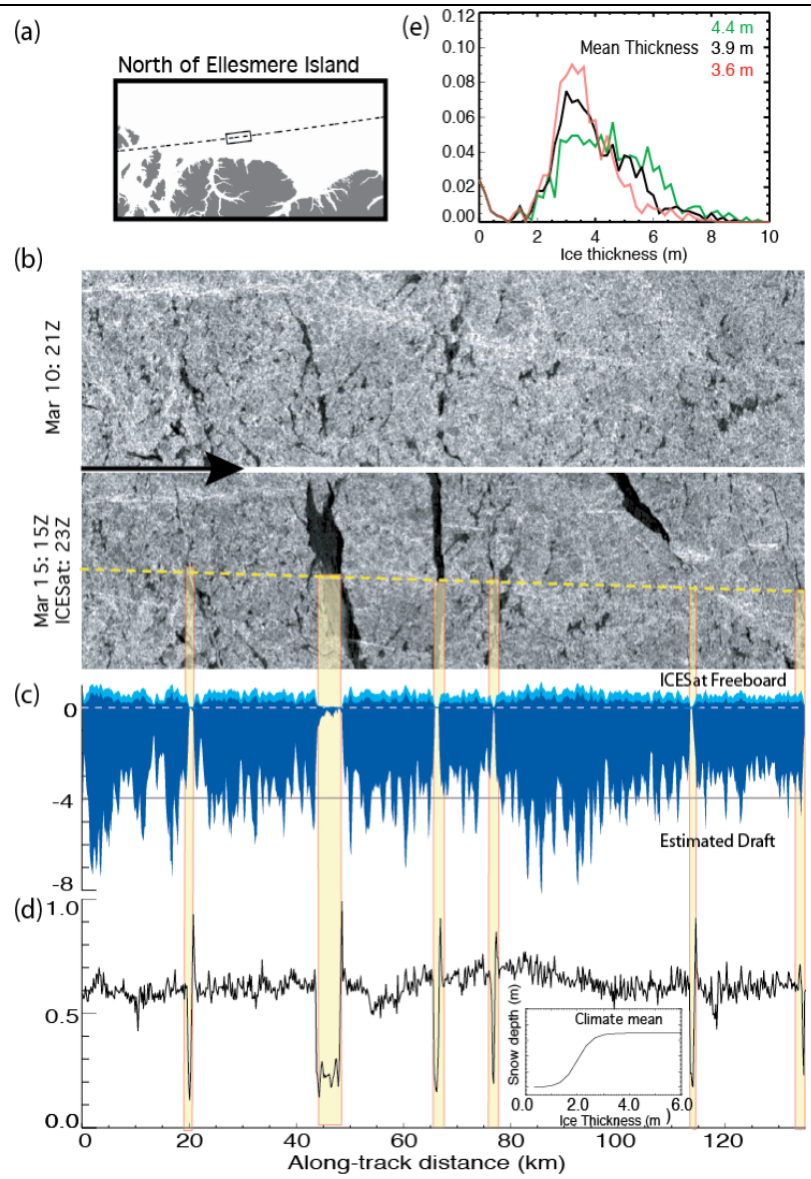

Figure 2 Near-coincident RADARSAT and ICESat-1 datatakes. (a) Geographic location of data. (b) ICESat track (dashed yellow line) and new leads/openings seen in time-separated RADARSAT images over the same area on the ice cover. (c) ICESat freeboard profile and estimated ice draft (snow: light blue; ice: dark blue). (d) Uncorrected reflectivity along the track. (e) The thickness distribution with three superimposed snow covers (red: climatological mean+10cm; black: mean; green: mean-10cm). (RADARSAT imagery ©CSA 2004). The inset in (d) shows the sigmoidal function for applying snow depth. The vertical scale depends on the climatological snow depth at the geographic location of interest. Yellow bands highlight sea ice leads in the radar and lidar data.

2.2 Photon counting altimetry over sea ice

Instead of an analog profiling lidar used on ICESat [*Abshire et al*., 2005; *Schutz et al*., 2005], ICESat-2 employs a photon counting (PC) system to obtain better measurement sensitivity with lower resource (power) demands on the satellite platform. A high repetition rate, low pulse energy laser at 532 nm and sensitive detectors are used to provide the round-trip time of individual photons scattered from the surface. The ATLAS instrument transmits laser pulses at 10 kHz and at the ICESat-2 nominal orbit altitude of ~500 km, the laser footprints (~17 m) are separated by ~0.7 m along ground tracks. Six across track beams (three pairs of strong and weak beams) provide profiles of the ice surface, and for ice sheets the multiple beams address the need for unambiguous separation of ice sheet slope from height changes [*Zwally et al*., 2011]. For sea ice, this provides multiple profiles of sea ice and sea surface heights for improved freeboard and thickness retrievals. The beam configuration and their separation are shown in Figure 3: the beams within each pair have different transmit energies ('weak' and 'strong', with an energy ratio between them of approximately 1:4) and are separated by 90 m in the across-track direction. The beam pairs are separated by ~3.3 km in the across-track direction, and the strong and weak beams are separated by ~2.5 km in the along-track direction (in Figure 3, green circles indicate laser spots from the weak beams, while the dark green

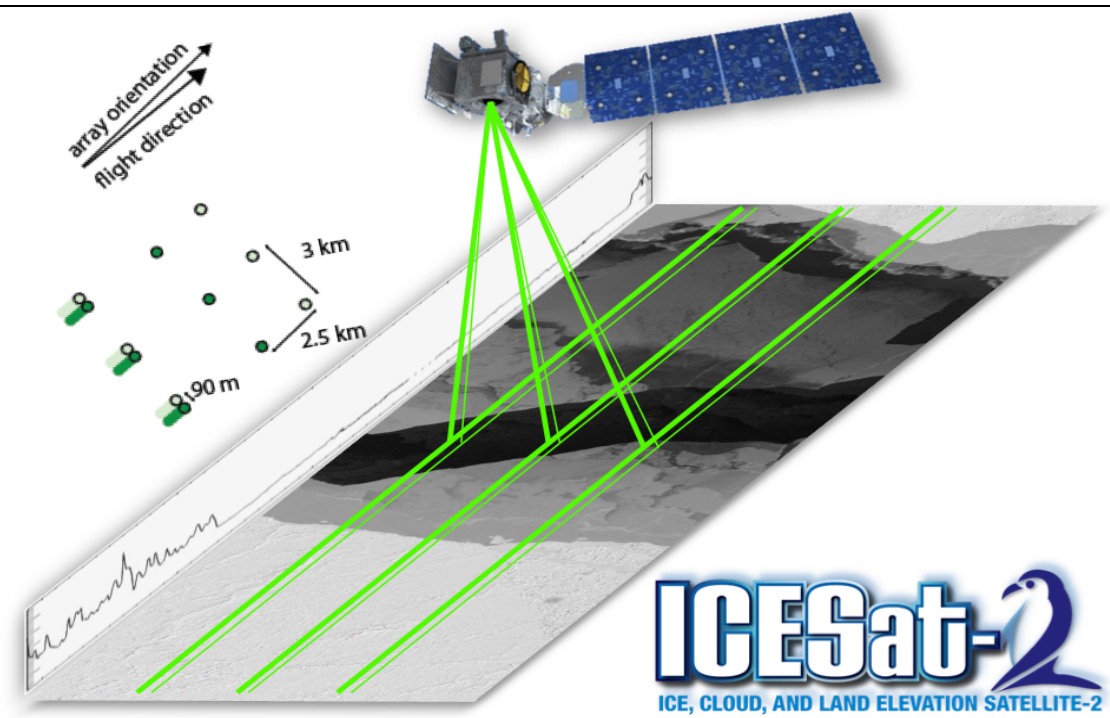

Figure 3 Multi-beam profiling of the surface with ICESat-2. The ATLAS instrument consists of 6 lidar beams or three pairs of beams separated by ~3 km across track. For each pair, there is a strong and weak beam separated by ~90 m across track.

circles indicate spots from strong beams).

2.2.1 Expected ATLAS performance over sea ice

The ICESat-2 instrument parameters and the expected range of signal levels over sea ice for the strong and weak beams are shown in Table 1. For highly reflective surfaces (like snow) under clear skies, on the order of 6/1.5 signal photons from a single strong/weak beam are expected to be recorded by ATLAS for a given transmit laser pulse. For dark leads, the expected signal photons six times lower. At the same time, background photons (discussed below) from sunlight at the same 532 nm wavelength may be arriving at the detector, and some of them will also be recorded by ATLAS. In sum, the number of photons recorded by ATLAS depends on the geometry and reflectance of the Earth's surface, solar conditions, and on scattering and attenuation in the atmosphere.

Table 1 ICESat-2 Instrument parameters and expected signal levels over sea ice (Dec 2014)

Parameter	ICESat-2
Operational altitude, R	490 km
Wavelength, λ	532 nm
Telescope diameter, A_T	0.8 m
Pulse repetition frequency	10 kHz
Pulse energy, E_t	41/160 μJ[1]
Footprint ($1/e^2$)	31 mrad (15 m)
Field of view	83 mrad (41 m)
Filter width	30 pm
System/Detector efficiency, T_oQ_E	3%
Swath width	±3.00 km
Signal levels over winter sea ice (photons/pulse)	Expected
Snow-covered ice (albedo=0.9)	1.6/6.2
Open lead (albedo=0.15)	0.26/1.0[1]

Notes:
1. Weak beam/Strong beam.
2. Lidar equation used to compute expected signal levels:

$$N_r = \alpha_\lambda \left(\frac{E_t \lambda}{\hbar c} \right) \left(\frac{T_A A_T T_o Q_E}{\pi R^2} \right)$$

where: α_λ = surface albedo; T_A = molecular atmospheric transmission (0.81 is used in calculations); Q_E = detector quantum efficiency; T_o = system optical transmission; c= speed of light; $\hbar$ = Planck's constant.

2.2.2 Signal vs. background photons: Examples from MABEL

Even though the physical basis of the ATLAS returns from the surface are not different from that of an analog lidar, there are important distinctions and considerations in the use of PC data. Here, with several examples from the Multiple Altimeter Beam Experimental Lidar (MABEL), we show signatures of the variability of returns from sea ice cover within a height window close to the surface. MABEL is an airborne PC lidar used as a technology demonstrator for the ATLAS instrument on the ICESat-2 mission [*McGill et al*., 2013] and it

should be noted that there are differences between the MABEL and ATLAS instruments. Nevertheless, MABEL data serves to illustrate the different aspects of PC altimetry. The MABEL Channel 6 (532 nm) data used here were acquired in early April of 2012 (Figure 4). The sea ice conditions at the time can be considered to be that of early-spring, i.e., there is very little surface melt except perhaps near the ice edge [*Kwok et al*., 2014]. For this deployment, the MABEL instrument performance was operating in a degraded state (i.e., reduced photon return) due to fiber damage sustained during laser/beam-splitter alignment.
One distinction between PC and analog lidars is the discrete nature of the noise processes. The total number of photons (NP_{tot}) within a recorded range window includes those scattered from the surface (NP_{surf}) and atmosphere (NP_{atm}), from solar background (NPs_{bkg}), and those introduced by noise in the detector (NP_{det} : dark counts), viz.:

$$NP_{tot} = NP_{surf} + (NP_{atm} + NPS_{bkg} + NP_{det})$$

Clearly, the larger the fraction of surface (or signal) photons compared to those photons (background) from sources within the parentheses (i.e., higher signal-to-noise ratio), the better for surface retrieval. Background or noise photons add to uncertainties in the surface profiling and retrieval processes. On a cloud free day, NP_{atm} can be considered to be small compared to the other terms but atmospheric scattering increases with cloud cover; the altered path length of these photons could potentially bias the estimates of the surface location. For this MABEL deployment, the detector noise rate (at 0.02 kHz) is much lower than the signal and solar background rates discussed below. In the following discussion, NP_{atm} and NP_{det} are assumed to be negligible.

Solar background consists of radiation from the sun scattered by the surface, the atmosphere (including clouds), or both, possibly multiple times, which finally enters the lidar detectors. The solar background rate (B_s - usually measured in photons/second or MHz) is defined as the solar zenith radiance due to surface and atmospheric scattering of solar energy at the laser wavelength (λ) that is detected by the instrument. The solar zenith angle varies with latitude, seasonally, and with time of day. B_s is negligible at night but significant when the sun is high in the sky. Neglecting atmospheric effects, this quantity can be calculated as:

$$B_s = S_\lambda \alpha_\lambda \cos(\theta_z)\left[\mathrm{S}\right] \text{ (MHz)} \tag{1}$$

B_s is dependent on the bi-directional reflectance of the surface (α_λ), the solar zenith angle (θ_z), and the solar flux at the top of the atmosphere (S_λ). **S**, in the above equation, includes constants and system parameters. This calculated background rate (in MHz or number of photons per second) when divided by 0.5*c* (*c*=speed of light) gives the expected number of background photons found within a one-meter height window.

The observed and expected solar background rates (with $\alpha_\lambda = 0.8$ in Eq. 1) along two flightlines are shown in Figure 5. The observed background rate is calculated using the total number of photons between a height of 4 m and 5000 m above the surface in each MABEL file-segment (or 300,000 pulses). The observed background rates are lower than predicted, but for long stretches of the 3000 km flightline on April-08 north of the coast of Greenland, the calculated and observed background noise rates are highly correlated. There is little variability in albedo in this region of relatively compact snow-covered sea ice, and the changes in the solar zenith angle (see Equation 1) explain a large fraction of the variability in the solar background rates. This can be compared to the more variable rates over the mixed ice cover in

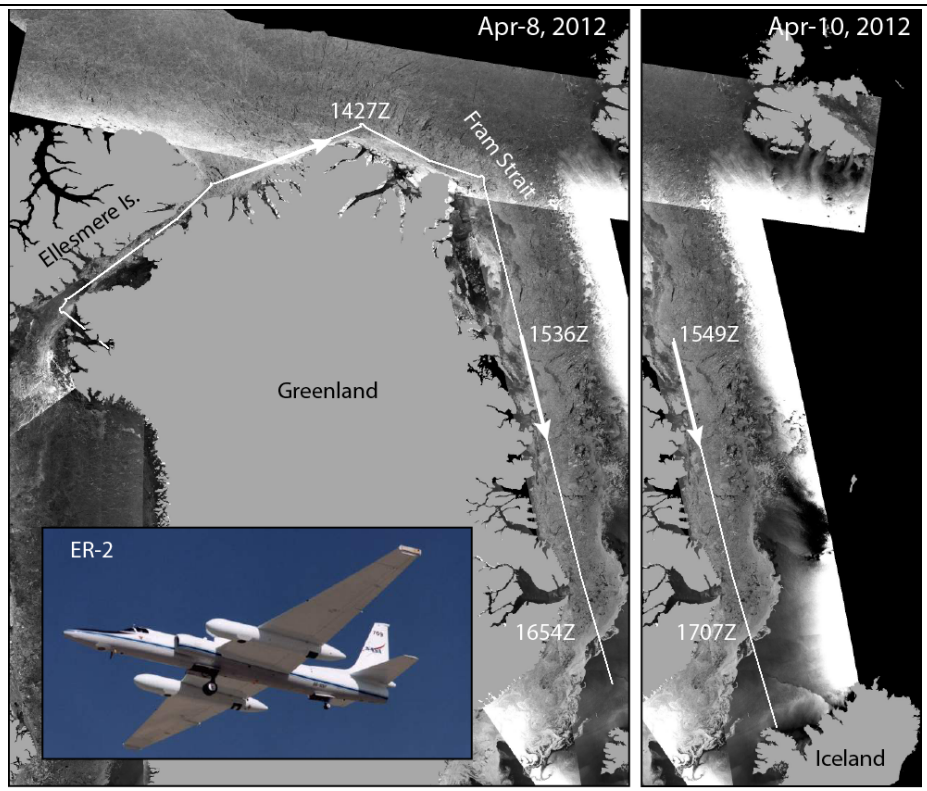

Figure 4 MABEL flightlines (on April 08, April 10) plotted on an Envisat Synthetic Aperture Radar (SAR) mosaic of the region acquired on April 8. Near-coincident ATM data from Operation IceBridge were acquired on April 10. Inset shows the ER-2 aircraft. MABEL is located in the nose of the platform. The segments discussed in this section are from flightlines south of the Fram Strait.

Nares Strait and those just south of Fram Strait. Here, the mix of ice types from old ice to those of recently opened leads, with large contrasts in albedos, contribute to the observed variability. Similar variability can be found in the shorter flightline on April-10 (a repeat survey of the track flown on April-8) of the mixed ice cover (deformed with relatively wide leads) just south of Fram Strait. The discrepancy between the calculated and observed solar background is due to unmodeled changes in albedo and to residual biases in uncertainties in system parameters in the MABEL instrument.

For the two flightlines, the magnitude of B_s (~0.1 MHz) translates into an approximate mean noise density of ~3.3×10^{-4} photons/m. This is equivalent to 1.5×10^{-3} photons over a limited

height window of 5 m containing the surface. The likelihood of finding a noise photon is relatively small compared to the number of expected surface (or signal) photons of between 0.1 and 1.0 photon/shot (see discussion below) from a dark sea ice lead or a snow-covered ice surface, respectively. It should also be noted that the detector dead time (this is discussed in Section 2.2.5) is much smaller (by three orders of magnitude) than the expected interval between background photons (1/ B_s), thus the impact of the background photons on the surface height retrieval is small. We note here that B_s is higher for ATLAS (more than 10 times higher, i.e., 1 MHz) and thus the separation of background from signal photons is an important step in the surface finding process.
Also important for sea ice is that since B_s provides a measure of surface albedo, it is a useful parameter for supporting the classification of surface types in the photon data (see discussion in next section).

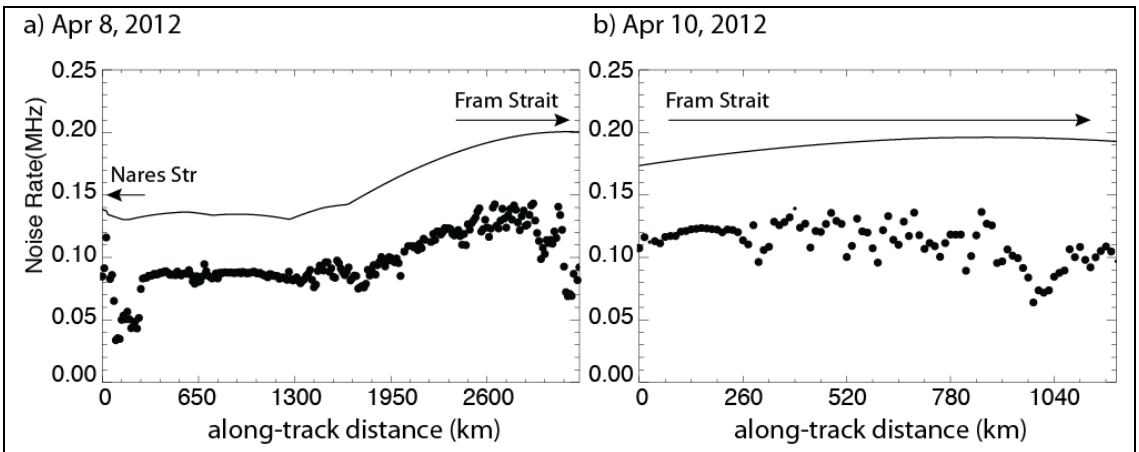

Figure 5 Calculated (black line) and observed (solid circles) solar background rates over the flightlines on April-08 (left) and April-10 (right). See Figure 1 for location of these flightlines.

2.2.3 Sea ice in two MABEL file-segments

Two examples (see Figs. 5 and 6) show the signatures of different surface types in the geolocated photon clouds from MABEL. Of particular geophysical interest are the contrasts in the signal and background rates for discrimination of ice and open water in the retrieval of sea ice freeboard. Each example shows a 5.5 km sub-segment extracted from one 13-km file-segment. A large open water lead is centered in the first example (Figure 6), while the second example shows more along-track spatial structure of the ice cover (Figure 7).
The Digital Camera System (DCS) visible imagery (in Figs. 5a and 6a), which was flown at the same time, shows the sea ice cover profiled by MABEL. Both examples contain at least four sea ice types as suggested by their image intensities and heights (relative to the dark lead). Visually, the brightest samples seem to belong to that of snow-covered sea ice, the next brightest to that of thin ice with a thin layer of snow, then thin ice that is bare of snow, and lastly of open-water in leads. We recognize the thin ice categories as thin ice because their heights are close to that of open-water (see Figs. 5c/e and Figs 6c/e). The derivation of surface height estimates shown in Figs. 5e and 6e are discussed in the next section.
The red and black dots (in Figs. 5b and 6b) show the along-track signal and background photon counts between -3 and 4 meters around the mean surface (henceforth we use the following notation to describe this height interval: [-3, 4] meters) and background noise ([4,

5000] meters) counts, respectively. In both examples, the profile of the background counts is positively correlated to the intensities of the DCS samples (ρ~0.98). This is expected in that the PC system is similar to a camera system that records scattering of incident solar flux at 532 nm from the surface. The ratios of background (*B*) photon counts $NP^B_{snow} / NP^B_{lead}$ between the snow-covered ice surface and open-water leads are ~5-6; approximately what one expects from the albedo differences (of ~0.8 for ice and ~0.1 - 0.2 for leads) between the two surface types [*Grenfell et al*., 1984; *Perovich et al*., 2004].

In these examples, the surface or signal counts and the DCS image intensities are only correlated over the brighter surface categories of snow-covered sea ice, snow-covered thin ice, and thin ice. Over the dark sea ice leads with low background counts, it is striking that the signal or surface photon counts are nearly five to six times the surface counts from a snow-covered ice surface (see Figure 6b and 7b). This is contrary to what one expects from a Lambertian surface, and suggests that these high signal counts are associated with near-nadir specular returns from very smooth surfaces in the open lead. This contrast in surface photon density can be seen in the color-coded plot of photon heights in Figs. 5c and 6c, where the colors represent 125-shot photon counts in the neighborhood (centered) of each detected photon. How close to nadir are these returns from? From consideration of the attitude and relative alignment of the IMU and the lidar, the returns seen in this and examples that follow are from 1 to 2° away from nadir.

Away from the specular returns of open-water, the ratios of surface (*S*) photon counts $NP^B_{snow} / NP^B_{thinice}$ between the snow-covered ice surface and thin ice in the solar background (*B*) are ~3-4. As expected the contrast is somewhat lower than the albedo differences (of ~0.8 for ice and >0.2 for thin ice) between the snow-covered ice and open water.

A measure of PC performance or the sensitivity of the system is the number of pulses it takes to accumulate a certain number of near-surface or signal photons. Here, we use 100 as the count (pulses/aggregate where aggregate count = 100). For MABEL over sea ice, the average varies between ~100 pulses/aggregate and 1400 pulses/aggregate (see Figs. 5d and 6d) or, 1 photon per shot (near specular surfaces) to 1 photon per 14 pulses (low reflectance surfaces), respectively. This parameter is fairly stable over snow-covered sea ice (~500 pulses/aggregate) but there is considerable variability in thin ice and open water areas (shaded regions in Figs. 5 and 6). Thus, even though there are no surface returns from certain pulses, the MABEL photon clouds provide a nice depiction of the surface profile of the sea ice surface because of the high pulse repetition rate or small sample spacing (~4 cm). This can be compared to the expected ATLAS rate of ~6/1.5 photons/shot (high/low reflectance surface) for the strong beam.

2.2.4 Height distributions

Here, we examine the distributions of the photon heights of three distinct surface types: lead, lead with specular return, and snow-covered sea ice (Figure 8). The character of these distributions informs the design of surface height retrieval and classification procedures.

In the first example, we show the height distribution of a sea ice lead with low signal and background counts (Figure 8 – left panel). The surface and background counts (Figure 8a), and the associated photon cloud of the ~1.45 km wide lead (identified by a horizontal black line in Figure 8b) are shown within the context of a 13-km MABEL file-segment. An expanded view of the photon counts is shown in Figs. 8c and d, and the height distribution of the surface photon clouds can be seen in Figure 8e. From the 35,982 transmitted laser pulses over the ~1.45 km wide lead, there were only 1591 surface photons within the [-2, 1] meter height

interval in the neighborhood of the surface. This gives approximately one signal/surface photon in ~22 pulses. From the height plot (Figure 8d – left panel), we see a higher density of the photons below the surface on the right edge of the lead but noticeably higher background counts from the same location. The extended tail in the height distribution of the return from the aggregate of 1591 photons (see Figure 8e – left panel) suggests returns from the subsurface (height S. D. = 0.40 m) but it could also be due to surface roughness. Also, as noted below, the returns may be skewed as a result of the laser pulse shape.

The next example (see Figure 8 – center panel) shows specular returns from a ~500 m wide lead along the 13-km MABEL segment that is flanked by several lower reflectance leads. As discussed above, significantly higher (almost five times) signal/surface counts came from the specular lead. The background counts from this specular lead, that are comparatively lower than those from adjacent leads, suggest a smooth surface of ice or water. In this case, the signal and solar background counts do not co-vary because of the specular return from the surface. There are 7470 signal photons in the 12,497 pulses or ~1 signal photon in 1.7 pulse; this can be contrasted with the 1 in 22 ratio computed for the lead in the previous example. With the larger number of counts from a smooth specular surface over a short distance, the apparent height distribution from this photon aggregate (see Figure 8) provides a measure of the shape of the transmit pulse. The width of the return (S.D. = 0.17 m) is narrower than that of the previous example and compares well with the expected pulse width of 2 ns (S. D. = 15 cm) of the laser, which has a sharper leading edge with a trailing edge that decays at a slower rate. In these two examples, we note that this contrast in both height and surface/background photon counts (as seen in this and the next example) is extremely useful for the discrimination of ice and open water in freeboard calculations.

The 2-km segment shown in Figure 8 (right panel) is from a highly reflective snow-covered surface. Both the surface and background counts are consistently higher than those seen in the left and center panels of Figure 8. Compared to the photon heights of the leads in the previous examples, they have higher variability. In the 1.6 km window, there is ~1 signal photons in 5 pulses, higher than the counts from leads but lower than that from a specular surface. The width of the height distribution from the photon aggregate is 0.54 (S.D.), characteristic of returns from a surface that is rougher than those discussed above. As noted earlier, since the average surface signal per shot from high reflectance surfaces in the current MABEL data set is less than one, the first photon bias (described in *Yang et al*. [2011]) is zero and does not need to be considered. However, this is not the case for ATLAS where the expected return is > 1 photon/shot.

2.2.5 Potential error sources

As alluded in the above discussions, errors in height retrievals from PC lidars like ATLAS can come from a variety of sources:

1) Sampling error: ATLAS height estimates are based on random point samplings of the surface height distribution;
2) Background noise: Random noise-photons are mixed with the signal photons, so sampled photons will include random outliers that are not from the surface;
3) Misidentified photons: The retrieval algorithms will not always identify the correct photons as surface photons in the estimation of surface height;
4) Atmospheric forward scattering: Photons traveling downward through a cloudy atmosphere may be scattered through small angles but still be reflected by the surface

within the ATLAS field of view; these will be delayed, producing an apparently lower surface;

5) Subsurface scattering: photons may be scattered many times within ice or snow volume before returning to the detector; these will be delayed, producing a surface estimate with a low bias. The magnitude of the subsurface-scattering bias delay depends in part on the scattering density of the snow and its bulk absorbance, both of which are determined by the density and grain or bubble size close to the surface. Since neither of these properties may be known at the time of ATLAS processing, each must be determined independently using external information about the snow, such as meteorological model output or infrared reflectance data. Or, the effects may be mitigated in the surface finding process via windowing of the photon height distributions to avoid tails in the distributions;
6) First-photon bias: this is an error inherent to photon-counting detectors that results in a high bias in the mean detected photon height that depends on signal strength. For a short time, t_{dead}, after an individual channel detects a photon, it cannot detect another. This means that photons early in a ground return are more likely to be detected than those later on, and the mean surface height estimate is biased upwards, an effect that is largest for strong returns and for returns from flat surfaces where the return energy is concentrated in a short period of time. For ATLAS, t_{dead} is approximately 2.2 ns and there are multiple channels in each detector (12 for the strong beams, 4 for the weak), to which photons are assigned at random as they reach the detector, resulting in fewer photons reaching each channel while it is inactive. Despite this, up to several cm of bias may be observed for flat bright surfaces with large returns that are close together in time (i.e., the dead time).

These errors are treated in different ways as described in this document.

4) and 5) require information about cloud structure and ice-surface conditions that may not be available. (Note: The nominal corrections may be provided as lookup tables that allow users to generate corrections based on independent estimates of surface and cloud conditions. 6) is corrected routinely during ATL07 processing.

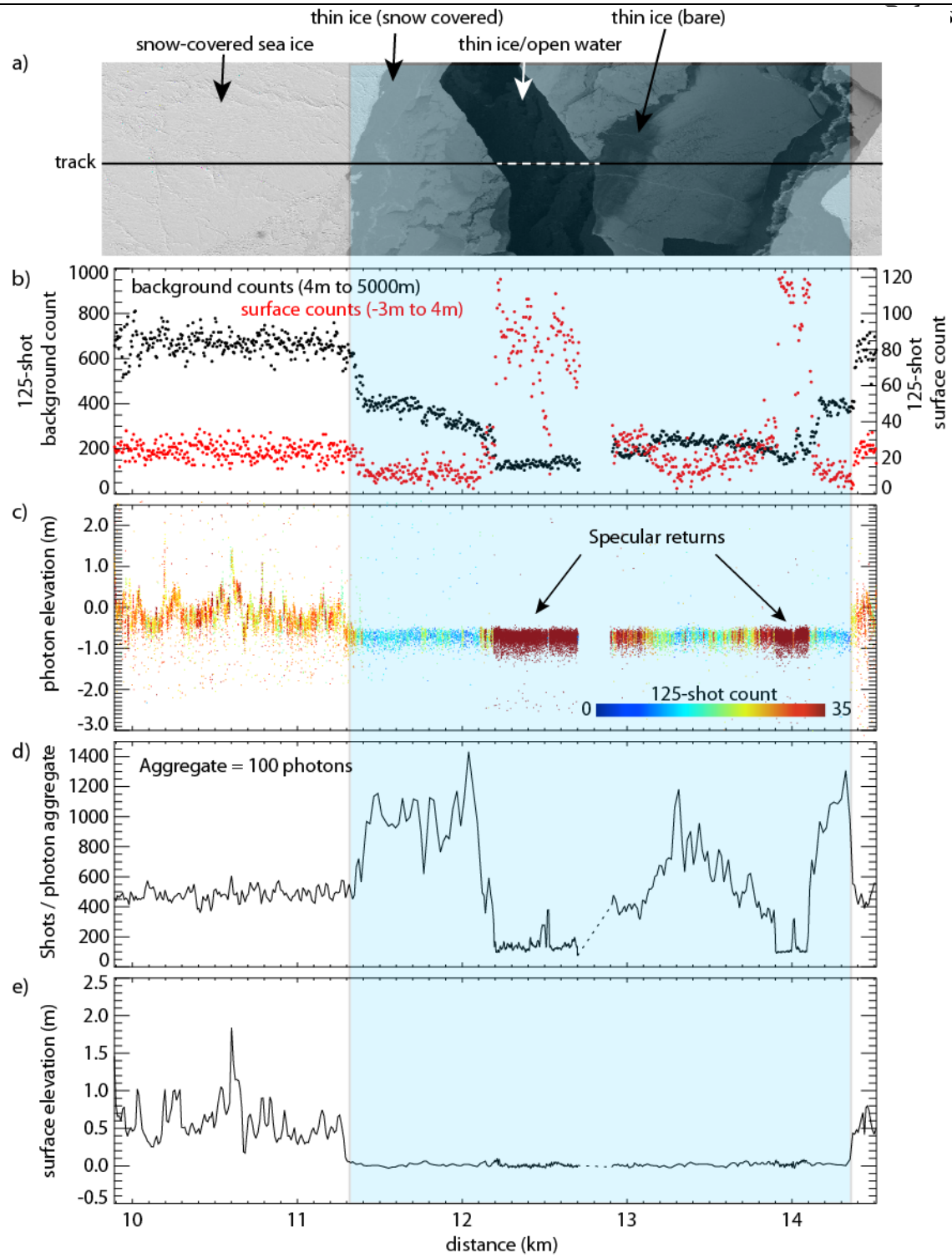

Figure 6 Returns from the sea ice cover (Channel 6) along a cloud-free ~5.5 km MABEL track. (a) DCS (Digital Camera System) image containing the MABEL track. (b) Total photon counts from two height intervals: Surface (-3 to 4 meters) and background (4 to 5000 meters). Photon counts are sums of returns from 125 pulses (~5 m along track). Note the different scales for background (left) and surface (right) counts. (c) Photon heights. Color represents total counts in 125 pulses. (d) Number of pulses needed to aggregate at least 100 signal photons. (e) Retrieved height. Location of this MABEL segment is shown in Figure 4. Transparent light-blue band shows characteristics of photons originating near the sea surface.

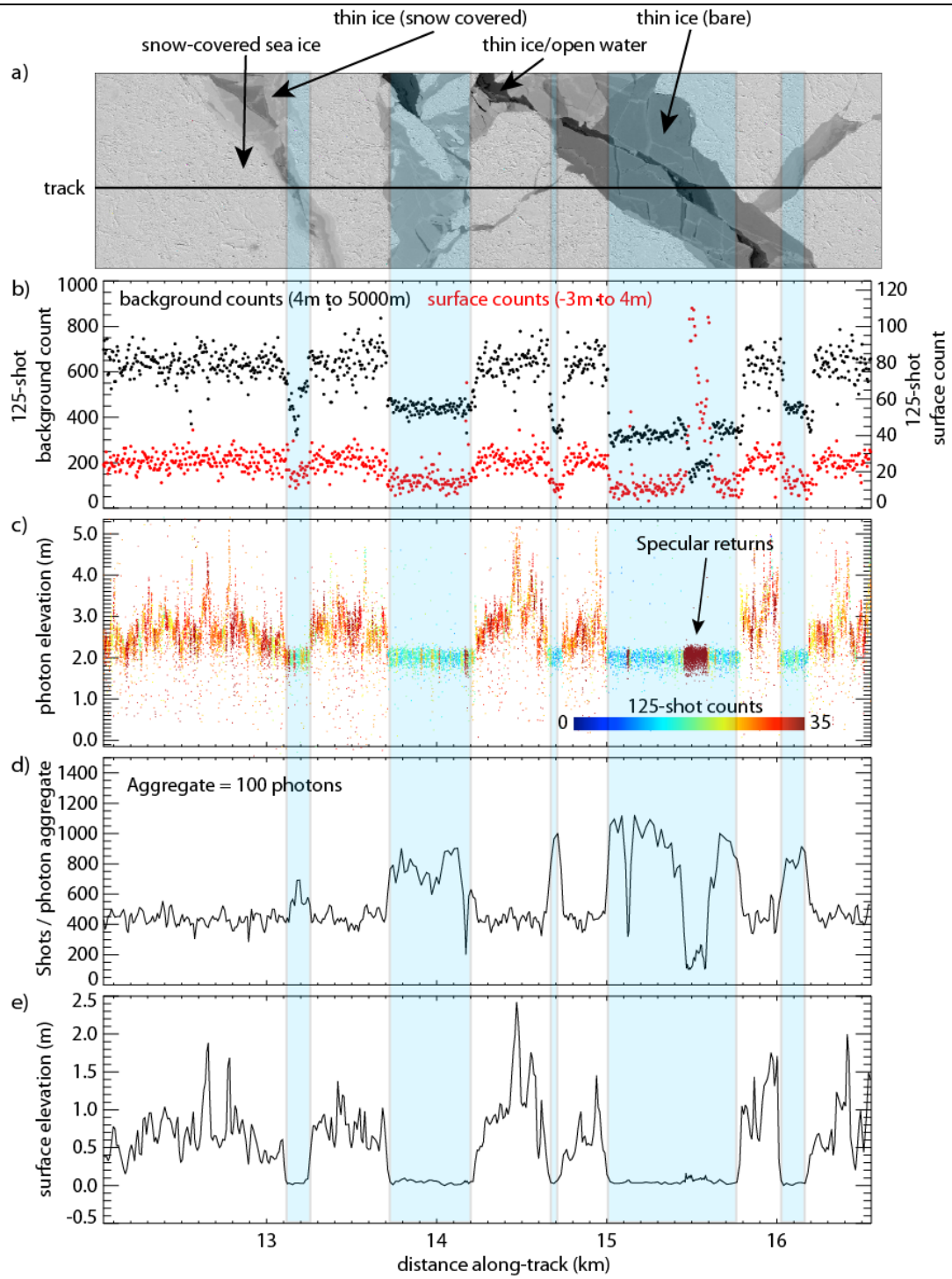

Figure 7 Same as previous figure, but for a different segment.

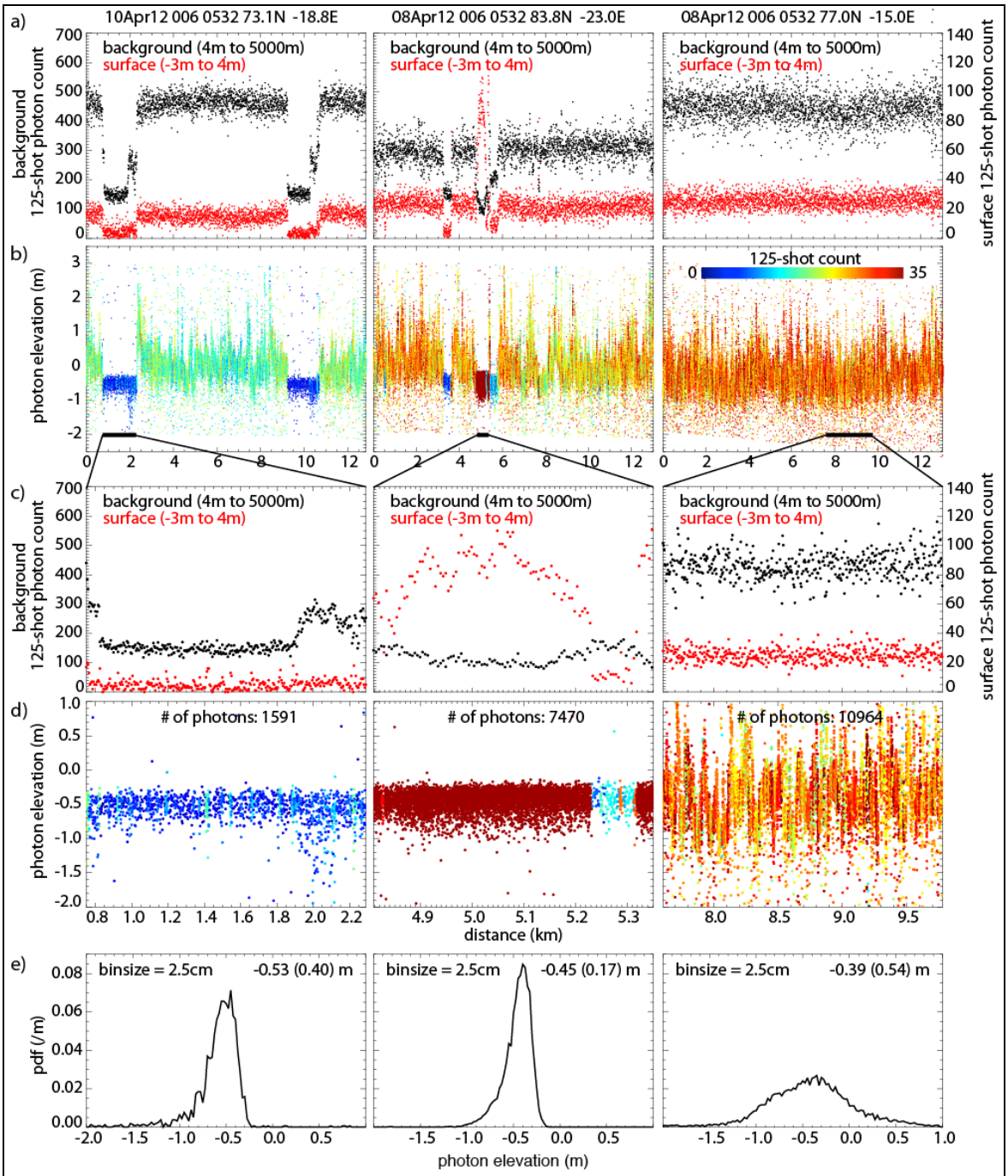

Figure 8 Elevation distributions of leads (left), open-water (center), and snow-covered surfaces (right) (Channel 6). (a) Photon counts along a cloud-free MABEL file-segment (300,000 pulses and ~13 km): Surface (-3 to 4 meters) and background (4 to 5000 meters); counts are 125-shot total. Note the different scales. (b) Photon heights; color represents total of counts in 125-shot (~5 m along track). (c) Photon counts of sub-segment indicated by a dark black line in (b). (d) Photon elevations within the sub-segment. (e) Elevation distributions within the sub-segment (bin size = 2.5 cm). Quantities in top right corner show the mean and standard deviation of the distributions. The plots in the center panel share the y-axis labels found in the left and right panels.

3 SEA ICE PRODUCTS

This section provides an overview of the relevant parameters of geophysical interest in the four sea ice products:

1. Along-track sea ice and sea surface height (Product: ATL07/L3A).
2. Along-track sea ice freeboard (ATL10/L3A).
3. Gridded monthly sea ice freeboard (ATL20/L3B).
4. Gridded monthly sea surface height anomaly (ATL21/L3B).

The ATL07 product contains the sea surface height and sea ice height for segments along each of the six ground tracks. The along-track length of these segments is determined by the distance over which ~150 signal photons are accumulated, so it can change with varying surface types.
The ATL10 product contains sea ice freeboard calculated in three different ways, each determined inside swath segments that are 10 km along-track (nominally) and 6 km across-track (the span of the six beams). These freeboard swath segments contain the leads that are used to establish a sea surface reference for each type of freeboard calculation. The first type is a mean freeboard height (one value) for the entire freeboard swath, based on a reference surface computed as the weighted mean of all the leads within that freeboard swath (still under testing, awaiting better beam alignment). The second type is a freeboard height for each ATL07 sea ice height segment within the freeboard swath (across all six beams) based on the same reference surface (still under testing, awaiting beam alignment). The third is a freeboard height computed for each ATL07 sea ice height segment based on a beam reference surface determined by using only the leads along the beam (each beam has its own reference surface). The fourth is *L*-km mean freeboards along each beam. For convenience, ATL10 also maintains the ATL07 segment heights used for the freeboard calculations

Granule size. The ATL07 and ATL10 products each consist of 32 files (granules) per day, 16 for the northern hemisphere and 16 for the southern hemisphere; each granule contains the sea ice retrievals (heights and freeboards) from data acquired over half an orbit. Six ground tracks within each granule span the width of the orbital swath with an across-track distance of 6 km. The detailed specification of the content of each product can be found in the appendices.

3.1 Surface height product (ATL07/L3A)

This product contains sea ice and sea surface height estimates of the ice-covered oceans derived from each ATLAS beam. Surface height estimates (output of ATL07) are referenced to the mean sea surface (MSS).

3.1.1 Height segments

For each beam (strong or weak), estimates of surface heights are defined for segments of variable lengths (i.e., distance along track; with maximum lengths of ~200 meters) sampled at variable intervals along the ground track. The segment length adapts to changes in photon counts from surfaces with different reflectance. Segment lengths are longer when the photon counts are low and vice versa. A classification algorithm determines the likely surface type of a given height segment to allow for the identification of segments suitable for use as sea surface height (SSH) references for freeboard calculations in ATL10. Height estimates are not produced for segments contaminated by clouds.
The parameters of particular geophysical interest are described below. The detailed structure of this product can be found in the appendix.

3.1.2 Parameters in a height segment

3.1.2.1 Center location/time and segment length

The location/time of each height segment is the average location/time of all surface/signal photons within that segment (i.e., the photons used as input to the surface finding procedure).

3.1.2.2 Surface Heights/Types

The surface finding and classification procedures are described in Section 4. A surface type is assigned to each height segment. Each height estimate (referenced to the WGS84 ellipsoid) is from a surface-finding algorithm (described in Section 4) adapted to work over the ice-covered ocean. Quality metrics for each segment include confidence level in the surface height estimate, which is based on the number of photons, the background noise rate, and the error measure provided by the surface-finding algorithm.

3.1.2.3 First-photon-bias (FPB) corrections

A first-photon bias estimate is provided from system engineering with each height estimate. The expected biases are defined in the Cal-19 (an ICESat-2 document). As mentioned earlier, at low photon rates an insignificant fraction of input events occur during the dead time from a previous event, so the output event rate from the receiver is linear with the input photon rate (the counting efficiency). As the input rate increases, a larger fraction occurs during the dead time, and the behavior becomes less linear. There are 16/4 detectors for the returns from the strong/weak beams to reduce the dead time effect on the observed photon distribution. Figure 9 illustrates the FPB for different return pulse width and events/shot. It can be seen that at the nominal return rates of 6/1.5 photon/pulse (strong/weak beams) for snow covered sea ice, the corrections are ~1-3 cm. It should also be noted that these corrections will use the average dead time for the active channels for each ground track.

3.1.2.4 Subsurface-scattering corrections

The subsurface-scattering, or volume scattering, bias comes from photons that experience multiple scattering within the snow or ice before returning to the satellite. Ice absorbs green light only weakly, with attenuation lengths of tens of meters or more, but ice grains in snow and bubbles in ice both scatter green light strongly [*Warren et al*., 2006]. While most photons exit the surface of a snow pack within a fraction of a nanosecond, some are delayed significantly, potentially producing a long tail on the histogram of return times. Averaging returns times of photons from this tail with photons from the surface return leads to a mean delay in the photon return time, and a downward bias in the apparent surface height. This error and its temporal variability is expected to be small for fine-grained snow surfaces, but it may be more significant in coastal areas where there are large seasonal variations in the surface grain size.

The magnitude of the subsurface-scattering bias delay depends in part on the scattering density of the snow and its bulk absorbance, both of which are determined by the density and grain and/or bubble size close to the surface. Since neither of these properties are known at the time of ATLAS processing, each must be determined independently using external information about the snow, such as meteorological model output or infrared reflectance data.

These corrections will not be provided.

3.1.2.5 Photon Statistics

The photon statistics parameters describe the distribution of the population used in the surface-finding algorithm. These parameters include the: number of photons, histogram of the population, length of segment, and width of the histogram.

3.1.2.6 Background photon rate

The background photon rate is used in estimates of segment-height error, in refining the ground window, and in the classification of surface type.

For each segment, there are three sources of background rate, either:

1. Calculated using the solar zenith angle, the solar flux in the receiver pass band, and the effective aperture of the detectors;
2. From 50-shot average in ATL03;
3. From the atmospheric histogram of photon heights calculated in ATL09 – this is lower-resolution background rate (25 Hz or every 280 m).

3.1.2.7 Apparent Surface Reflectance

This is based on surface photon rate, estimated background rate, and operational lidar parameters.

3.1.3 Input from IS-2 Products (ATL03 and ATL09)

3.1.3.1 Classified photons and height corrections (Source: ATL03/L2B)

The primary input from ATL03 are photons heights, background rates, and corrections applied to the height estimates. The standard height estimates include a number of corrections applied to the height estimates (see below). ATL03 applies multiple geophysical corrections to provide

corrected heights for all the downlinked photons. By design, each of these corrections can easily be removed by the end user from the ATL03 data products if desired. By default, they are applied to generate a best estimate of the photon height. Additional corrections that some users may decide to apply are provided with the product. Also, a number of meteorological parameters (e.g., wind, surface air temperature, sea level pressure, etc.) from reanalysis products are available in ATL03.

Photon cloud parameters:

- Background rate at 400 Hz (which includes solar background and dark count rates)
- The height of the column used in the background calculation (*bckgrd_int_height_reduced*)

The geophysical height corrections provided include:

Time-varying geophysical surface corrections:

- Ocean Tides including diurnal and semi-diurnal (harmonic analysis), and longer period tides (dynamic and self-consistent equilibrium) (±5 m)
- Dynamic Atmospheric Correction (DAC) including inverted barometer (IB) effect (±5 cm)
- Solid Earth Tides (±40 cm, max)
- Long period equilibrium tides (±7 cm)
- Local displacement due to Ocean Loading (-6 to 0 cm)
- Deformation due to centrifugal effect from small variations in polar motion (Solid Earth Pole Tide) (±1.5 cm, the ocean pole tide ±2mm amplitude is considered negligible)

Photon round-trip range corrections:

- Total column atmospheric delay (-2.6 to -0.9 m)

Static and Quasi-static corrections:

- Geoid (-105 to +90 m, max)
- Mean Sea Surface (±2 m)

NOTE: All of the above corrections except ocean tides, long period equilibrium tides, DAC, and geoid undulations are applied to the ATL03 photon heights. An IB correction is applied in ATL07 instead of the full DAC due to uncertainties in DAC estimates over sea ice.

3.1.3.2 Atmosphere (Source ATL09/L3A)

- Relative/calibrated backscatter
- 25-Hz background photon rates
- 25-Hz cloud statistics
- 1-Hz surface pressure, 2-m air temperature, 2-m eastward wind, 2-m northward wind

3.1.4 External inputs (see Section 7)

1. Ice concentration from passive microwave data (NSIDC CDR, daily fields, Table 19).
2. Mean sea surface (MSS) from blended CryoSat-2 and DTU13 data (see Table 19 & 24).

3. Land Mask.
4. Distance from Land Mask.

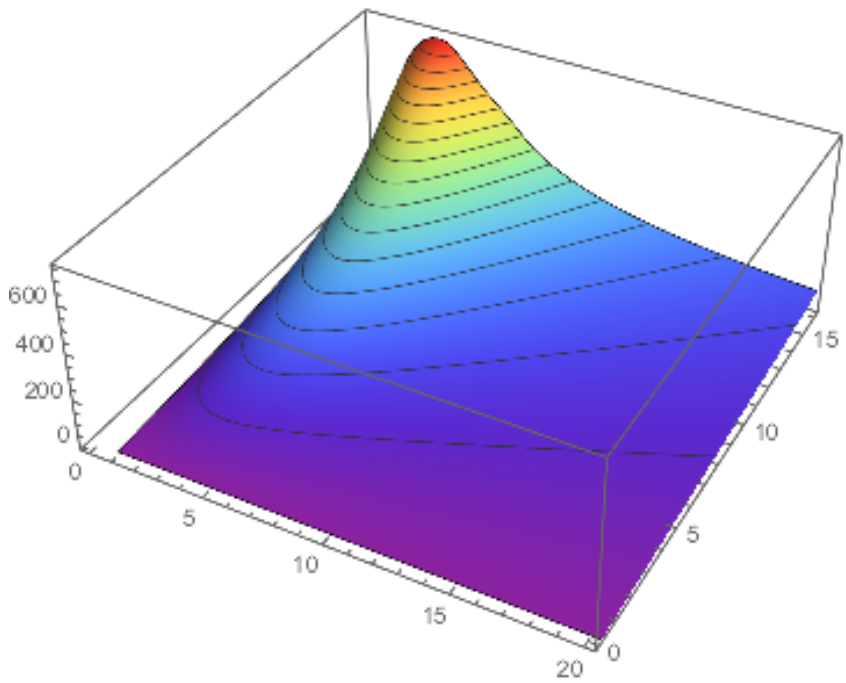

Figure 9 Mean time of flight bias (picoseconds) correction for 3.2 ns dead time as a function of apparent width - foreground (ns) and apparent strength (events/shot).

3.2 Sea Ice Freeboard (ATL10/L3A)

This product, based on results from ATL07/L3A, contains along-track estimates of sea ice freeboard height. Available SSH segments (identified from classification algorithm) within an along-track interval (see Figure 10) are used to establish a local sea surface reference for computing freeboard. A freeboard estimate (IFH) is provided for each ice surface height (ISH) segment defined in ATL07/L3A.The collection of IFH segments within a neighborhood with available SSH segments (i.e., sea surface references) are contained within a freeboard swath-segment (IFH-S).

3.2.1 Sampling (Swath-segment)

An algorithm is used to define, based on the relative location and number of sea surface height segments from all ATLAS beams, a ~10-km along-track window for determining the number of ISH segments to be included in an IFH-S. Swath-segments are of variable intervals along the ground track; this adapts to the infrequent occurrence of sea ice leads. The SSH segments, which have nearly zero freeboard, are included in the swath-segments.

3.2.2 Parameters in a freeboard swath-segment

3.2.2.1 Freeboard

Freeboard estimates (time/location) are from ice and SSH segments from all beams within ~10 km of available sea surface segments. The number of IFH within a swath-segment varies. Each IFH within a swath-segment has an associated uncertainty and quality indicator based on input data quality, distance from available sea surface estimates, and quality of the SSH estimates.

3.2.2.2 Freeboard histogram

This contains the IFH histogram derived from the collection of height segments from all the beams.

3.2.2.3 Sea surface height (SSH) segments (Source: ATL07/L3A)

SSH segments that are used to construct the freeboard swath-segments. It contains their time/location, height, reflectance, quality, etc.

3.2.2.4 Sea ice height (ISH) segments (Source: ATL07/L3A)

ISH segments that are used to construct the freeboard swath-segments: time/location, height, reflectance, quality, etc.

3.2.3 External input (see Section 7)

1. Mean sea surface (MSS) from blended CryoSat-2 and DTU13 data (see Table 24).

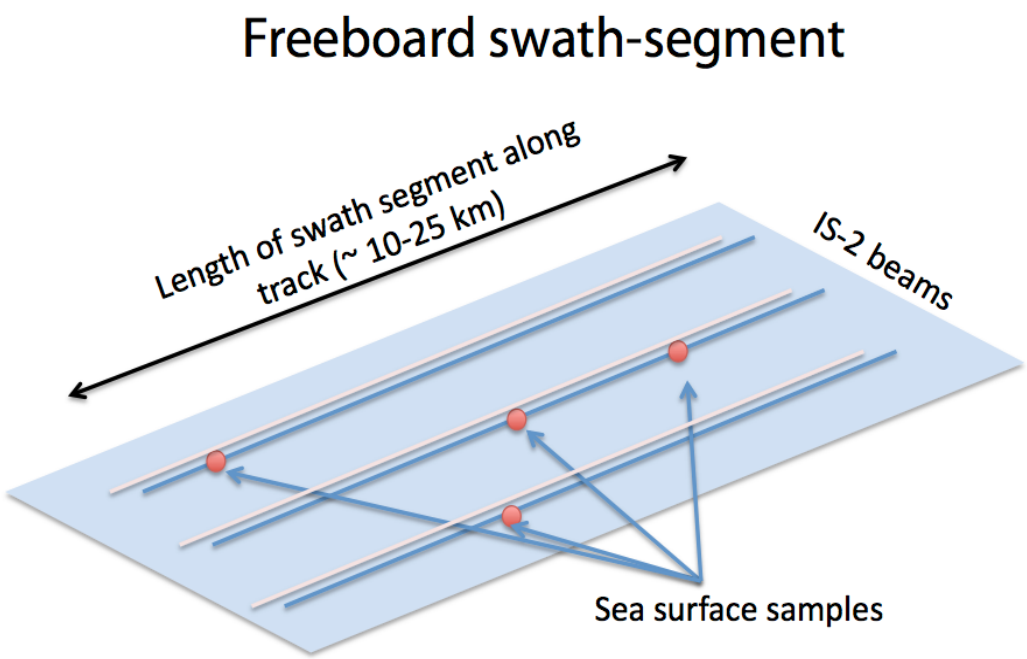

Figure 10 Region for freeboard calculations.

3.3 Gridded Sea Ice Freeboard (ATL20/L3B)

This product, based on Product ATL10/L3A, contains monthly estimates of gridded (spacing: 25 km) IFH from all IS-2 tracks between the beginning and the end of each month. The data are mapped on a planimetric grid using the SSM/I Polar Stereographic Projection.

3.3.1 Grid Parameters

3.3.1.1 Gridded freeboard estimate

This contains the statistical description of daily and monthly freeboard gridded composites (mean, standard deviation, number of segments, total segment length) within each grid cell.

3.3.2 External input

None required.

3.4 Gridded Sea Surface Height - Ice-covered Ocean (ATL21/L3B)

Note that this product is still in the development phase, with an expected release in spring/summer 2021.
This product, based entirely on Product ATL10/L3A, contains monthly gridded (spacing: 25 km) averages of sea surface height from all IS-2 tracks between the beginning and the end of each month. The data are mapped onto a planimetric grid using the SSM/I Polar Stereographic Projection equations.

3.4.1 Grid Parameters

3.4.1.1 Sea surface height (SSH) estimates

This contains the statistical description of the daily and monthly SSH gridded composites (mean, standard deviation, number of segments, total segment length) within a grid cell.

3.4.2 External input

TBD.

4 ALGORITHM DESCRIPTION: ATL07

In this section, we describe the approaches for:

1. Finding the surface in the photon distributions.
2. Discrimination of ice and water.

The block diagrams in Figure 11 show the algorithm flow for producing ATL07. The required inputs are from two ICESat-2 data products: ATL03 (Global geolocated photons) and ATL09 (Atmosphere), and various time-varying and static fields from external sources (listed in Section 7). The reader is referred to the ATL03 and ATL09 ATBDs for more details on the geolocation and atmospheric algorithms used to produce the parameters used in this ATBD. Briefly, we first use a two-step procedure (a coarse and a fine) to locate the ice and sea surfaces in the photon distributions (provided in ATL03); each surface height segment is then labeled as belonging to a surface type based on the photon and background rates. Cloudy conditions are identified using parameters in ATL09. Freeboard estimates (in ATL10) are calculated using available ISH and SSH segments in ATL07.

The following subsections detail the procedural steps. For each procedure, we define the inputs and outputs, and block diagrams and textual descriptions are used to detail the algorithm structure and transformations (i.e., conversions of input to output) in the dataflow. The multi-beam architecture of the overall dataflow to produce ATL07 from the six ICESat-2 beams is described later in this section. To minimize the computational load, the weak beam in each beam-pair takes advantage of the estimated heights in the adjacent strong beam.

Notes:

1. The algorithms defined here are expected to be effective only within certain seasonal windows and regional domains given our current understanding of the sources of geophysical variability that could introduce errors in estimations of height and freeboard, and interpretations of surface type. Therefore, product generation is restricted to those seasons and regions where the algorithms have been tested successfully, albeit not extensively (see Section 5). Sea ice products are produced only if the acquired data fall within predefined seasonal and regional bounds (see Section 7).
2. The IS-2 geolocation-segments (~20-m increments) should be used except for gathering of signal photons to construct the height histogram in the fine surface finding procedures, in which case the finest shot-by-shot spacing should be used.
3. Ocean tides: Locations outside of the domain of the ocean tide model used in ATL03 should be tagged (at the geo-segment rate).
4. Sets of constant parameters are provided for each season/hemisphere for both ATL07 and ATL10 production. The parameters found in the ATL07 product reside in the following /ancillary_data/ folders: coarse_surface_finding, fine_surface_finding, sea_ice, and surface_classification. The ATL10 product constants are found in the /ancillary_data/freeboard_estimation/ folder. When a seasonal change occurs (see Section 7.2.3) in either the northern or southern hemisphere, the appropriate set of constants will be accessed by the software and used in the ATL07/ATL10 production.

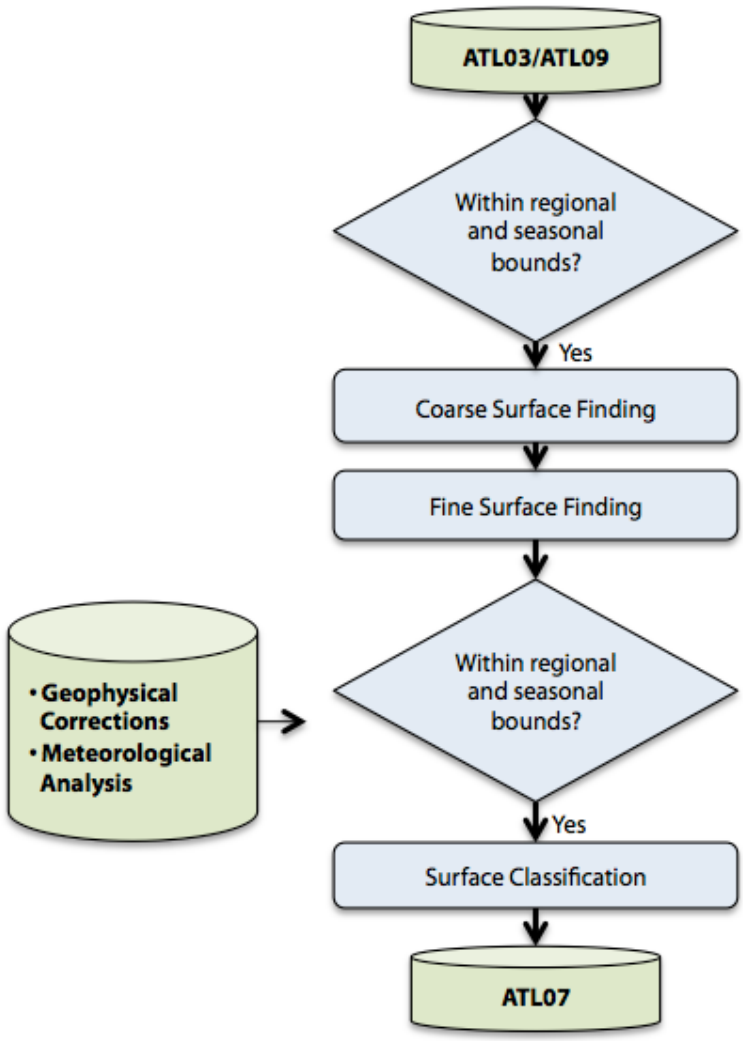

Figure 11 Flowchart: Production of ATL07.

4.1 Input parameters

4.1.1 Source: ATL03

Table 2 Input parameters (Source: ATL03)

Label	Description	Symbol
delta_time	Elapsed seconds since first data point in granule	
lat_ph	Latitude of each received photon	
lon_ph	Longitude of each received photon	
h_ph	Height of each received photon	
dist_ph_along	along-track distance	
sigma_along	uncertainty in along-track distance	
dist_ph_across	across-track distance	
sigma_across	uncertainty in across-track distance	
bounce_time_offset	Difference between the transmit time and the ground bounce time of the reference photons	
segment_ID	geolocation-segment ID	
segment _length	length of each geolocation-segment	
h_quality_flag	Flags describing quality of height for use on higher level products	
ref_azimuth	The direction, eastwards from north, of the laser beam vector as seen by an observer at the laser ground spot viewing toward the spacecraft (i.e., the vector from the ground to the spacecraft). When the spacecraft is precisely at the geodetic zenith, the value will be 99999 degrees.	
ref_elev	Co-elevation (CE) is direction from vertical of the laser beam as seen by an observer located at the laser ground spot.	
solar_azimuth	The direction, eastwards from north, of the sun vector as seen by an observer at the laser ground spot.	
solar_elevation	Solar Angle above or below the plane tangent to the ellipsoid surface at the laser spot. Positive values mean the sun is above the horizon, while negative values mean it is below the horizon. The effect of atmospheric refraction is not included.	
surf_type	Flags describing which surface types this interval is associated with. 0=not type, 1=is type. Order of array is land, ocean, sea ice, land ice, inland water. (from ATL03)	
fpb_parm(n)	parameter needed to compute first-photon bias correction to a mean height	
geoid	The height of the geoid above the ellipsoid	
backgr_r_200	Background count rate, averaged over the segment (200 Hz)	
dac	Dynamic Atmospheric Correction (DAC) includes inverted barometer (IB) effect.	
tide_earth	Solid Earth Tides (±40 cm, max)	
tide_ocean	Ocean Tides including diurnal and semi-diurnal (harmonic analysis), and longer period tides (dynamic and self-consistent equilibrium) (±4 m).	
tide_load	Load tide – local displacements due to ocean loading (-6 to 0 cm)	
tide_equilibrium	Long period equilibrium tides (±7 cm).	
tide_oc_pole	Oceanic surface rotational deformation due to polar motion (-2 to 2 mm).	
tide_pole	Pole Tide -Rotational deformation due to polar motion (-1.5 to 1.5 cm)	
neutat_delay_total	Total neutral atmosphere delay correction (wet+dry).	

TEP-ATL03	Transmit Echo Pulse from ATL03 used here
pod/ppd	POD/PPD flag from ATL03 that indicates the quality of input geolocation products. A non-zero value may indicate that geolocation solutions are degraded or that ATLAS is within a calibration scan period (CAL). Possible non-CAL values are: 0=NOMINAL; 1=POD_DEGRADE; 2=PPD_DEGRADE; 3=PODPPD_DEGRADE; possible CAL values are: 4=CAL_NOMINAL; 5=CAL_POD_DEGRADE; 6=CAL_PPD_DEGRADE; 7=CAL_PODPPD_DEGRADE.

(new in rel005) As of Release005, ATL03 now includes more detailed information (at the geoseg scale) related to the geolocation quality and presence of calibration scan maneuvers (see Table 2). Calibration maneuvers are conducted sporadically during the mission and do not always degrade the quality of the height returns, but do generally cause significant off-pointing which can impact the sea ice retrievals (see the ATL07/10 Known Issues hosted at the NSIDC for more discussion, https://nsidc.org/sites/nsidc.org/files/technical-references/ICESat2_ATL07_ATL10_Known_Issues_v005.pdf).

4.1.2 Source: ATL09

Table 3 Input parameters (Source: ATL09)

Label	Description	Symbol
delta_time	Elapsed GPS seconds since start of the granule. Use the metadata attribute granule_start_seconds to compute full gpstime.	
latitude	Latitude, WGS84, North=+, Lat of segment center	
longitude	Longitude, WGS84, East=+, Lon of segment center	
msw_flag	multiple scattering warning flag *msw*_parameter *flag* has values from 0 to 5 where zero means no multiple scattering and 5 the greatest. If no layers were detected, then *msw_flag* = 0. If blowing snow is detected and its estimated optical depth is greater than or equal to 0.5, then *msw_flag* = 5. If the blowing snow optical depth is less than 0.5, then *msw_flag* = 4. If no blowing snow is detected but there are cloud or aerosol layers detected, the *msw_flag* assumes values of 1 to 3 based on the height of the bottom of the lowest layer: < 1 km, *msw_flag* = 3; 1-3 km, *msw_flag* = 2; > 3km, *msw_flag* = 1.	*msw_flag*
cloud_flag_ASR	cloud probability p=(1-asr/t)*100 *t* is ASR estimate from GMASI (Global 4km Multisensor Automated Snow Ice maps) flag_values: 0 = clear_with_high_confidence 1 = clear_with_medium_confidence 2 = clear_with_low_confidence 3 = cloudy_with_low_confidence 4 = cloudy_with_medium_confidence 5 = cloudy_with_high_confidence	*cloud_flag_ASR*
cloud_flag_atm	Flag that indicates number of layers found from the backscatter profile	

layer_flag	Flag combining solar zenith, *cloud_flag_ASR*, *cloud_flag_atm, and bsnow_con*	*layer_flag*
asr	Apparent Surface Reflectivity (25Hz)	*asr_25*
asr_q	ASR Quality Flag	*asr_b_25*
bgr	Background count rate, averaged over the segment (25 Hz)	*bgr_25*
cab	Calibrated Attenuated Backscatter (CAB) profiles for the RT strong beam or and a sum of the 3 beams covering (nominally) 13 to -1 km at 25 Hz	
bsnow_con	blowing snow layer confidence flag	
bsl_h	blowing snow layer height	
met_slp	sea level pressure (Pa)	
	Note: the sea level pressure from ATL09 should be smoothed with a running average filter with a length of 8 seconds (~50 km) to reduce quantization noise due to the lower sampling rate of this parameter in the ATL09 product	*met_slp*
met_t2m	air temperature 2 meters above the surface (K)	*met_t2m*
met_u2m	eastward wind 2 meters above the surface	*met_u2m*
met_v2m	northward wind 2 meters above the surface	*met_v2m*

4.1.3 External (time-varying/static fields - see Section 7)

4.1.3.1 Time-varying fields

Ice concentration from CDR passive microwave (daily): the nearest daily field within +/- 1 day is used (see Table 19).

4.1.3.2 Static fields

Mean sea surface (MSS) from blended CryoSat-2 and DTU13 data (see Table 19 & 24),

4.2 Finding the surface

Prior to surface finding, do the following to the photon heights:

- Remove all TEP photons.
- Remove the mean sea surface (MSS) heights, which are bilinearly interpolated to the photon locations.
- Apply the ocean tide corrections.
- Apply the long period equilibrium tide corrections only when there is a valid ocean tide correction. (i.e., when tides both are available).
- Apply the inverted barometer (IB) corrections using *met_slp* (local Sea Level Pressure) from ATL09 (bilinearly interpolated to the photon locations) as
$$h_{\mathrm{IB}} = -9.948(met_slp-1013.25)/1000. \text{ (meters).}$$
- (new for rel005), calculate (but do not apply to the segment height, still under testing) a 'dynamic' inverted barometer (IB) correction using the following equation.
$$h_{\mathrm{IB}} = -9.948(met_slp-oce_slp)/1000. \text{ (meters).}$$
Where *oce_slp* is the time varying (hourly) sea level pressure over the global oceans.

The applied corrections can be summarized as follows:

$$h = h_ph - h_{\mathrm{MSS}} - h_{\mathrm{ocean_tide}} - h_{\mathrm{lpe_tide}} - h_{\mathrm{IB}}$$

(sign convention is consistent with that used in ATL03)

NB: In rel001 to rel003 data there were inconsistencies in the treatment of the solid earth tide (SET) in ATL03 and the sea ice products. The ATL03 heights are corrected for the SET (since rel001). The computed SET includes both time-dependent (periodic) and time-independent (permanent) solid Earth displacements produced by the tidal gravitational potential of external bodies (e.g., the Moon and the Sun). Subtracting the SET from the measured heights results in heights referenced to a tide-free crust. However, the model of the mean sea surface (MSS; heights above the WGS84 ellipsoid) used in ATL07/10 is obtained from direct measurements of the sea surface which includes the permanent component of the SET (i.e., 'mean-tide' system). This discrepancy has now been rectified by moving the sea ice products into a 'tide-free' system consistent with the ATL03 heights by converting the MSS to a 'tide-free' MSS as

$$MSS\ (tide\text{-}free) = MSS\ (mean\text{-}tide) - geoid_free2mean\ ,$$

where *geoid_free2mean* = 0.1287 − 0.3848 $\sin^2\varphi$ (meters) and φ is the latitude.

The total SET correction (applied in ATL03) is given as *height_segment_earth* and the calculated permanent tide component is given as *height_segment_earth_free2mean* = 0.06029 − 0.180873 $\sin^2\varphi$ (meters) which can be added to the heights in ATL07/10 to restore the permanent solid earth tide displacement (tide-free to mean-tide system). Note also that the expected sea surface height window is dynamically adjusted to consider this change to a tide-free system.

New free-to-mean conversion factors are now included in ATL07 and ATL10 to easily change from the tide-free system to the mean tide system:

In ATL07:
gtx/sea_ice_segments/geophysical/height_segment_earth_free2mean
gtx/sea_ice_segments/geophysical/height_segment_geoid_free2mean
In ATL10:
gtx/freeboard_beam_segment/geophysical/height_segment_earth_free2mean
gtx/freeboard_beam_segment/geophysical/height_segment_geoid_free2mean

(new for rel005): A new user guide providing more insight into these different tide systems and geophysical corrections has been drafted by the ICESat-2 PSO (Geophysical Corrections for the ICESAT-2 Sea Ice Products) which will be made available through the NSIDC portal.

4.2.1 Coarse surface-finding

Over sea ice, the ATL03 product provides photon clouds in 30-m height windows that include the surface return. This first step in the surface finding process aims to produce a coarse estimate of the mean surface height over a *L*-km segment of the orbit that is within ±0.5 m of the local surface; this narrows the search space and the computational load of the fine surface-

finding process outlined in the following section. Figure 12 shows the high-level dataflow of this coarse surface-finding procedure.

Notes:

- It is assumed that the ICESat-2 photon heights will already have all corrections applied (geophysical height corrections in ATL03). Once the mean sea surface (MSS) is removed in the following procedures, we assume the surfaces are near the sea surface and are henceforth designated as *h*. Ideally, the height of sea surfaces should be near zero. (Note: The MSS is an external input discussed in Section 7.)
- The coarse height estimates for the weak beams are based on the output of the fine surface-finding results of the adjacent strong beam. That is, the weak beam is slaved to the fine-tracker output from the strong beam. See section 5.1 on multibeam architecture.

4.2.1.1 Control parameters

Table 4 Control parameters – coarse surface finding

Parameter	Description	Value
B_c	bin size of coarse histogram	10 cm
L	along track segment length	10 km
nph_min	minimum # of photons for 30m histogram	1
Th_F_m	fraction of histogram peak	0.2
Th_D	distance from mode on negative side	2 m
Th_D_p	distance from mode on positive side	3.5 m
Th_t_c	height deviations from surface or adjacent strong beam	3.0 m
Th_P_c	percentage cloud cover	TBD
coarse_ub_wins	coarse tracker window upper bounds	15 m
coarse_lb_wins	coarse tracker window lower bounds	-15 m

Note: All threshold parameters are prefixed by *Th.*

4.2.1.2 Dataflow and procedural steps

The steps are as follows:

Note: Only returns located in regions with >15% ice concentrations (based on daily NOAA/NSIDC CDR passive microwave sea ice concentration fields) should be processed.

N.B. Each L-km along-track segment is made up of ~L-km/0.02km geolocation-segment. Bins are ~20 m incremental segments that designate the along-track distance from the equator (*dist_ph_along* from ATM03). The *binning* allows for the coarse determination of along-track distance of all the photon heights within them.

For each *L*-km along-track segment:

1. Calculate percentage cloud coverage within a *L*-km segment using cloud information from ATL09: If 25-Hz *layer_flag=0* (from ATL09) then it is clear for that 280 m section of orbit.
2. If percentage cloud coverage > Th_P_c, advance 0.5*L*-km for next segment.

3. Retrieve all photon heights (signal+noise) within the selected geolocation-segments.
4. (*added in the ATBD in rel005, filter been present since rel001*) Filter out all photons with a height outside of a coarse tracker window. By default, the window size is fixed at +/- 15 m (0 m is assumed to represent the mean sea surface after applying the above corrections to photon heights as described in Section 4.2). This window can be adjusted by modifying the controllable parameters for coarse track window lower and upper bounds (*coarse_lb_wins* and *coarse_ub_wins*)
5. Construct histogram of photon heights h (not cloud contaminated) with specified bin size (B_c).
6. If the number of photons within the column and the histogram total are both greater than *nph_min*, do the following (else advance 0.5L-km to next segment):
   a. Find population at the mode of the histogram (N_{cmode}). If there is more than one peak ($N_{maxpeak}$) with population = N_{cmode}, use the ($N_{maxpeak}$-1)/2 peak for the mode.
   b. If the mode peak is not in the first or last histogram bin, do the following (else advance 0.5L-km to next segment):
      i. Trim histogram by removing the bins before/after the first/last occurrence of cells with population less than $Th_F_m * N_{cmode}$ and by removing the bins more than [Th_D_n , Th_D_p] away from the mode
      ii. Estimate the mean height ($\overline{h}_c$) and standard deviation (σ_c) of the trimmed height histogram.
      iii. If deviation of mean height ($\overline{h}_c$) from the MSS (assumed to be near 0) > Th_t_c meters, then advance 0.5L-km to next segment.
      iv. Output: mean ($\overline{h}_c$) and standard deviation (σ_c) of the height histogram.

The fine-tracking algorithm breaks the photons up into N_s = 150 (this number can be changed, see 4.2.2.3 control parameters) aggregate segments, therefore the last aggregate in the L-km along-track segment may have less than Ns photons. This Ns aggregate segment is flagged and skipped over. In this case, when the coarse-tracking algorithm advances to the next L-km along-track segment, it starts the coarse segment with the first geo-bin that has the flagged N_s aggregate segment within it. Consequently, no valid data are erroneously removed and each coarse segment may be less than L-km long.

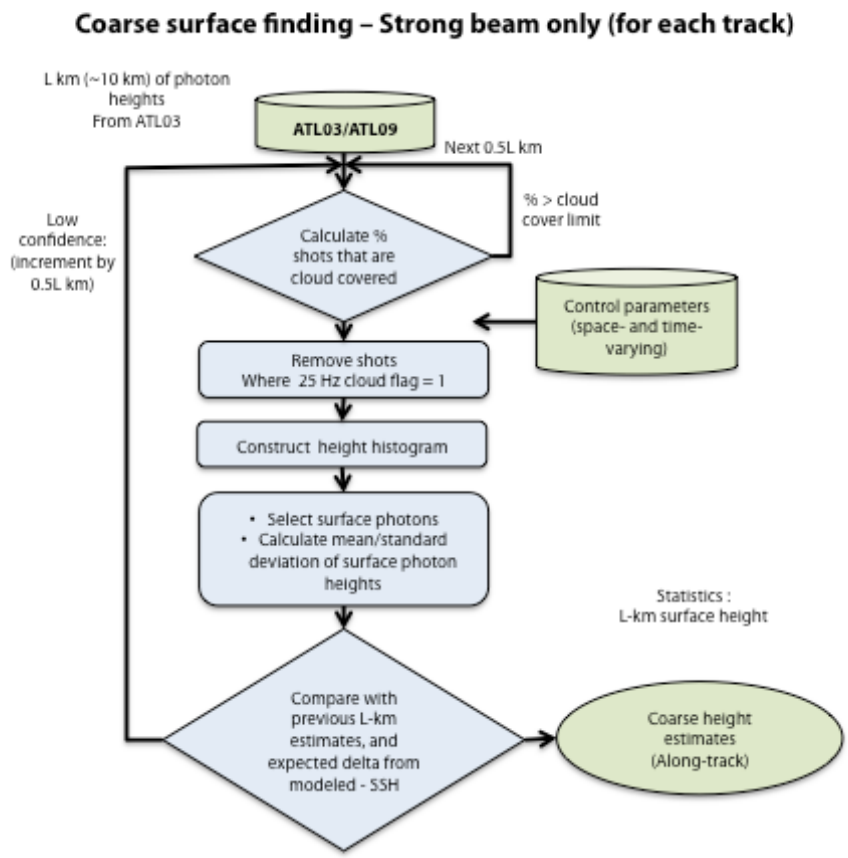

Figure 12 Flowchart: Coarse surface finding (used for strong beams only).

4.2.2 Fine surface-finding: Fitting the expected return to the photon cloud

Figure 14 shows the high-level dataflow for this procedure. First we discuss the basis for refining the height estimate from the coarse tracker. Then, we describe the dataflow and procedural aspects used to refine the coarse height estimate for individual segments.

4.2.2.1 Basis for height retrieval

The expected return, $s_e(h)$, from a surface with a Gaussian height distribution (width w or two times standard deviation) at a height offset of h_o (i.e., $G(h; h_o, w)$) can be written as,

$$s_e(h; h_o, w) = s_t(h) * G(h; h_o, w)\,, \tag{2}$$

where $s_t(h)$ is the impulse response of the system and * is the convolution operator. That is, the expected return is assumed to be the convolution of the system impulse response with a Gaussian surface height distribution of width *w*.

Further, we define the mean-squared difference between the normalized received signal (or height distribution), $\tilde{s}_{rec}(h)$, and the normalized expected return, $\tilde{s}_e(h)$, to be,

$$e^2(h_o, w) = \frac{1}{N}\sum_N (\tilde{s}_{rec}(h_i) - \tilde{s}_e(h_i; h_o, w))^2$$
$$\sum_N \tilde{s}_{rec}(h_i) = 1$$
$$\sum_N \tilde{s}_e(h_i; h_o, w) = 1. \tag{3}$$

The two variables ($\tilde{s}_e(h)$ and $\tilde{s}_{rec}(h)$) are normalized because we do not have *a priori* knowledge about the amplitude of the received signals (or the reflectivity of the surface). Lastly, we consider the minimum in the error surface, $e^2(h_o, w)$, to be the best estimate of the height offset, $\hat{h}_o$, of a surface with a Gaussian distribution of width $\hat{w}$. This can be represented as,

$$\{\hat{h}_o, \hat{w}\} = \operatorname{argmin} e^2(h_o, w) \quad h_o \in [h_1, h_2] \quad w \in [w_1, w_2]. \tag{4}$$

That is, the set of points of the given argument for which the function e^2 attains its minimum value within the intervals defined by $h_o \in [h_1, h_2]$ and $w \in [w_1, w_2]$ is considered to be the best estimates of h_o and *w*. (In the following procedure, an expected return waveform is considered valid only if it contains its peak value and that the peak value does not occur at the start or end of the waveform. If the expected return is invalid it is skipped.)

The key parameters that control behavior of the retrieval process described above are: the number of signal photons and bin size used in constructing the height distribution, $\tilde{s}_{rec}(h)$; the window size or the number of bins (*N* in Eq. 3) of the height distribution used in the process; and the size of the search space in width ($w \in [w_1, w_2]$) and height offset ($h_o \in [h_1, h_2]$).

A height distribution ($\tilde{s}_{rec}(h)$) can be constructed using photon heights from a fixed or variable number of pulses. Rather than using photons from a fixed number of pulses, we find it best to use a fixed number of photons (or aggregates) over a variable number of pulses. With aggregates, the height distributions ('waveforms') are constructed with photons from a larger number of pulses over surfaces with lower returns, and vice versa. This allows the control of signal strength (or signal-to-noise ratio) of the constructed waveform and thus the consistency in the quality of the surface retrievals. This is well suited for sea ice surfaces with its broad range of expected reflectance. We note, however, that the spatial resolution of the retrievals varies along track and is proportional to signal strength.

Here, we show retrieved heights within a defined height window using an example from MABEL (Figure 13). The window size specifies that portion of the height distribution used in the surface estimation process. The size is defined by the standard deviation (σ) of the distribution within -2 to 3 m of the mean height of the photons in that window. In the results shown here, we truncate the distribution at 2σ from the mean, i.e., we use a window size of 4σ. This effectively limits the number of noise photons used in the retrieval process. Potentially, narrowing the width of the window could also be used to reduce the sensitivity of the retrieved height to the contributions of subsurface returns present in the tails of the distribution. In this example, the [-2, 3] m interval works quite well, however we may have to expand the window to include taller ridges.

To implement this approach, we also require estimates of $s_t(h)$, i.e., the impulse response of the system. Surface retrieval is sensitive to the shape of $s_t(h)$, especially when the surface is relatively flat compared to the pulse width. Asymmetric transmitted pulse shapes or system response, if not accounted for, would introduce biases in the height estimates. The search space in height offset and width seen in Eq. 4 (i.e., $w \in [w_1, w_2]$ and $h_o \in [h_1, h_2]$) depend on the quality of the initial estimate of the mean height calculated above and the expected distribution of the surface relief.

4.2.2.2 Mixture distributions

The surface-finding procedure assumes that the surface heights are normally distributed. Potentially, there could be mixture distributions within the photon aggregate. We provide the parameters of a mixture of two Gaussians (means, standard deviations, and mixing ratio) fitted to the height distribution as measures of deviation of the local distributions from that of a single Gaussian. The parameters of the mixture are from the Expectation-Maximization procedure described in Appendix B.

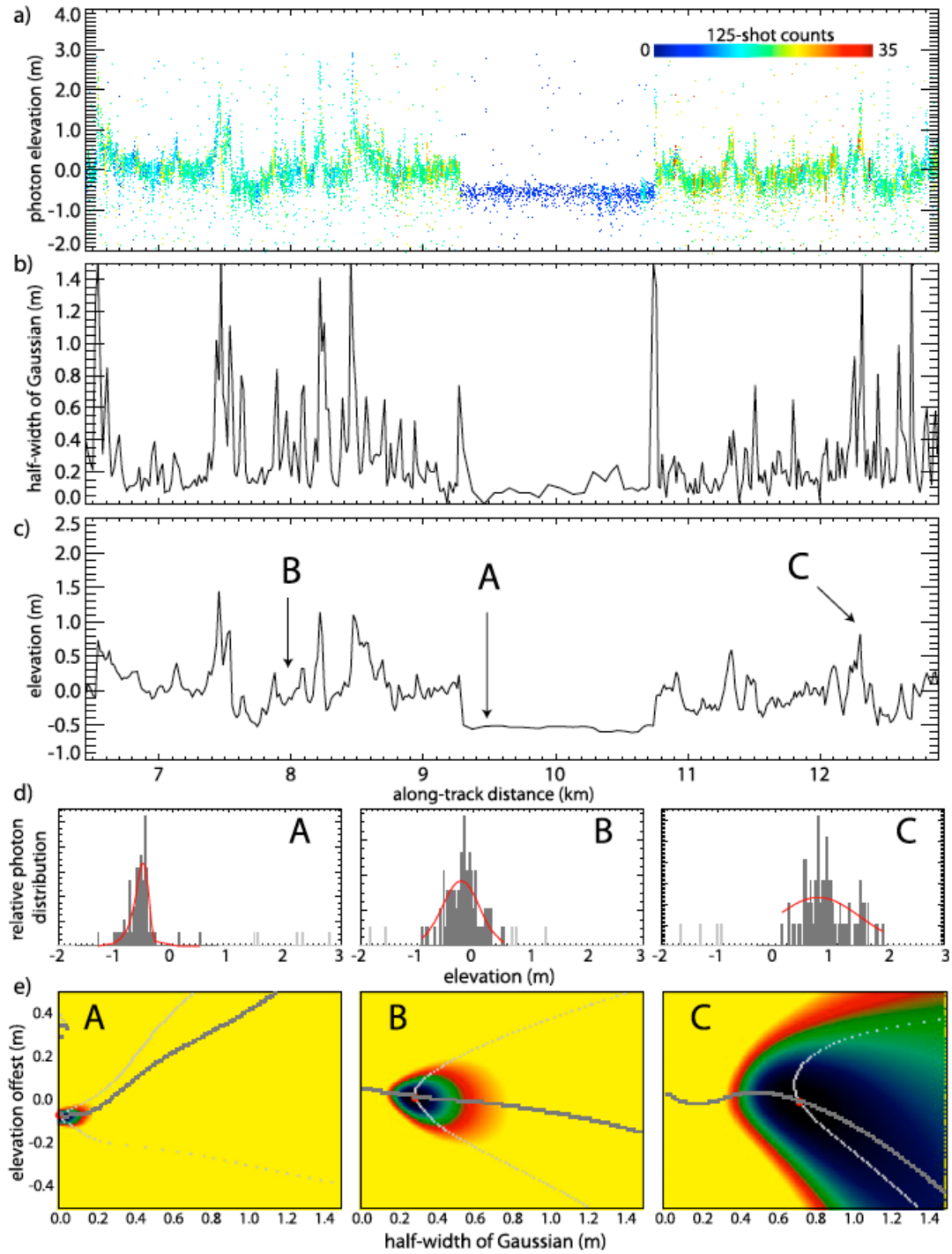

Figure 13 Surface height retrieval using 100 photon aggregates. (a) Photon cloud from a 6.5 km segment of MABEL acquisitions. (b) half-width of Gaussian from retrieval process. (c) Retrieved height. (d) Height distributions and modeled returns (red) (at locations A, B, and C in (c)). (e) Error surface. The light- and dark-gray lines in (e) show the local minima along the x-axis (half-width of Gaussian) and y-axis (elevation offset), respectively. Colors show relative size of the minima. Panels a, b, and c share the same x-axis (labeled in c).

4.2.2.3 Control parameters

Table 5 Control parameters – fine surface finding

Parameter	Description	Value
B_f	bin size of fine histogram	2.5 cm
L	along track segment length	10 km
LB_h_{tab}, UB_h_{tab}	lower and upper bound of h table	[-0.5, 0.5] m
Δh_{tab}	h table spacing	1.0 cm
LB_w_{tab}, UB_w_{tab}	lower and upper bound of w table	[0.0, 1.5] m
Δw_{tab}	w table spacing	1.0 cm
LB_win_s, UB_win_s	window (W_s) containing signal photons	[-2.0, 3.5] m
N_s	photons in W_s	150
N_w	number of standard deviations	2
$N_{specular}$	specular returns	16 photons/pulse (default strong beam)
UB_length_strong	upper bound of segment length – strong beam	200 pulses
UB_length_weak	upper bound of segment length – weak beam	800 pulses
Th_P_c	percentage cloud cover	TBD
h_diff_limit	maximum height difference between the height histogram mean and the initial tracked height	0.2 m
n_photon_min	minimum fraction of photons needed for tracking	0.8
overlap_switch	Use of overlapping height segments (1=yes, 0=no)	1
LB_oc_switch	Lower bound of overlapping control (strong,weak)	(3.0,0.75)
UB_oc_switch	Upper bound of overlapping control (strong,weak)	(9.0,2.25)
n_photon_trim	minimum number of photons for trimming leading/trailing bins	2
~~*TEP_id*~~	~~ID of TEP file used~~	

Note: All threshold parameters are prefixed by *Th.* All upper and lower bound parameters are prefixed by UB and LB, respectively.

4.2.2.4 Dataflow and procedural steps (see dataflow on next page)

A. Pre-generate the following data set:

1. Produce templates of $s_e(h)$ over the search space of interest (i.e., $h_o \in [LB_h_{tab}, UB_h_{tab}]m$, $w \in [LB_w_{tab}, UB_w_{tab}]m$. This table of waveforms, $S_e = S_e(h,w)$, is created by convolving a normalized system impulse response with a family of normalized Gaussian height distributions with varying widths and offsets, representing an expected spectrum of return waveforms (see section 4.2.2.1). Table spacing: $(\Delta h_{tab}, \Delta w_{tab})$. Use TEP recommended in ATL03 for ATL07 processing. The skew correction tables (see Appendix C) are computed on a TBD basis.

B. For each *L*-km along-track segment (strong beam):

1. Remove $\overline{h}_c$ (the *L*-km mean height from the coarse tracker) from all photon heights and keep only those photons within W_s:.
2. Mask pulses where *layer_flag* = 1 (from ATL09).
3. Remove shots with highly specular returns: $N_{ph} > N_{specular}$ photons per shot for strong beams, $> N_{specular}/4$ photons per shot for weak beams, where N_{ph} is the number of photons in a shot with surface confidence level = 3 or 4.
4. Aggregate N_s photons from consecutive along-track pulses to construct height histogram (starting shot = *shot_0*, number of pulses = *n_pulse_seg, length_seg = n_pulse_seg*pulse_spacing*). If number of pulses > *UB_length_strong*, *n_pulse_seg= UB_length_strong,* proceed to step 8.
5. (added to the code as of rel005) keep track of total shots/pulses initially available (*n_pulse_seg_total)* and the number of pulses used to construct the histogram after specular shots are removed (*n_pulse_seg).*
6. Including all photons within the pulse range, construct histogram with bin size B_f over a window W_s.
7. Find the local mode of the histogram. If the mode peak is not in the first or last histogram bin and the total of the histogram is > *n_photon_min** N_s, do the following:
   a. If there is more than one peak, the left most mode is chosen as the assumed surface. Modes further right are assumed to be ice-ridges.
   b. Truncate photons outside window W_s: $[LB_win_s, UB_win_s]$ around the local mode and retain photons that are within 1st - (B_f/2) and nth - (B_f/2) bins.
   c. Calculate moments (mean and standard deviation) of sample population.
   d. Retain the photons that are within $N_w \sigma_c$ of the mean height (this defines *trim_height_bottom, trim_height_top*); this new trimmed distribution is used in the fine surface-finding procedure.
   e. A new height histogram is constructed using the trimmed photons. All bins with fewer than *n_photon_trim* photons before the first and after the last bin with at least *n_photon_trim* photons are removed. If the total of the resulting histogram is > *n_photon_min** N_s then continue:

i. Analyze the waveform with ex_max to find dual-gaussian fit (See Appendix B). If the mean of the 1st Gaussian (*exmax_mn1)* < the mean of the 2nd Gaussian (*exmax_mn2)*, then swap the mean and standard deviation. So the 1st Gaussian mean becomes the 2nd and vise versa.
ii. Save the center bin of the trimmed input waveform to align with the table of expected waveforms, used in the error surface computation. Then trim the table of expected waveforms to match the trimmed input waveform width, with the trim window centered on the table of expected waveforms.
iii. Compute error surface: $e^2(h_o, w)$ as discussed in 4.2.2.1. For reasons of computational load, this is first done at every other point in both dimensions
iv. Determine: $\{\hat{h}_o, \hat{w}\} = \text{argmin}\, e^2(h_o, w) \quad h_o \in [h_1, h_2] \quad w \in [w_1, w_2]$.
v. Steps iv and v are repeated, using a reduced search space, which is a 5×5 set of each expected waveform about the previously calculated minimum.
vi. If $h_o = h_2$ or $w = w_2$, then proceed to step 8.
vii. Refine $\{\hat{h}_o, \hat{w}\}$ by fitting a biquadratic surface to the 3×3 points centered at $\{\hat{h}_o, \hat{w}\}$, and then finding the location of its minimum in the sampled error surface. Note that this step is ignored when: (1) not all 9 points are valid; (2) the surface is too flat (argmin $e^2 < 10^{-5}$); (3) the minimum lies farther than one gridpoint away from the 3×3 center.
viii. Add back $\overline{h}_c$ (removed in step 1) to the height from (vii) to obtain segment height estimate (*height_segment_height)*
ix. Calculate Δh_{corr} to correct for skew of distribution (See Appendix C). Add Δh_{corr} to estimated height.
x. Compute first-photon bias (*fpb_corr*) using procedure described in CAL-19 to calculate the following parameters: apparent width (*fpb_width*, using the untrimmed height histogram), apparent strength (using the *photon_rate* with no adjustments), and average detector dead time (see also Appendix G). Subtract *fpb_corr* from the estimated height.
xi. Compute quality metrics (*h_rms, h_fit_quality_flag*) and statistics of truncated histogram (mean (h_{mean}), median (h_{median}), and standard deviation (*hist_w*)) and error estimate (*height_segment_surface_error_est = hist_w*/sqrt(*n_photons_used*).
xii. Compute photon rates – count signal photons (N_p). The shots filtered for high specular returns (see B.3 above) are not used in this calculation.
xiii. Compute background photon counts (see discussion in 4.2.3).
xiv. Compute apparent surface reflectance (ρ_{app}) for segment (see ATL09 for more details)
xv. If abs(*height_segment_height* - h_{mean}) is greater than *h_diff_lim* and *exmax_mix2* is greater than 0.50, then *height_segment_height =*

exmax_mn2. If not, then if abs(*height_segment_height* - h_{median}) is greater than min[*hist_w,* 0.10m], then *height_segment_height* = h_{median}.

8. Set *height_segment_qual* value: This flag contains information on quality of tracking, cloud conditions, and availability of ocean tides. The quality is considered bad if: *h_fit_quality_flag* less than *LB_qual_flag* or greater than *UB_qual_flag* (see Table 9), or *height_segment_w_gaussian* = UB_w_{tab}, or *layer_flag* =1.
   (**NOTE**: for now, set *layer_flag*=0 for all cases until further examination of the use of the *layer_flag*). We declare a height segment as missing an ocean tide correction if any photon within the height segment has an invalid ocean_tide correction. The *height_segment_qual* value is set as:
   (0) bad quality with ocean tides;
   (1) good quality with ocean tides;
   (2) bad quality without ocean tides;
   (3) good quality without ocean tides.
9. (new for rel005): Set height segment to invalid for any segment that includes an associated *podppd_flag* geoseg (from ATL03) of 1-3 or 5-7 (these indicate degraded geolocation quality, see 4.1.1).
10. Define the beginning shot (*shot_next*) of the next N_s-photon aggregate as:
    If overlap_switch is 1, then *shot_next = shot_0* +(*n_pulse_seg+1*)/2.
    If overlap_switch is 0, then:
    if previous segment photon rate > *LB_oc_control* and < *UB_oc_control*
    then *shot_next = shot_0 + n_pulse_seg*
    else *shot_next = shot_0* + (*n_pulse_seg+1*)/2
    continue from step 3.

C. For weak beams:

1. Location of a weak-beam segment is defined by the center location of each strong-beam height segment.
2. Extend the span of the weak-beam segment (about the shot number at the strong-beam segment center) to include N_s photons within W_s. If number of pulses > *UB_length_weak*, proceed to the next strong beam segment.
3. Construct histogram with bin size B_f centered at the strong beam fine tracker height.
4. Continue from Step 6 through Step 8 in strong-beam procedure above. For the coarse tracker mean and standard deviation in the weak beam, use the strong beam fine tracker segment height and the strong beam coarse tracker standard deviation, respectively.

4.2.3 Background rates (MHz)

The background photon rate is used in the estimation of segment-height error, in refining the ground window, and in the classification of surface type. The source and calculation of background rates are discussed in Appendix D. We also calculate an expected rate based on system parameters.

4.2.3.1 Expected solar background photon rate (clear sky)

Compute expected solar background rate (B_s) with unit reflectivity (R_S=1) using solar background equation in ATL09.

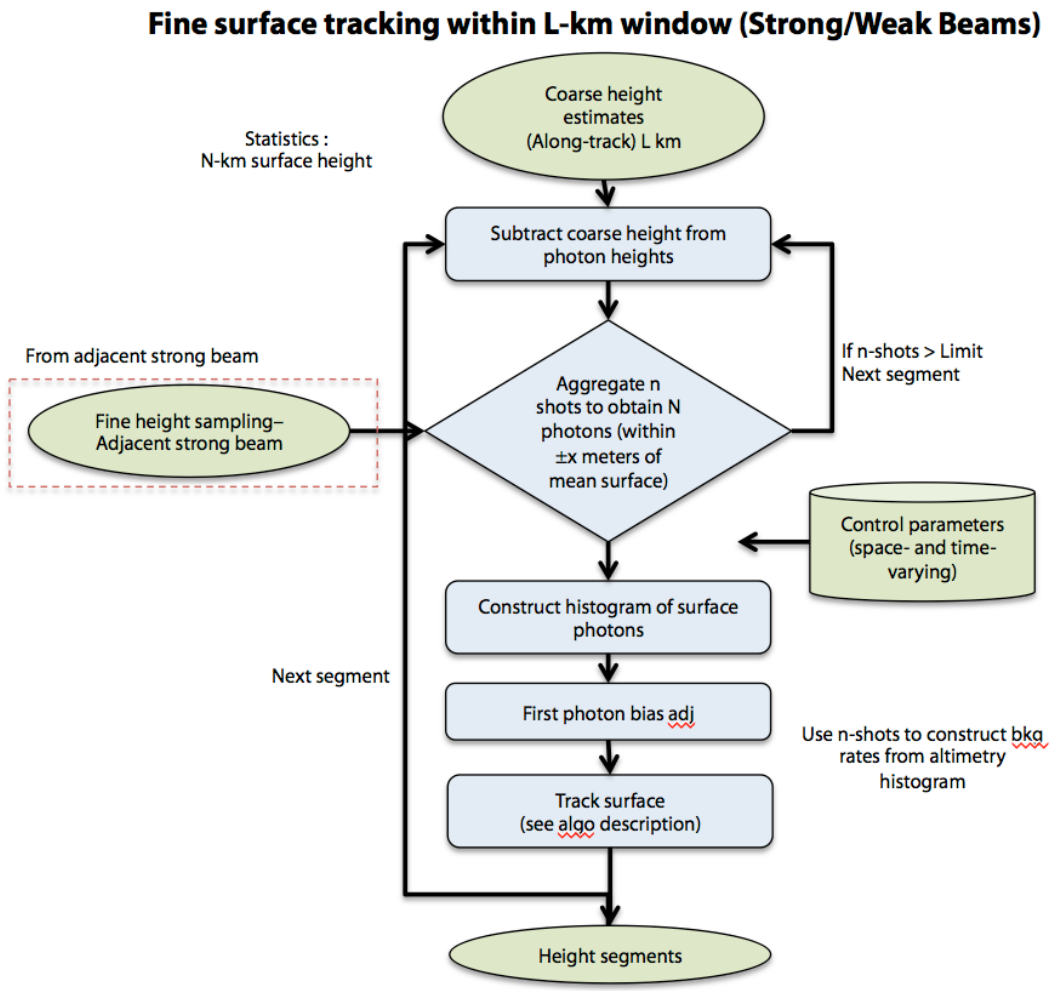

Figure

Figure 14 Flowchart: Fine surface finding.

4.2.4 Surface height histogram statistics and height quality estimates

4.2.4.1 Surface height histogram statistics

Calculate the following moments: *h_mean, h_stdev*

4.2.4.2 Quality estimates

There are 3 height quality metrics defined in Table 8 of section 4.4. They are all calculated during the fine tracking of each aggregate waveform. Note that the convolved waveforms space is defined with dimensions of Gaussian half-width (*w*), (with a window that spans *wlength* = UB_w_{tab} - LB_w_{tab}) and height (*h*) (with a window that spans *hlength* = UB_h_{tab} - LB_h_{tab}). The error surface (*e*, calculated in 4.2.2.4 B.6.e.v) is used to define and calculate the quality metrics as follows:

1. *e_surf_min*: the minimum value of the *e* surface.
2. *h_confidence*: the difference between *e_surf_min* and the mean of the *e* surface excluding a 4-gridpoint band at each edge of the convolved waveforms array (*e_surf_mean*).
3. *h_fit_quality_flag*: (where 1 is best and 5 is poor) This is estimated by calculating the width of the quarter-height of the *e* surface above its minimum in both the *w* and *h* dimensions. The search algorithm for the *e* values is done in 2 steps, the first being done at every other table entry in both *w* and *h*. Using this first location (w_o,h_o), the *e* vectors in both the *w*-direction and *h*-direction about (w_o,h_o) are examined. The parameters *ngrid_w* and *ngrid_h* contain the number of table grid points from (w_o,h_o) to the table locations (both less than and greater than the minimum location) where an *e* value greater than the quarter-height *qtr_h* (= (*h_rms* *3 + *e_surf_mean*)/4) is first reached.

Initialize *h_fit_quality_flag* = -1 (default value when min(*e*) cannot be determined or none of the following conditions are met)

If max(*ssh*[w_o:*wlength*]) >= *qtr_h*, then:
h_fit_quality_flag = 1 if ngrid_w < wlength/2
= 2 if ngrid_w >= wlength/2
If max(*ssh*[w_o:*wlength*]) < *qtr_h*, then:
h_fit_quality_flag = 3 if ngrid_dt < dtlength/2
= 4 if ngrid_dt >= dtlength/2
= 5 if ngrid_dt >= (dtlength-2)

4.2.5 Expected uncertainties in retrieved surface height

In this subsection, we examine the magnitude of the expected uncertainties in the retrieved surface height estimate. The sources of error include:

1. Signal-to-noise considerations in a distribution of photon heights.
2. Deviation of surface height from a Gaussian distribution.
3. Uncertainties in the mean impulse response.
4. First-photon bias.
5. Subsurface scattering.

4.2.5.1 Signal-to-noise considerations/Uncertainties

Here we calculate the expected contributions of background photons and surface roughness to errors in the determination of surface height. The total number of photons (NP_{tot}) in a height window, W, is the sum of the number of signal photons, the background rate (B_s) and the number of pulses (N_{pulses}) within that window:

$$NP_{tot} = NP_{signal} + NP_{bkg}$$

Background photons are uniformly distributed within the height window and thus the standard deviation, σ_{bkg}, can be written as,

$$\sigma_{bkg} = 0.287W \ ,$$

where the factor .287 is the standard deviation of a uniform random variable on a unit interval. The number of background photons (NP_{bkg}) in the window (W) is a Poisson variable with a mean value given by:

$$NP_{bkg} = 2N_{shot}B_s(W/c)$$

If the distribution of the received signal photons is approximately Gaussian, the variance depends on the transmit-pulse width (σ_{pulse}) and the surface roughness (σ_{rough}):

$$\sigma^2_{signal} = \sigma^2_{rough} + \sigma^2_{pulse}$$

The expected composite variance of surface height can then be written as:

$$\sigma^2_{surf} = \frac{NP_{signal}\sigma^2_{signal} + NP_{bkg}\sigma^2_{bkg}}{NP_{signal} + NP_{bkg}}$$

Except for the roughness, all of the quantities in this equation can be estimated from the data: the background and signal photon counts can be estimated from the total number of photons and the background rate. For a relatively smooth flat surface, the expected variance in the estimation of surface height in a window of N_{pulses} can be calculated using:

$$\hat{\sigma}^2_{surf} = \frac{\sigma^2_{surf}}{NP_{tot}} \ .$$

Table 6 shows the expected contributions over a flat lead (with mean returns of ~1 photon per shot) for 100 shots using nominal parameters.

Table 6 Uncertainties in retrieved surface height (100 photons)

Error source	Background = 0 Strong/Weak	Background = 3MHz Strong/Weak
$\hat{\sigma}_{surf}$ Reflectance=0.2 Flat surface	1.0	1.1/1.4
$\hat{\sigma}_{surf}$ Reflectance=0.8 Roughness=0.3 m	3.1	3.2/3.7
Variability in impulse response	TBD	TBD
First-photon bias after correction Reflectance=0.2 Flat surface	~0	~0
First-photon bias after correction Reflectance=0.8 Roughness=0.3 m	1-2 cm	1-2 cm

4.2.6 Correction for skews in the surface height distributions

NB: This skewness correction is currently included as a static correction. We are hoping to eventually have this be calculated dynamically based on the evolving system impulse response, but this is computationally demanding and more testing is needed to understand its possible benefit and inclusion.

The surface finding approach described herein assumes surface returns with an underlying Gaussian height distribution. Thus, deviations of the actual distributions from this surface model would introduce biases in the retrieved height estimates. This assumption of the surface distribution stems from the need to resolve narrow leads (tens of meters) and to address the asymmetry in the superimposed system impulse response. Thus, there are only a limited number of photons that could be used to estimate the higher moments (e.g., skew) of the surface distribution.

For an actual sea ice surface, we expect a non-Gaussian behavior given that the surface height distribution is typically skewed high (i.e., away from the surface) because of ridges. That is, the presence of ridges within a height segment will produce more photons on the right tail of the distribution. In the extreme case of only a single ridge (more likely for a big Arctic ridge), this can appear as a long tail or even as a secondary mode in the observed distribution. Further, the expected skew is dependent on the size of the lidar footprint because ridges are of limited length scale (2-3 m base) and the relative population of photons from ridges decreases as the footprint size increases. Since the MABEL footprint (2 m) is much smaller than that of IS-2 (~17 m), the MABEL data should (on average) represent extremes in surface roughness that IS-2 will encounter.

As measures of deviation of the local distributions from the model of a single Gaussian, ATL07 also provides estimates of the parameters of a two-component Gaussian mixture fitted to the height distributions. The parameters include: means, standard deviations, and mixing ratio of the two-component distribution- $\Delta\tilde{\mu},\tilde{\sigma}_1,\tilde{\sigma}_2,\tilde{\alpha}$; note only the differences between the mean heights or separation between the two distributions are important here. The parameters of the two-component mixture (Fig. 15a) are obtained using an Expectation-Maximization (EM) procedure described in Appendix B. We use these mixture parameters as measures of 'skewness' of the observed distribution.

Here, we examine the two-component mixtures in the height distributions in the MABEL data collected on April 8, 2012. This MABEL data set was selected because it contains a range of surface conditions and includes the highly deformed areas north of the Greenland coast (see Fig. 4). Fig. 15 shows the parameters ($\tilde{\alpha},\Delta\tilde{\mu},\tilde{\sigma}_1,\tilde{\sigma}_2$) of the MABEL distributions from the EM analysis. In our definition, the observed distributions are positive-skewed (i.e., positive is above the surface) when $\tilde{\alpha}$ is greater than 0.5 and vice versa. The mean separation between the two component ($\Delta\tilde{\mu}$) distributions approaches zero when there is very little skew or when $\tilde{\alpha}$ approaches zero. It can be seen in the joint density of ($\Delta\tilde{\mu}$,$\tilde{\alpha}$) (Fig. 15d) from the EM analysis that a significant fraction of the population is located near $\tilde{\alpha}$ ~0.5 and $\Delta\tilde{\mu}$ ~ -0.2 m (Note the square root of the density is used in Fig. 15d to suppress the mode and to emphasize the spatial structure of the distribution away from the mode.) The negative-skewed population (i.e., $\tilde{\alpha}$ < 0.5) has a local mode near $\tilde{\alpha}$ = 0.35 and $\Delta\tilde{\mu}$ ~ -0.2 m, characteristic of returns from relatively flat surfaces. The expected mixture

parameters near this location are those of the negative-skewed system response: these values can be compared with the EM analysis of the MABEL system impulse response, which gives $\tilde{\alpha}$ = 0.34 and $\Delta\tilde{\mu}$ ~ -0.2 m (see right panel in Fig. 15d). The positive-skewed population is due to deformation features above the ice surface. Further, the spatial structure of the density field is asymmetric about $\tilde{\alpha}$ = 0.5; and the estimated heights from the surface finder with $\tilde{\alpha} > 0.5$ are biased because of the assumption of the surface model. In order to correct the biases in the height estimates due to skews in the surface height distributions, we construct a table $(\tilde{g})$ of approximate height corrections (Δh_{corr}) that is a function of the parameters provided by the EM procedure (i.e., $\tilde{\alpha}, \Delta\tilde{\mu}, \tilde{\sigma}_1, \tilde{\sigma}_2$). The corrections are approximate in a sense that the two-component mixture provides only measures of the skew in the distributions described by a two-component mixture rather than that computed from the actual distribution.

The calculation of the approximate corrections is discussed in Appendix C. Fig. 16a shows the height corrections of MABEL data if all of the observed height distributions could be modeled as two component distributions. However, the system impulse response is negative-skewed and so the corrections must be weighted so that they are applied only to distributions that are positive-skewed. We control the transition from negative-skewed distributions (where no corrections are needed) to positive-skewed distributions by a sigmoidal function; the gradient of the function is dependent on $\tilde{\alpha}_1$ (see Appendix C). Fig. 16b shows the weighting functions and Fig. 16c shows the corrections with $\tilde{\alpha}_1$ =0.5. Fig. 16d shows the distributions of height corrections for different values of $\tilde{\alpha}_1$. There is more tapering of the corrections with higher $\tilde{\alpha}_1$. In all cases, the mean correction of all the data is ~1 cm, and the standard deviation is 3-4 cm. For IS-2, we select $\tilde{\alpha}_1$ =0.5 since the transition could be arbitrarily sharp, as the corrections are small (<< 1 cm) in the transition region.

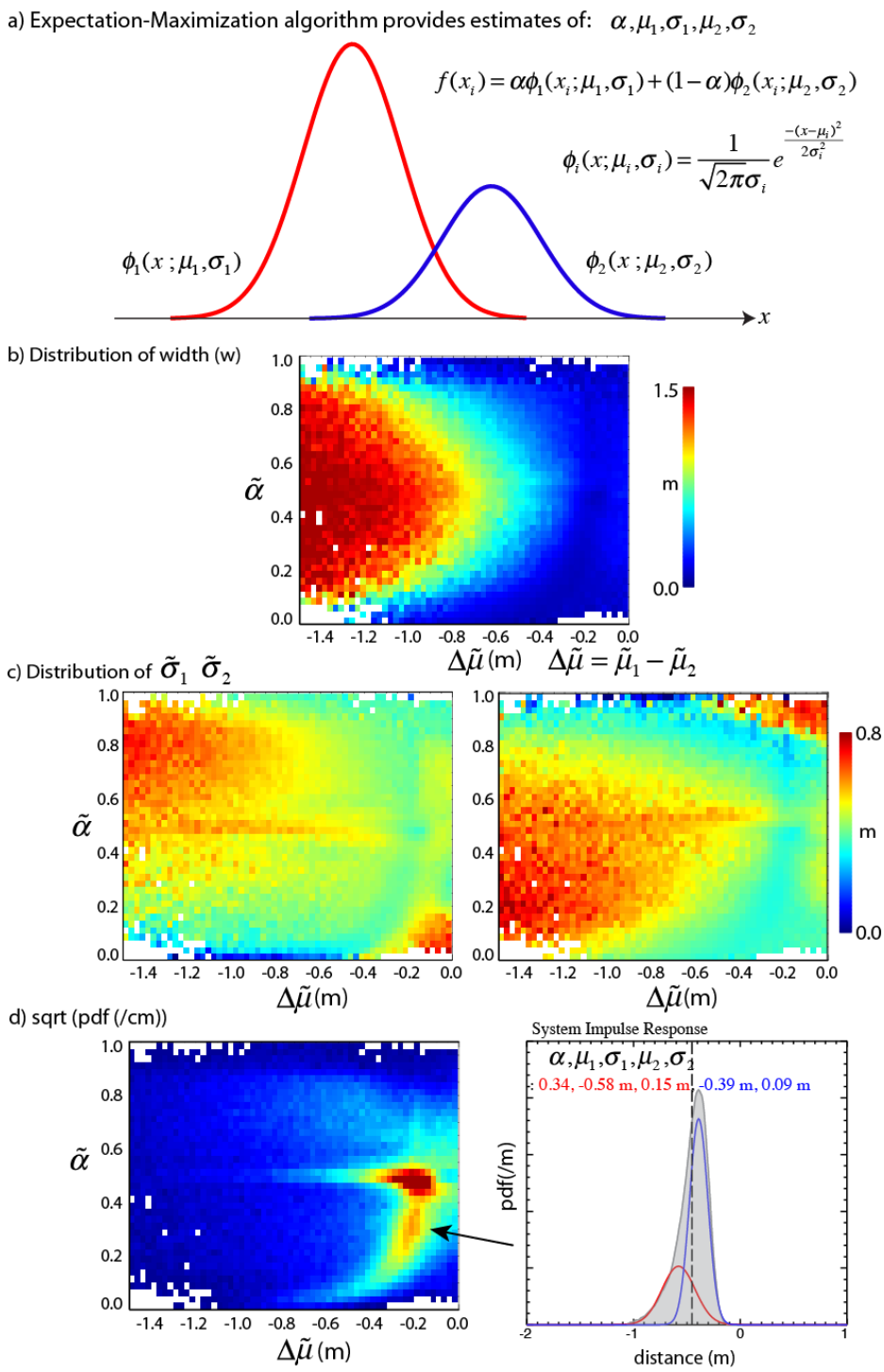

Figure 15. Two-component mixtures in Mabel height distributions (April 8, 2012). (a) Expectation-Maximization (E-M) procedure provides estimates of the parameters in the Mabel height distributions. (b) Distribution of width (w) from the surface finding procedure as a function of $\Delta\mu$ and α from the EM procedure. (c) Distributions of σ_1, σ_2 .(d) Density of population as a function of $\Delta\mu$ and α from the EM procedure, and the location of the impulse response in the two-component space.

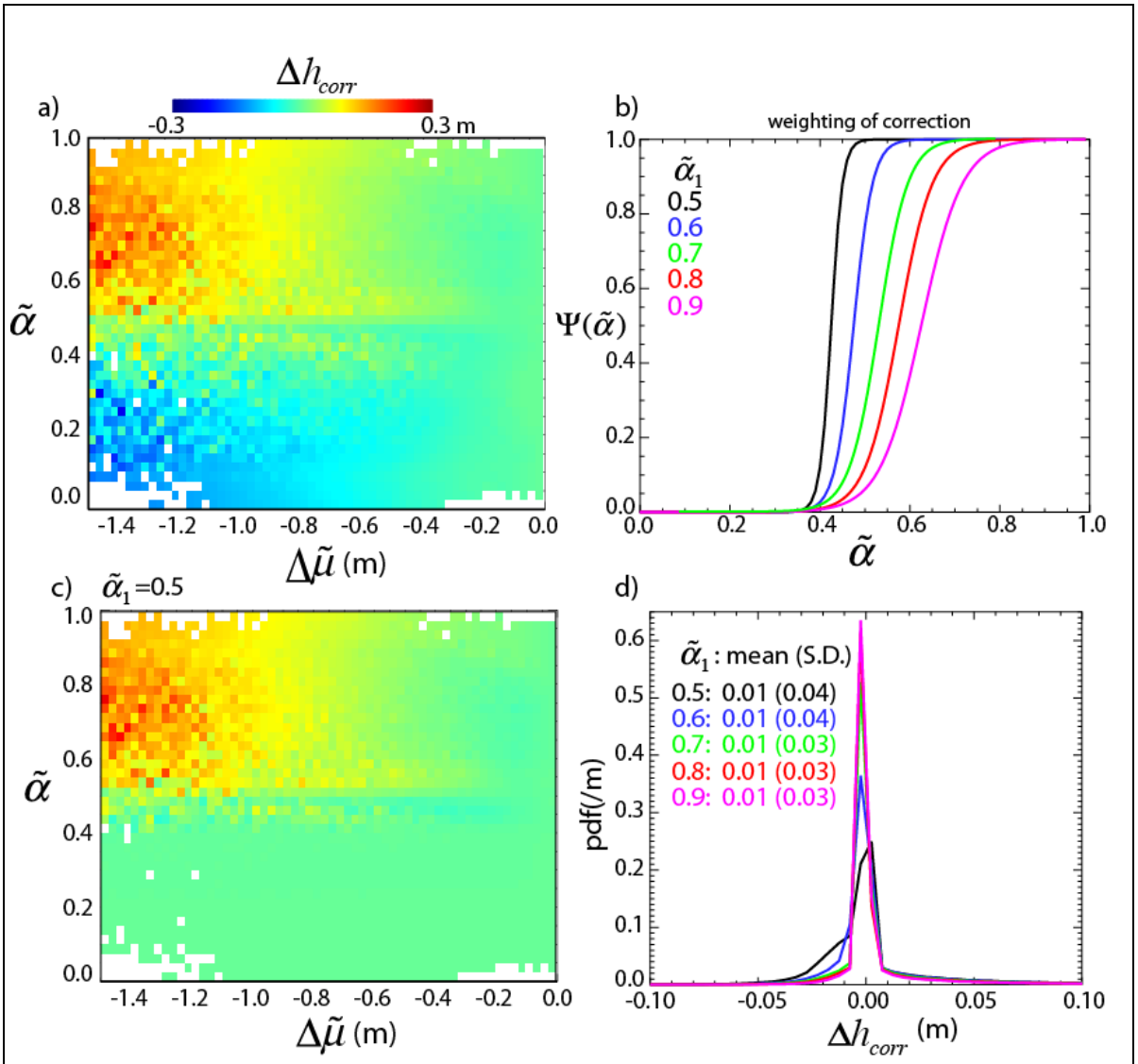

Figure 16 Correction of the estimated height from the surface finding procedure for skew in distribution. (a) Distribution of corrections before accounting for the tail in the system impulse response. (b) Potential weighting functions to account for system impulse response. (c) Distribution of corrections after accounting for the tail in the system impulse response. (d) Distribution of corrections applied to the April-8 data.

4.2.7 Variability in the system impulse response

The system impulse response varies with time and this will be a source of variability in the retrieved heights from the surface finding.

4.2.8 First-photon bias

Table 6 shows the residuals in the corrected first-photon biases for different reflectance and surface roughness.

4.3 Surface classification (Ice/water discrimination)

This section describes how surface types (*seg_surf_type*) and sea surface designations (*SSH_flag*) are assigned to individual height segments. Surface types, together with height statistics, are used to determine whether a given height segment is suitable for use as surface height reference estimates for computing the local freeboard in ATL10. Based on our current understanding of the variability of ice surface signatures in photon counting altimetry, surface type is derived only in certain seasons and regions (see Section 7 for seasonal and geographic bounds for these retrievals).

4.3.1 Basis for surface classification

The decision tree in Fig. 17 addresses the labeling of the height segments in the winter Arctic and Antarctic. The *seg_surf_type* of an individual height segment is labeled based on three parameters: surface photon rate (r_{surf}), the width of photon distribution (or fitted Gaussian - w_s) and background rate (r_{bkg}). The combination of these parameters reduces the ambiguity in the labeling and the possibility of undetected cloud contamination in that segment. Below, we discuss the use of these parameters.

4.3.1.1 Surface photon rate

The surface photon rate (photons/shot) is a measure of the brightness (or apparent surface reflectance) of that height segment. Low surface rates are indicative of water/thin ice in open leads, however specular and quasi-specular returns have been observed from smooth open-water/thin ice surfaces in both ICESat-1 and MABEL. Thus, very high photon rates are expected and these segments are handled differently. In fact, specular returns from these surfaces are especially useful since they provide large numbers of photons for surface finding. In between the two extremes, the surface types are less useful for freeboard calculations but may be of geophysical interest in the general understanding of ice types observed by ICESat-2.

4.3.1.2 Width of the photon distribution

This parameter provides a measure of the surface roughness and serves to partition the height segments within the four ranges of surface photon rates (see Figure 17) into different surface types.

4.3.1.3 Background photon rate

The background rate (MHz) is useful when there are enough photons (i.e., when the solar elevation is high) to provide an accurate rate estimate. For Lambertian surfaces, under clear skies, the surface photon rate should be approximately linearly related to the background rate. When they are not, it is indicative of shadows (cloud shadows or ridge shadows), specular returns, or perhaps atmospheric effects. In the case of specular returns from a dark lead, the near linear behavior would deviate significantly from expected. That is, while the surface photon rate is high the background rate would be very low. In the shadow case, the background would be lower than expected.

The background rate is also related to solar elevation. To define consistent background measure for the determination of the classification types, we us a background rate normalized to a fixed solar elevation angle (r_{bkg_norm}).

When the solar elevation angle (θ) is low, the uncertainty in the estimated background rate is high and this parameter is not used in surface types classification. With only r_{surf}, the uncertainty in labeling increases.

It is anticipated that the classification approach will vary seasonally and regionally in both the Arctic and Antarctic, thus the number of surface types will be dependent on location and time i.e., (X_i, t_j).

The number of surface types (*seg_surf_type*) is 10. At this time:
Surf_type_wo/bkg = [*cloud_covered, dark_lead(smooth), dark_lead(rough), snow_covered, rough, specular1, specular2, unclassified*].
Surf_type_w/bkg = [*cloud_covered, dark_lead(smooth), dark_lead(rough), gray_ice, snow_covered, rough, shadow, specular1, specular2, unclassified]*.
Note:

1. Unclassified: does not fit within a geophysical category

4.3.1.4 Control parameters

Table 7 Control parameters – surface classification (Winter, Spring transition, Summer, Fall transition)

Parameter	Description	Value
θ_{ref}	Solar elevation normalization angle	20 degrees
θ_{nlb}	Solar elevation normalization lower bound	5 degrees
θ_{t}	Solar elevation for controlling use of background rate	*TBD*
beam_gain(N)	Relative gains for beams 1 through 6 where *N* is the beam number (Note: Beams 1, 3, and 5 are the strong beams, see glossary and figure 22)	[1.0, 1.0, 0.82, 1.0, 1.0, 1.0]
P1 (counts/shot)	pr (clouds)	[0.5, 0.5, 0.5, 0.5]
P2 (counts/shot)	pr (dark lead)	[2.5, 2.5, 2.5, 2.5]
P3 (counts/shot)	pr (specular low)	[11.0., 11.0, 11.0, 11.0]
P4 (counts/shot)	pr (specular high)	[14.0, 14.0, 14.0, 14.0]
W1 (meters)	max width (smooth lead)	[0.13, 0.13, 0.13, 0.13]
W2 (meters)	max width (dark rough lead)	[0.17, 0.17, 0.17, 0.17]
B1 (MHz)	max bg (dark ice)	[4.0, 4.0, 4.0, 4.0]
height_pct	Percentile of sorted heights	[0.02, 0.02, 0.02, 0.02]
pr_ratio_extent	Number of segments to examine both before and after a dark lead segment	40
Th_pr_ratio	Minimum photon rate ratio for filtering	1.5

Note:

1. All threshold parameters are prefixed by *Th.* All upper and lower bound parameters are prefixed by UB and LB, respectively.
2. Attention should be paid to the definition of beams and spots: Beams are defined relative to ATLAS while spots are defined relative to the along track direction.

4.3.1.5 Dataflow and procedural steps

Let segment $S_i = \left\{ h_s, w_s, r_{surf}, r_{bkg}, \theta_s \right\}_i$, where

h_s = segment height,

w_s = width of fitted Gaussian

r_{surf} = surface photon rate

r_{bkg} = background photon rate (B_{hs} defined in Appendix D)

θ_s = solar elevation

The steps are as follows:

There are 2 values to be set describing both the radiometric characteristics (*seg_surf_type*) and the sea surface designation (*SSH_flag*) of each segment. Note the bounding parameters are seasonally dependent. For weak beams, P1, P2, P3, and P4 should be divided by 4. Additionally, to accommodate for the differences in returns for each beam, P1, P2, P3, and P4 should be multiplied by relative gain of each beam (*beam_gain*): i.e., Pn = *Pn*beam*_gain(). The steps are as follows:

1. Calculate the normalized background photon rate $r_{bkg_norm} = r_{bkg} * \cos(90-\theta_{ref}) / \cos(90-\min[\theta_s, \theta_{nlb}])$

2. The following surface types (*seg_surf_type*) are defined meeting the given criteria: (All lead types (2 thru 9) must not be at the edge of a data gap):

   0: cloud covered: $r_{surf} \leq$ P1

   2: specular lead (low) w/bkg: P3 $\leq r_{surf} \leq$ P4, $w_s \leq$ W1, $r_{bkg_norm} \leq$ B1, $\theta_s \geq \theta_t$

   3: specular lead (low): P3 $\leq r_{surf} \leq$ P4, $w_s \leq$ W1, $\theta_s < \theta_t$

   4: specular lead (high) w/bkg: $r_{surf} >$ P4, $w_s \leq$ W1, $r_{bkg_norm} \leq$ B1, $\theta_s \geq \theta_t$

   5: specular lead (high): $r_{surf} >$ P4, $w_s \leq$ W1, $\theta_s < \theta_t$

   6: dark lead (smooth) w/bkg: P1 $< r_{surf} \leq$ P2, $w_s \leq$ W1, $r_{bkg_norm} \leq$ B1, $\theta_s \geq \theta_t$

   7: dark lead (smooth): P1 $< r_{surf} \leq$ P2, $w_s \leq$ W1, $\theta_s < \theta_t$

   8: dark lead (rough) w/bkg: P1 $< r_{surf} \leq$ P2, W1 $< w_s \leq$ W2, $r_{bkg_norm} \leq$ B1, $\theta_s \geq \theta_t$

   9: dark lead (rough): P1 $< r_{surf} \leq$ P2, W1 $< w_s \leq$ W2, $\theta_s < \theta_t$

   1: all other segments are non-lead snow/ice surface

   -1: invalid/unknown surface type (see step 5)

3. NOTE: non-winter seasons will still carry the same *seg_surf_type* values but have different associated descriptions (e.g. summer: 0:*same*, 2-5: specular lead/pond, 6-7: smooth dark lead/pond, 8-9:rough dark lead/pond, 1:pond/ice mixture).Calculate e_{min} = minimum (h_{mean} with $w_s \leq$ W1 and not at edge of a data gap)
4. Calculate lead_ht_{max} = maximum value of: (1) the percentile of sorted heights (*height_pct*) of h_s and (2) e_{min} + *height_segment_surface_error_est* x 2

a. Set *ssh_flag* = 1 for segments with 2 ≥ *seg_surf_type* ≤ 5 and h_s ≤ lead_ht_{max}.

5. (new as of rel005) Set surface type (*seg_surf_type*) to invalid (-1) for any segment that includes an associated *podppd_flag* geoseg (from ATL03) of 1-7 (NB: 1-3 and 5-7 indicate degraded geolocation quality, 4 indicates nominal data but during a calibration scan when significant off-pointing can occur, see see Section 4.1.1). Also set surface type (*seg_surf_type*) to invalid (-1) for any segment where the beam incidence angle is greater than a maximum beam incidence angle on the ground (*max_incidence_angle*). We effectively mask the classification procedure for relatively high pointing angles as the algorithm is not currently designed to take this into consideration. Analysis of off-pointing data indicate a lack of specular returns above ~1 degree of incidence angle. Note that *beam_coelev* is first converted to an incidence angle in degrees relative to nadir using: 90 – (180 . *beam_coelev* / π)"

Under development/testing for rel006: After the classification procedure is complete for the entire granule, apply a contrast filter to invalidate classifications for some segments that were classified as dark leads in areas with clouds. More details will be provided once fully tested and implemented.

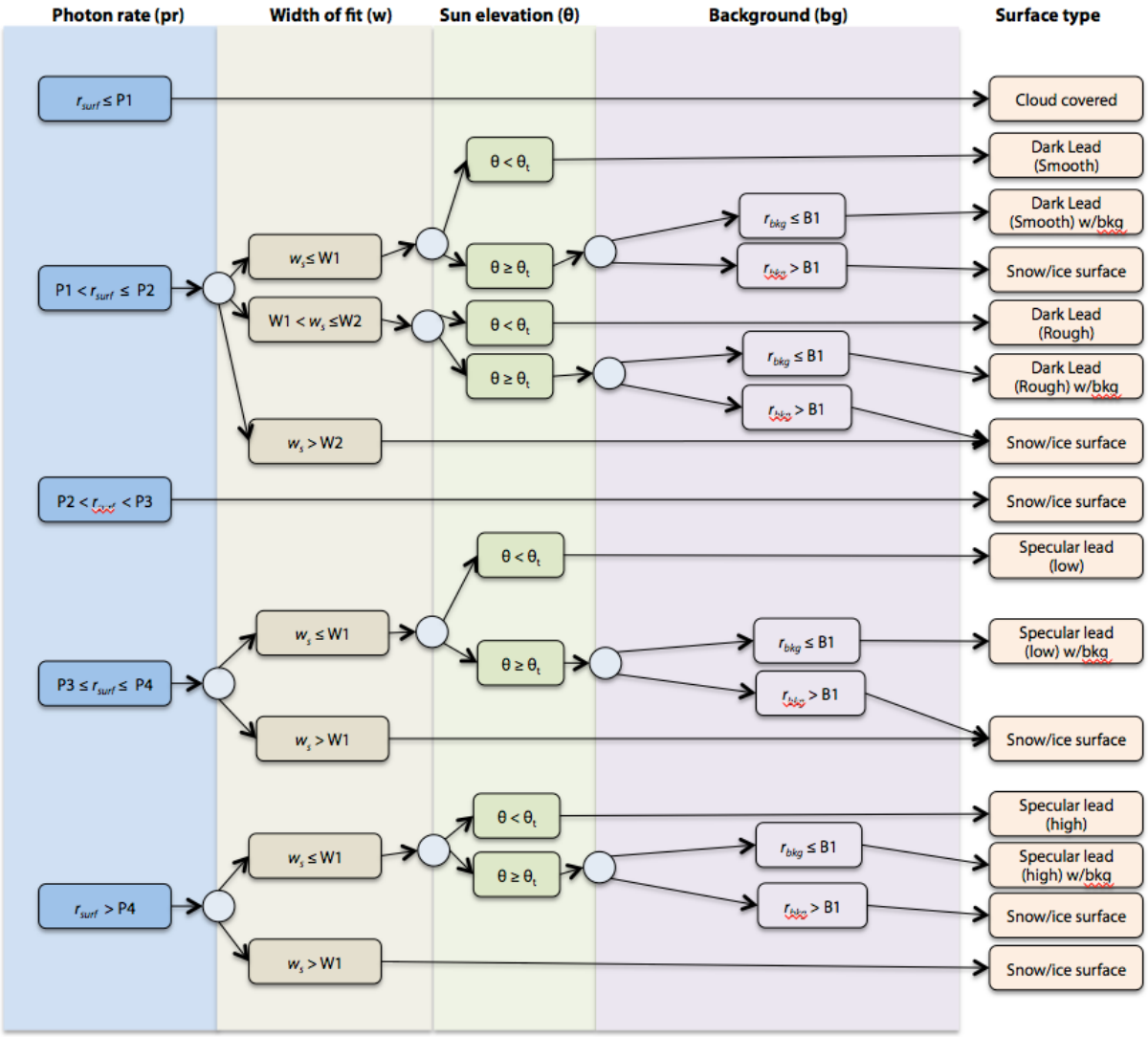

Figure 17 Decision tree: Surface classification (Winter Arctic and Antarctic).

4.4 Output of surface finding algorithm

Table 8 Output to ATL07 (See Appendix A for details of full product dictionary)

Product Label	Description	Symbol
Sea_ice_heights		
height_segment_height	Height of along-track surface segment (MSS and other geophysical corrections applied, tide-free system)	$\hat{h}_o$
height_segment_fit_quality_flag	see Section 4.2.4.2	*h_fit_quality_flag*
height_segment_confidence	see Section 4.2.4.2	*h_confidence*
height_segment_rms	RMS difference between sea ice modeled and observed photon height distribution	*h_rms_diff*
height_segment_surface_error_est	Error estimate of surface height	*h_error_est*
height_segment_length_seg	Length of segment (in meters)	*length_seg*
height_segment_n_pulse_seg_used	Number of laser pulses used in segment (excluding specular shots)	*n_pulse_seg*
height_segment_n_pulse_seg_total	Number of laser pulses (including specular shots) originally available in segment	*n_pulse_seg_total*
height_segment_type	Value that indicates segment surface type as sea ice or different types of ice surface	*seg_surf_type*
height_segment_ssh_flag	Identifies the height segments that are candidates for use as sea surface reference in freeboard calculations in ATL10	*SSH_flag*
height_segment_w_gaussian	width of best fit gaussian	
height_segment_htcorr_skew	Skew correction (not applied to the segment height, as of r004)	
latitude	Latitude, WGS84, North=+, of segment center (mean location of all photons in segment)	
longitude	Longitude, WGS84, East=+, of segment center (mean location of all photons in segment)	
delta_time	time of segment center	
height_segment_asr_casr (apparent reflectance)	Apparent surface reflectivity	
Height_segment_stat		
beam_azimuth	The direction, eastwards from north, of the laser beam vector as seen by an observer at the laser ground spot viewing toward the spacecraft (i.e., the vector from the ground to the spacecraft). When the spacecraft is precisely at the geodetic zenith, the value will be 99999 degrees. 40 Hz.	
beam_coelev	Co-elevation (CE) is direction from the plane of the laser beam as seen by an observer located at the laser ground spot.	
height_segment_podppd_flag	Composite POD/PPD flag from ATL03 that indicates the quality of input geolocation products. Value is set as the highest podppd_flag value from ATL03 associated with this segment. A non-zero value may indicate that geolocation solutions are degraded or that ATLAS is	

	within a calibration scan period (CAL). Possible non-CAL values are: 0=NOMINAL; 1=POD_DEGRADE; 2=PPD_DEGRADE; 3=PODPPD_DEGRADE; possible CAL values are: 4=CAL_NOMINAL; 5=CAL_POD_DEGRADE; 6=CAL_PPD_DEGRADE; 7=CAL_PODPPD_DEGRADE. (Source: ATL02, ANC04, ANC05, ATL03)	
backgr_r_25	Background count rate (25 Hz) from ATL09	*bgr_25*
backgr_r_200	Background count rate (200 Hz)- this is calculated in ATL03 (50 shot counts)	r_{bkg}
background_r_norm	Background count rate (200 Hz) normalized for solar elevation	r_{bkg_norm}
backgr_calc	Expected background count rate based on sun angle, surface slope, unit reflectance	*bgr_calc*
photon_rate	Photon count rate (photons/shot), averaged over the segment	
hist_w	width estimate of photon distribution	H_w
cloud_flag_atm	Number of layers (from ATL09)	*cloud_flag_atm*
cloud_flag_ASR	Cloud flag from ASR (from ATL09)	*cloud_flag_ASR*
msw_flag	multiple scattering warning flag (from ATL09)	*msw_flag*
layer_flag	Combined flag (from ATL09)	*layer_flag*
bsnow_con	blowing snow layer confidence flag	*bsnow_con*
bsnow_h	blowing snow layer height	*bsl_h*
exmax_mean_1	exmax height mean 1	
exmax_mean_2	exmax height mean 2	
exmax_stdev_1	exmax height standard deviation 1	
exmax_stdev_2	exmax height standard deviation 2	
exmax_mix	exmax height mix ratio	
fpb_corr	First photon bias (fpb) correction	*fpb_corr*
fpb_width	FPB correction width	*fpb_width*
fpb_strength	FPB correction strength	*fpb_strength*
fpb_avg_dt	FPB correction average dead time	*fpb_avg_dt*
height_coarse_mn	height mean of coarse tracker	
height_coarse_stdev	height standard deviation of coarse tracker	
height_filter_min	height minimum used in the ssh height filter	
height_filter_05	height fifth percentile used in the ssh height filter	
hist_mean_h	photon heights mean	H
hist_median_h	photon_heights_median	H_{median}
hist_photon_bin_size	height histogram bin size	B_f
hist_photon_bottom	height histogram minimum	H_{min}
hist_photon_heights	photon heights histogram	$H(i)$
hist_photon_top	height histogram maximum	H_{max}
n_photon_actual	Number of photons gathered	N_p
n_photon_define	Number of photons to gather (constant)	

n_photon_used	Number of photons in trimmed histogram	
asr_25	Apparent surface reflectance at 25 Hz (from ATL09)	
solar_azimuth	The direction, eastwards from north, of the sun vector as seen by an observer at the laser ground spot.	
solar_elevation	Solar Angle above or below the plane tangent to the ellipsoid surface at the laser spot. Positive values mean the sun is above the horizon, while negative values mean it is below the horizon. The effect of atmospheric refraction is not included.	
trim_height_bottom	minimum height of trimmed photons	*trim_height_bottom*
trim_height_top	maximum height of trimmed photons	*trim_height_top*

5 ALGORITHM DESCRIPTION: ATL10

Retrieval of freeboard is limited to those seasons and regions where the ice/water discrimination algorithm is able to work reliably.

5.1 Basis for freeboard estimation

(clarification added in rel005): A freeboard estimate is provided for all 'good quality' height segments (see later) and these are not filtered by surface type – e.g., a freeboard estimate (likely near zero) is included even for potential lead/sea surface height segments. Only 'nominal' height segments (e.g. *podppd_flag* = 0) are currently included in ATL10. The algorithm first finds the leads, which consists of collections of height segments that are designated as sea surface height segments (i.e., with *ssh_flag* = 1) in ATL07, and then the leads are used to estimate the height of the reference surface (*refsurf*) for computing the local freeboard over a region of 10-km extent. The relationship between sea surface height segments (*SSHseg*), leads, and the reference surface (*refsurf*) is shown in Fig. 18. The output is a beam section that contains freeboards and freeboard distributions across all six beams (or 3 beam pairs) (see Figure 19).

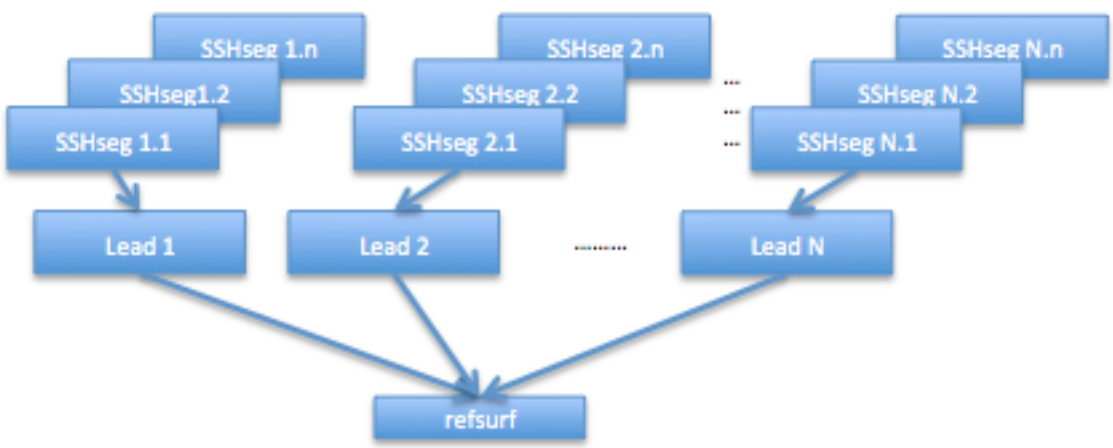

Figure 18 Relationship between sea surface height segments (SSHseg), leads, and the reference surface (refsurf) for computing freeboards

5.1.1 Control parameters

Table 9 Control parameters – freeboard estimation

Parameter	Description	Value
L	along track segment length for freeboard calculations	10 km
LB_N_f	Lower bound on number of SSH estimates	1
B_{fr}	bin size of freeboard histogram	2.5 cm
SSH_slope_UB	Upper bound of SSH slope	*20 cm / 10 km*
n_fillpass	Number of passes for gap filling	*5*
refsurf_sd_fill	Filled *refsurf* stdev estimate	*undefined*
refsurf_slope_fill	Filled *refsurf* slope estimate	*undefined*
LB_frb_hist	Lower bound of freeboard histogram	*0 m*
UB_frb_hist	Upper bound of freeboard histogram	*4 m*
LB_qual_flag	Lower bound of *h_fit_quality flag* for freeboard calculation	*1*
UB_qual_flag	Upper bound of *h_fit_quality flag* for freeboard calculation	*4*
Multibeam_disable_flag	Disable multi-beam (intra-pair and inter-pair) freeboard calculations turned on	*1*
h_offset1	height offset for fill *refsurf* bound check	*0.05*
h_offset2	height offset for fill *refsurf* estimate	*0.03*
fill_UB_width	maximum width for fill segments (width of Gaussian from fine tracking)	*0.10 m*
fill_height_pct	Percentile of sorted heights (in fraction)	*0.02*
fill_snow_depth	snow depth bias for fill segments	*2.0 cm*
max_incidence_angle	maximum beam incidence angle for surface classification/freeboard calculation. If incidence angle (complement of *beam_coelev angle*) is greater than *max_incidence_angle*, height_segment surface type will be set to -1. (Source: ATBD section 4.3.1.4)	*1 degree*

Note: All threshold parameters are prefixed by *Th.* All upper and lower bound parameters are prefixed by UB and LB, respectively.

5.1.2 Dataflow and procedural steps

The sea surface reference (for calculating freeboard) – with mean and error – will first be estimated for each *L*-km segment for each beam. These will then be synthesized across the 6 beams to create a single reference surface (with mean and error estimates) for each *L*-km segment. Freeboards are calculated from the individual height-segments using the sea surface references (per beam and for all the beams).

Note: the weights for the mean and error estimate values are used and computed as follows:

To form a single lead (of consecutive samples of dark leads and specular returns (h_i)) in Step (6):

$$\hat{h}_{lead} = \sum_{i=1}^{N_s} \alpha_i h_i \quad and \quad \hat{\sigma}^2_{lead} = \sum_{i=1}^{N_s} \alpha_i^2 \sigma_i^2$$

$$where \quad \alpha_i = \frac{w_i}{\sum_{i=1}^{N_s} w_i}$$

$$and \quad w_i = \exp\left(-\frac{h_i - h_{\min}}{\sigma_i} \right)^2$$

and h_{min} = minimum height of grouped candidate segments,
N_s = number of samples forming the lead,
σ_i^2 = error variance of each height estimate.

For groups of leads in Steps 7 and 10:

$$\hat{h}_{ref} = \sum_{i=1}^{N_l} \alpha_i \hat{h}^i_{lead(i)} \quad and \quad \hat{\sigma}^2_{ref} = \sum_{i=1}^{N_l} \alpha_i^2 \hat{\sigma}^2_{lead(i)}$$

$$where \quad \alpha_i = \frac{\frac{1}{\sigma^2_{lead(i)}}}{\sum_{j=1}^{N_l} \frac{1}{\sigma^2_{lead(i)}}}$$

and N_l = number of leads in the L-km segment.

The steps are as follows (steps 1 through 13 for each beam)(Check *Multibeam_disable_flag* to see if multi-beam calculations are disabled):

1. Find sea surface tiepoints using candidate lead/sea surface height segment(s) based on surface type (i.e., those labeled as *ssh_flag* = 1) in an *L*-km segment along track (h_{cand}, σ^2_{cand}, n_{cand}).
2. If $n_{cand} < LB_N_f$, go to next *L*-km segment.
3. Calculate surface slope (cm/10 km) and filter as follows:
   a. If $n_{cand} \geq 2$ and the tiepoints span at least half the *L*-km segment, use along track distance (relative to center of *L*-km segment) of the reference surface height-segments to calculate surface slope ($refsurf_slope_{along}$) using a linear fit. Otherwise, set $refsurf_slope_{along}$ to an invalid value.
   b. If the slope is calculated and abs($refsurf_slope_{along}$) > *SSH_slope_UB* then continue to next *L*-km segment.
4. Gather consecutive candidate lead height-segments into groups to identify leads and calculate each lead height mean, error estimate and length (h_{lead}, σ^2_{lead}, n_{lead}, *lead_length*). Label the leads used to calculate the *refsurf* .
5. Calculate the *L*-km segment mean and error estimates of *refsurf* (h_{ref}, σ^2_{ref}) using the lead values (h_{lead}, σ^2_{lead}, n_{lead}).
6. Calculate the center of a given *L*-km segment using along-track distance. Time, latitude and longitude determined by interpolating sea ice segment values to this location.
7. Fill missing gaps in the *refsurf* along-track profile as described in section 5.1.4.
8. Gather all valid height segments (sea ice and lead) for deriving a freeboard estimate – filter height segments with a *h_fit_quality_flag* outside of *LB_qual_flag/UB_qual_flag* and where *seg_surf_type* = -1 (this filters out all non-nominal podppd data).
9. Compute freeboard of all the remaining height-segments using ($refsurf_{seg}$, σ^2_{seg}):
$$h_f = h_{obs} - \hat{h}_{ref}$$
$$\sigma_f^2 = \sigma_h^2 + \hat{\sigma}_{ref}^2$$
10. Compute freeboard of each height-segment in all beams using (h_{ref}, σ^2_{ref}):
$$h_f = h_{obs} - \hat{h}_{ref}$$
$$\sigma_f^2 = \sigma_h^2 + \hat{\sigma}_{ref}^2$$
11. Truncate all negative freeboard values to zero.
    Construct histogram using LB_frb_hist, UB_frb_hist and B_{fr} and compute moments of freeboard that are weighted by *height_segment_length_seg* to control highly specular short segments from skewing the freeboard mean.

    (*rel005 update*) note that the multi-beam steps in the above flow-chart have been removed for clarity, as these are currently not implemented as we await improved beam alignment.

5.1.3 Theoretical uncertainties in freeboard determination

Freeboard is determined by:

$$h_f = h_{ice} - h_{ref}$$

In addition to the measurement error in the determination of $\hat{h}_{ref}$, the geophysical variability of SSH over a swath-segment introduces errors via:

$$\sigma_{ref}^2 = \sigma_{lead}^2 + \sigma_g^2 + \sigma_a^2 + \sigma_T^2 + \sigma_d^2$$

where:

σ_{lead}^2 = variance in the sea surface measurement

σ_g^2 = local residuals in geoid

σ_a^2 = local residuals in atmospheric loading

σ_T^2 = local residuals in tides

σ_d^2 = local residuals in dynamic ocean topography

If σ_{ice}^2 is the expected variance of the ice surface height based on 150 photons, then the uncertainty in freeboard for an individual height segment, assuming that the sea surface height residuals are zero can be calculated as (*N* is the number of lead measurements):

$$\sigma_f^2 = \sigma_{ice}^2 + \frac{\sigma_{lead}^2}{N} \quad \sigma_g^2 + \sigma_a^2 + \sigma_T^2 + \sigma_d^2 = 0$$

.

If we take σ_{lead} =~1.5 cm (i.e., low reflectance surface with background of 3 MHz), *N*=1 and σ_{ice} = ~3 cm, then σ_f = 3.4 cm. If $\sigma_g^2 + \sigma_a^2 + \sigma_T^2 + \sigma_d^2$ were random over the length scale used for freeboard calculations, then:

$$\sigma_f^2 = (\sigma_{ice}^2 + \sigma_g^2 + \sigma_a^2 + \sigma_T^2 + \sigma_d^2) + \frac{\sigma_{lead}^2 + \sigma_g^2 + \sigma_a^2 + \sigma_T^2 + \sigma_d^2}{N}$$

This above equation assumes that the errors are random locally, which is typically not the case at the length scale of the swath-segments. In fact, most of the errors are surface tilts that are of longer wavelengths (except perhaps for eddies – but their number and surface expression should be considered if they should be a constraint on length scale) than the length of a swath segment (10-20 km), and surface tilts due to tides and dynamic ocean topography (DOT) are space- and time-varying, and therefore difficult to construct a rational error budget. Further the errors are also dependent on the location of the leads within the swath segment. If the leads (that provide the reference levels) were located near the edge of a tilted surface, then there would be a net bias in the freeboards. If the leads were at the center, the net mean freeboard error within that swath segment would be zero but the variance would be correlated with the uncompensated tilt.

Table 10 Uncertainties due to surface tilts

Source	Worst case tilt	Remarks
σ_g	4.3 cm	High over deep ocean ridges – up to 15 cm/10 km
σ_a	< 1 cm	
σ_T	< 1 cm	
σ_d	1-2 cm (?)	Higher errors along coast and shelves

5.1.4 Procedure to filter and fill missing surface reference (*refsurf*) estimates along track

Table 11 Control parameters – for filtering/filling of along-track reference surface estimates

Parameter	**Description**	**Value**
min_land_dist	minimum distance from land	25 km
ic_thresh1	minimum ice concentration	0.5
ic_thresh2	Reference surfaces estimates filtered below this ice concentration	0.8
ht_thresh1	*refsurf* height difference threshold for low concentration cases	0.1 m
ht_thresh2	*refsurf* height difference threshold for consecutive estimates	0.5 m
maxgaptime	Maximum allowable time gap for interpolation	30 (seconds)
maxgapht	Allowable height separation between ref_surf heights across time gap	0.05 m
LB_refsurf	Lower bound of *refsurf* [Arctic:Winter,Spring,Summer,Fall, Antarctic: Winter,Spring,Summer,Fall]	[-0.5, -0.5, -0.5, -0.5, -1.0 ,-1.0, -1.0, -1.0] m
UB_refsurf	Upper bound of *refsurf* [Arctic:Winter,Spring,Summer,Fall, Antarctic: Winter,Spring,Summer,Fall]	[0.5, 0.5, 0.5, 0.5, 1.0, 1.0, 1.0, 1.0] m
min_refsurf_count	ATL10 granules with less than this number of non-interpolated strong beam reference surface sections will be marked as failed. (Source: Sea Ice ATBD)	9
min_segs_count	ATL10 granules with less than this number of strong beam freeboard sea ice segments will be marked as failed. (Source: Sea Ice ATBD)	1500

The reference surfaces used to calculate the ice freeboard are based on sea surface heights from ATL07. Erroneous reference surfaces are filtered out (below procedure) by identifying the conditions where the reference surface observations are near to land and in areas of low ice concentration. Near the ice edge, the reference surfaces are affected by sea state, resulting in surfaces that can be many 10's of centimeters below the local mean sea surface.

The first filter is to remove any reference surface (*refsurf*) < LB_*refsurf* or > UB_*refsurf*. The next filtering procedure is designed to use collections of reference surfaces within an ATLAS Subproduct region (approximately 20 degrees of latitude). Since multiple ATL03 granules can be processed into one ATL07 and ATL10 granule, we use the defined latitude boundaries and increasing/decreasing latitudes (i.e., ascending/descending tracks) in time to delineate these regions. Analysis of reference surfaces in the northern hemisphere are performed within the following latitudinal bounds: (1) 27 < *latitude* < 60 and *Δlatitude* increasing (ascending tracks); (2) 60 < *latitude* < 80 and *Δlatitude* increasing (ascending tracks); (3) *latitude* > 80 ; (4) 60 < *latitude* < 80 and *Δlatitude* decreasing (descending tracks); (5) 27 < *latitude* < 60 and *Δlatitude* decreasing (descending tracks). Analysis of reference surfaces in the southern hemisphere are performed within the following latitudinal bounds: (1) -79 < *latitude* < -50 and *Δlatitude decreasing* (descending tracks); (2) -79 < *latitude* < -50 and *Δlatitude* increasing (ascending tracks).

The procedure is as follows (for each beam):

1. Filter the valid reference surfaces using the following procedure:

For each reference surface observation (*refsurf*), mark as invalid if < LB_*refsurf* or > UB_*refsurf*. If it passes this filter, determine its distance-to-land from the appropriate map. If distance-to-land < *min_land_dist*, tag that *refsurf* as invalid.
If the ice concentration at the *refsurf* location < *ic_thresh1*, tag that *refsurf* as invalid.
For the remaining valid *refsurf* values, identify the height of the maximum *refsurf* in the granule (max_refsurf_ht). For each *refsurf*, determine the lowest height of the leads (min_lead_ht) that were used in the *refsurf* calculation. If refsurf_iceconc < *ic_thresh2* and (max_refsurf_ht - min_lead_ht) > *ht_thresh1*, tag that *refsurf* as invalid.
For the remaining valid *refsurf* values, calculate all consecutive *refsurf* height differences (Δh). For all refsurf pairs where Δh > *ht_thresh2*, tag the lower of the 2 *refsurf* values as invalid. Repeat this step until there are no more large Δh values.

2. Identify gaps and estimate their *refsurf* as follows:
    a. Set beam_refsurf_interp_flag= 0 for all refsurf segments.
    b. Identify gaps between valid *refsurf*. If the time span of the gap (gapsize) < *maxgaptime* and the absolute value of the *refsurf* height difference across the gap (htgap) < *maxgapht*, fill all of the missing *refsurf* in the gap using linear interpolation between the two valid *refsurf* heights. Set *beam_refsurf_interp_flag*=1 for the interpolated *refsurf's*.
    c. Set *beam_refsurf_interp_flag*= -1 for segments without a valid or filled reference surface.
    d. Put in the *refsurf_sd_fill* and *refsurf_slope_fill* values for the filled segments.
    e. For all of the observed and interpolated *refsurf*, run a 3-point smoother.

3. Set */gtxx/freeboard_beam_segment/height_segments/height_segment_ssh_flag*=2 for all

height segments where:
(1) initial *height_segment_ssh_flag*=1; (2) the segment *beam_refsurf_interp_flag* = 0, and (3) the segment *beam_refsurf_height* is valid.

4. (new in rel005) Determine latitude/longitude of interpolated reference surfaces using nearby available reference surfaces. Find along-track pointing vector using consecutive along-track reference surfaces and use this pointing vector to estimate latitude/longitude of interpolated reference surfaces. This pointing vector can be rotated by 90 degrees to determine latitude/longitude of across track interpolated reference surfaces. Previously these were erroneously calculated using multi-beam interpolation causing inconsistent times/locations of the reference surfaces.

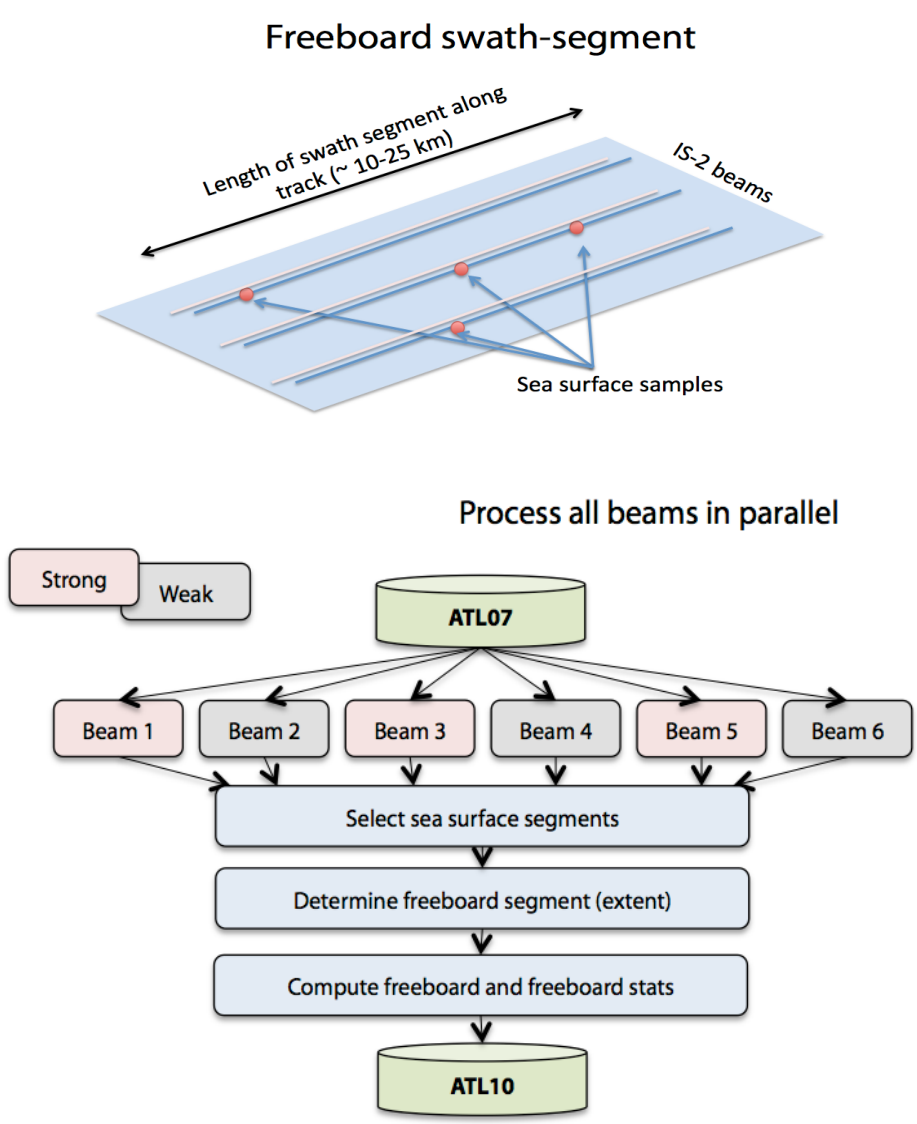

Figure 19 Freeboard estimation

5.2 Output of freeboard estimation algorithm

Table 12 Output to ATL10 (See Appendix A for full product dictionary)

Product Label	Description	Symbol
freeboards (per height segment per beam)		
beamnum	Beam identifier	
latitude	Latitude, WGS84, North=+, of segment center	*ctrlat*
longitude	Longitude, WGS84, East=+, of segment center	*ctrlon*
delta_time	time of segment center	*ctrtime*
beam_fb_height	Freeboard height relative to *beam_refsurf_height*	h_f
beam_fb_sigma	Freeboard height standard deviation	σ_f
beam_fb_confidence	Freeboard confidence	*fb_confidence*
beam_fb_quality_flag	Flag describing the quality of the freeboard estimate	
height_segment_height	Mean height from along-track segment fit determined by the sea ice algorithm (from ATL07)	*h*
height_segment_rms	RMS difference between sea ice modeled and observed photon height distribution (from ATL07)	*h_rms_diff*
height_segment_confidence	Confidence level in the surface height estimate based on the number of photons; the background noise rate; and the error analysis (from ATL07)	*h_confidence*
height_segment_w_gaussian	width of best fit Gaussian (from ATL07)	*w_gaussian*
height_segment_id	Identifier of each height segment (from ATL07)	
height_segment_length_seg	Length of segment (from ATL07)	
height_segment_ssh_flag	Identifies segments used as sea surface references (from ATL07)	
beam_lead_ndx	Index first lead	
beam_lead_n	Number of leads	
Geophysical (per height segment per beam)		
height_segment_dac	Dynamic Atmosphere Correction	
height_segment_earth	Earth Tide	
height_segment_geoid	EGM2008 Geoid	
height_segment_load	Load Tide	
height_segment_mss	Mean Sea Surface	
height_segment_ocean	Ocean Tide	
height_segment_lpe	Long period equilibrium Tide	
height_segment_tide_pole	Pole Tide	
height_segment_ib	Inverted Barometer Effect	
refsurf **(per beam)**		
delta_time	time of segment center	
latitude	Center latitude of reference surface	
longitude	Center longitude of reference surface	
beam_refsurf_height	reference surface mean	h_{ref}

beam_refsurf_sigma	reference surface uncertainty	σ_{ref}
beam_refsurf_alongtrack_slope	reference surface along track slope	
beam_refsurf_interp_flag	reference surface interpolation flag	
beam_refsurf_mss	mss calculated at the L-km segment scale	$h_{ref\text{-}mss}$
beam_refsurf_geoid	geoid calculated at the L-km segment scale	$h_{ref\text{-}geoid}$
leads **(per beam)**		
delta_time	time of segment center	
latitude	Center latitude of lead	
longitude	Center longitude of lead	
ndx_refsurf	beam refsurf index first	
n_refsurf	Number of refsurf	
ndx_fbswath_segment	Swath Segment index first	
n_fbswath	Number of Swath segments	
lead_sigma	Lead uncertainty estimate	
lead_height	Lead height	
lead_length	Lead size	
ssh_ndx	index first sea surface	
ssh_n	number of sea surface references	

6 ALGORITHM DESCRIPTION: GRIDDED FREEBOARD (ATL20) AND SEA SURFACE HEIGHT (ATL21)

In this section, we describe the procedure for gridding the sea ice freeboard and sea surface height.

6.1 Gridded fields of freeboard and sea surface height

The gridded fields are constructed for two time-spans (daily and monthly) and two parameters (sea ice freeboard and sea surface height (SSH)) with a grid spacing defined by the parameter *Grid-space* below). The estimates of sea ice freeboard and sea surface height are from the ATL10/L3A granules. These products are constructed with data aggregated from the selected beams (*ATL20-beams*, Table 13); the monthly span is defined by the beginning and the end of each month. The Cartesian grid is specified by the mapping parameters of the commonly used SSM/I polar stereographic projection (Appendix E).
There are two files for each month (for freeboard and SSH anomalies), one for the Northern Hemisphere and one for the Southern Hemisphere. Each file contains a gridded monthly composite and the gridded daily composites.

6.1.1 Control parameters

Table 13 Control parameters – Gridded products

Parameter	Description	Value
Grid-space	Grid Spacing	25 km
ATL20-beams	List of beams used to derive ATL20 (1,3,5 are the strong beams; 2, 4, 6 are the weak beams)	1, 3, 5
ATL21-beams	List of beams used to derive ATL21	3
ATL21-refsurf-ints	List of reference surface interpolation flags (*beam_refsurf_interp_flag*) used to derive ATL21 (0, 1, 2, 3)	0, 1, 2

6.2 Dataflow and procedural steps (ATL20)

1. Daily gridded fields of total freeboards are constructed as follows:

Collect all the individual *freeboard beam segments* for all of the chosen for all of the chosen beams (*ATL20-beams* in Table 13) that are within the time-span of interest. Do not use ATL10s that have failed or been held (see Section 9). The parameter *h* in the following calculations is the *beam_fb_height* in the *gtx/freeboard_beam_segment/beam_freeboard* group.
For each grid cell (*x, y, D*), where *D* is day-of-month, the following parameters are computed:

$$\overline{L}(x,y,D) = \sum_N L_s^i$$

$$\overline{h}(x,y,D) = \frac{\sum_N L_s^i h_s^i}{\sum_N L_s^i}$$

$$\sigma^2(x,y,D) = \frac{\sum_N L_s^i (h_s^i)^2}{\sum_N L_s^i} - \bar{h}^2(x,y,D)$$

L is length of a given (i) freeboard segment (*height_segment_length*), N is the number of freeboard segments in the given daily grid-cell.

2. Monthly gridded fields are constructed as follows:

Each cell contains the following – computed from the daily composites:

$$\bar{L}_M(x,y) = \sum_D \bar{L}(x,y,d)$$

$$\bar{h}_M(x,y) = \frac{\sum_D \bar{h}(x,y,d)\bar{L}(x,y,d)}{\sum_D \bar{L}(x,y,d)}$$

$$\sigma_M^2(x,y) = \frac{\sum_D \bar{L}(x,y,d)(\sigma^2(x,y,d) + \bar{h}^2(x,y,d))}{\sum_D \bar{L}(x,y,d)} - \bar{h}_M^2(x,y)$$

$$N_M(x,y) = \sum_D N(x,y,D)$$

Table 14: Key variables output to ATL20 (See Appendix A for full product dictionary)

Product Label	Description	Symbol
grid_lat	Grid cell center latitude	
grid_lon	Grid cell center longitude	
grid_x	Grid cell center X value in projection grid	x
grid_y	Grid cell center Y value in projection grid	y
land_mask_map	Gridded map identifying each grid cell as land (=1) or ocean/sea ice (=0).	
daily/dayxx		
mean_fb	Grid of daily mean freeboard	$\bar{h}$
n_segs	Number of sea ice segments for each daily grid cell	N
length_sum	Sum of freeboard segment lengths for each daily grid cell	$\bar{L}$
sigma	Standard deviation of freeboard segments in each daily grid cell	σ
monthly		
mean_fb	Grid of monthly mean freeboard	$\bar{h}_M$
n_segs	Number of sea ice segments in each monthly grid cell	D
length_sum	Sum of freeboard segment lengths in each monthly grid cell	$\bar{L}_M$
sigma	Standard deviation of freeboards in each monthly grid cell	σ_M

6.3 Dataflow and procedural steps (ATL21)

1. Daily gridded fields of polar sea surface height anomalies are constructed as follows:

Step 1 (compile additional height correction data): Read in the MSS and geoid from ATL10 that have been sampled at the *L*-km reference surface scale (updated in rel005 as these variables are now available in ATL10). This is required to generate equally sampled estimates of the MSS and geoid , enabling users to remove these corrections in either ATL10 or ATL21 product without introducing sampling biases.

Repeat steps in Section 5.1.2 (Steps 4-6), but replacing the segment height *h* with the mean sea surface h_{mss} (*height_segment_mss*) and geoid $h_{ref\text{-}eoid}$ (*height_segment_geoid*) to produce new estimates of $h_{ref\text{-}mss}$ and $h_{ref\text{-}geoid}$ leveraging the lead indices already calculated.

Note that the rel004 ATL07 and ATL10 sea ice products were converted to a 'tide-free' system to be consistent with ATL03 (which includes the time-varying and permanent solid-earth tide correction and also passes through a tide-free geoid to the higher-level products, see Section 3.1.3). The conversion of sea ice products to a consistent 'tide-free' system simply involved the transformation of the MSS (which was originally provided in the mean-tide system) to tide-free by subtracting a geoid_free2mean conversion factor (as of rel005, see the new Geophysical Corrections for ICESat-2 Sea Ice Products user guide). We opt to put ATL21 in a mean-tide system as this is the more physically representative system from which one can then derive geophysical quantities such as Dynamic Ocean Topography. This is also consistent with ATL19 (gridded ocean height) which will be in the mean-tide system.

To make this conversion we add the solid earth permanent tide correction and subtract the geoid free to mean correction from the tide-free reference surface heights:

$$h_{ref}(\text{mean-tide}) = h_{ref}(\text{tide-free}) + \text{height_segment_earth_free2mean} - \text{height_segment_geoid_free2mean}$$

and then add the geoid free2mean correction to both the MSS and geoid as

$$h_{ref\text{-}mss}(\text{mean-tide}) = h_{ref\text{-}mss}(\text{tide-free}) + \text{height_segment_geoid_free2mean}$$
$$h_{ref\text{-}geoid}(\text{mean-tide}) = h_{ref\text{-}geoid}(\text{tide-free}) + \text{height_segment_geoid_free2mean}$$

Step 2 (gridding): Collect all reference sea surface heights h_{ref} where the associated reference surface interpolation flag (*beam_refsurf_interp_flag*) is provided in the list of permissible interpolation flags (*ATL21-refsurf-ints*, Table 13) for all of the chosen beams (*ATL21-beams* in Table 13) within the time-span of interest. Do not use ATL10s that have failed or been held (see Section 9). Repeat for the MSS and geoid. The parameter *h* in the following calculations represents the *beam_refsurf_height* (h_{ref}), *beam_refsurf_mss* ($h_{ref\text{-}mss}$) and the *beam_refsurf_geoid* ($h_{ref\text{-}geoid}$) in the *gtx/freeboard_beam_segment* group.

For each grid cell (*x, y, D*), where *D* is day-of-month and *x/y* are the grid indices, the following parameters are computed:

$$\overline{h}(x,y,D) = \frac{\sum_N h_s^i}{N}$$

$$\sigma^2(x,y,D) = \frac{\sum_N (h_s^i)^2}{N} - \bar{h}^2(x,y,D)$$

N is the number of *beam_refsurf_height* L-km sections in the given daily grid-cell. Unlike ATL20, no length weighting is applied – i.e. all L-km reference sea surface heights are given equal weight (they should all be roughly equal length).
In the first ATL21 release we default to using just the middle strong beam as beam alignment efforts are still on-going (see ATL20/21 Known Issues for a more detailed summary).

2. Monthly gridded fields are constructed as follows:
Each cell contains the following – computed from the daily composites:

$$\bar{h}_M(x,y) = \frac{\Sigma_D \bar{h}(x,y,D)}{N_D}$$

Table 15 Key variables output to ATL21 (See Appendix A for full product dictionary)

Product Label	Description	Symbol
grid_lat	Grid cell center latitude	
grid_lon	Grid cell center longitude	
grid_x	Grid cell center X value in projection grid	x
grid_y	Grid cell center X value in projection grid	y
land_mask_map	Gridded map which describes each grid cell as land (=1) or ocean/sea ice (=0).	
daily/dayxx		
mean_ssha	Mean Sea Surface Height Anomaly (SSHA) for each daily grid cell. Sea surface height anomaly expressed relative to the mean sea surface (other geophysical corrections also applied, as indicated in the ATBD) using the reference surface heights. Converted to a mean-tide system (see ATBD Section 6.2).	$\bar{h}$
mean_weighted_mss	Mean of the Mean Sea Surface (MSS) values sampled at each reference surface height location used in the daily grid cell. MSS is expressed relative to the WGS-84 reference ellipsoid from a DTU/CS-2 merged product (https://doi.org/10.5281/zenodo.4294047) and has been converted back to a mean-tide system (originally converted to tide-free in ATL07/10, see ATBD Section 6.2).	
mean_weighted_geoid	Mean of the geoid values sampled at each reference surface height location used in the daily grid cell. Geoid is expressed relative to the WGS-84 reference ellipsoid from EGM2008 and has been converted to a mean-tide system (see ATBD Section 6.2).	
n_segs	Number of reference surface segments used in each daily grid cell	
sigma	Standard deviation of reference surface heights in daily grid cells.	
mean_weighted_earth_free2mean	Mean of the solid earth tide free-to-mean conversion correction sampled at each reference surface height location used in the daily grid cell.	

mean_weighted_geoid_free2mean	Mean of the geoid free-to-mean conversion correction sampled at each reference surface height location used in the daily grid cell.	
monthly		
mean_ssha	Mean Sea Surface Height Anomaly (SSHA) for each monthly grid cell. Sea surface height anomaly expressed relative to the mean sea surface (other geophysical corrections also applied, as indicated in the ATBD) calculated as the mean of all available daily *mean_ssha* values and is in a mean-tide system.	$\bar{h}_M$
mean_weighted_mss	Mean monthly MSS calculated from all available daily *mean_weighted_mss* values. MSS is expressed relative to the WGS-84 reference ellipsoid from a DTU/CS-2 merged product (https://doi.org/10.5281/zenodo.4294047) and is in a mean-tide system.	
mean_weighted_geoid	Mean monthly geoid calculated from all available daily *mean_weighted_geoid* values. Geoid is expressed relative to the WGS-84 reference ellipsoid from EGM2008 and is in a mean-tide system.	
n_segs	Number of reference surface segments used in each monthly grid cell	
sigma	Standard deviation of reference surface heights in daily grid cells.	
mean_weighted_earth_free2mean	Mean solid earth tide free-to-mean conversion correction calculated from all available daily mean_weighted_earth_free2mean values.	
mean_weighted_geoid_free2mean	Mean geoid free-to-mean conversion correction calculated from all available daily mean_weighted_geoid_free2mean values.	

7 ALGORITHM IMPLEMENTATION CONSIDERATIONS

This section addresses implementation details including:

1. Multi-beam architecture.
2. Product coverage (ATL07 and ATL10).
3. Parameters required by the algorithms that are produced by the ICESat-2 project or from an external source.

7.1 Multi-beam Architecture: Surface Finding/Classification

The earlier sections described the elements (surface finding and classification) required to produce the ATL07. Here we show how these elements are combined into a multi-beam architecture to produce ATL07 (Figure 20).
Note that the multi-beam 'swath' reference surface/freeboard calculations are currently disabled as work is on-going to understand inter-beam biases.
Implementation notes:

1. Process strong beams first, then the associated weak beams. The center location/surface height of each strong beam height segment is used to determine the center location (closest distance) and the initial coarse surface height of each weak beam height segment. As a result, the weak-beam segments are oversampled because weak-beam segments are longer than the strong-beam segments.

2. Surface classification is performed after all the beams are processed.

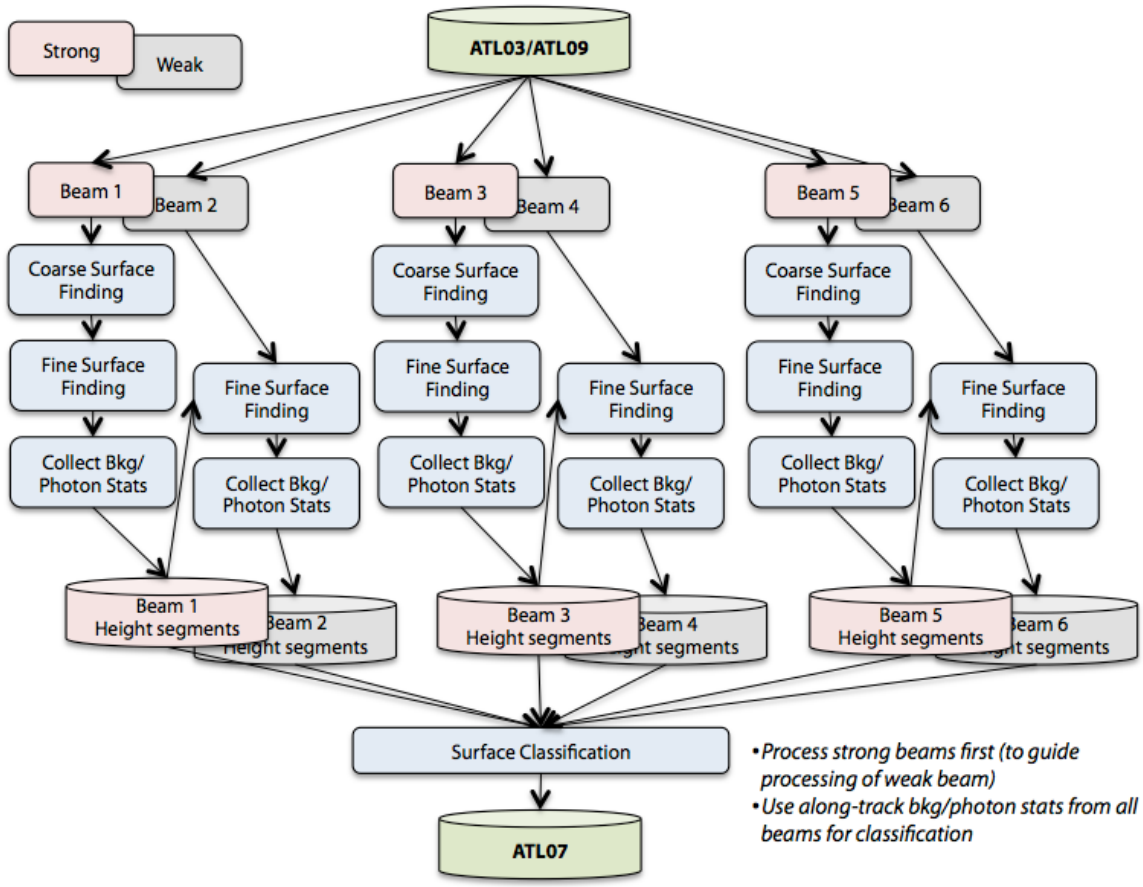

Figure 20 Flowchart: Multibeam architecture.

7.2 Product Coverage (ATL07 and ATL10)

In the initial development of the ATL07/10 sea ice products there was uncertainty as to how well the algorithm would perform in different regions (peripheral seas) and time periods. As such, a regional and time period filter was introduced to the algorithm, as described below. In this release (and earlier releases of data) no seasonal or regional filter was implemented due to the encouraging performance of the algorithm across both hemispheres. We thus currently apply no regional or seasonal filtering, other than the concentration filter (<15% for ATL07 and <50% for ATL10) but provide the information here for possible future implementation following further validation efforts.

We divide the Northern and Southern Hemisphere ice covers into eleven and five regions, respectively (see Fig. 21, Table 10 and Table 11). We define the ice margin (MIZ – marginal ice zone) as that part of the ice cover with <15% ice concentration, as defined by daily fields of ice concentration from satellite passive microwave brightness temperatures.

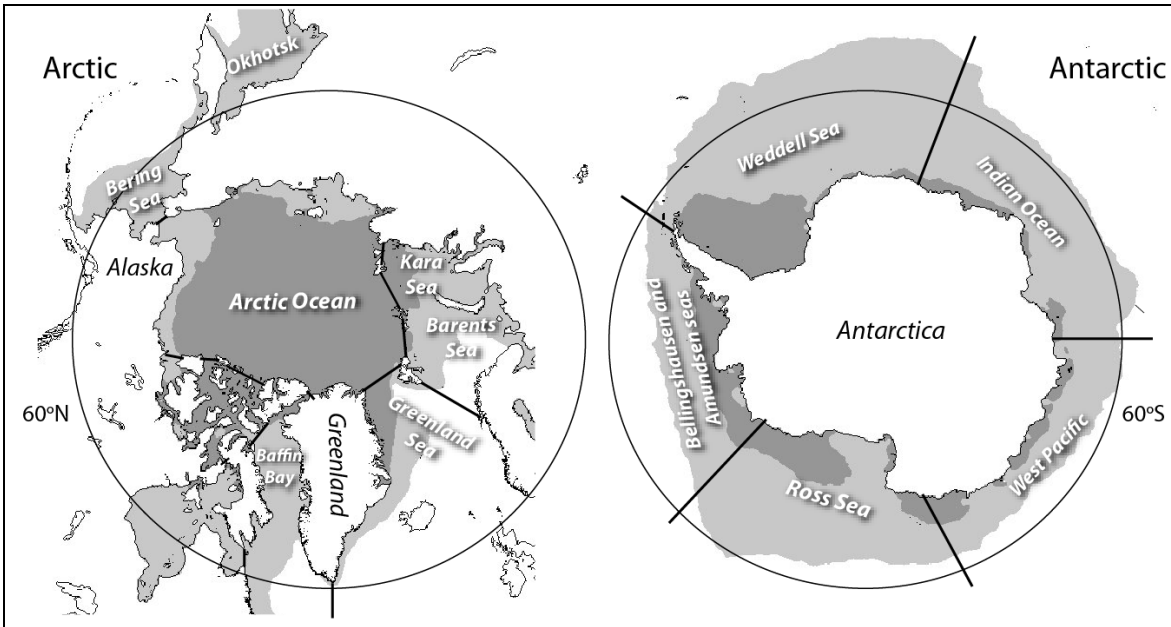

Figure 21 Northern and Southern Hemisphere ice covers.

7.2.1 Northern Hemisphere Sea Ice Cover

Table 16 Coverage of ICESat-2 Products in the Northern Hemisphere

Northern Hemisphere		**Seasons**			
		Winter Oct-Apr	**Transition May-Jun**	**Summer Jul-Aug**	**Transition Sep**
Arctic Ocean Canadian Arctic Archipelago Greenland Sea Barents Sea Kara Sea Bering Sea Baffin Bay/Davis Str Baltic Sea	Interior	ATL07 ATL10	ATL07 ATL10	ATL07 ATL10	ATL07 ATL10
	MIZ	ATL07 ATL10	ATL07 ATL10	ATL07 ATL10	ATL07 ATL10
Sea of Okhotsk (extrapolar; high background rates)	Interior	ATL07 ATL10	ATL07 ATL10	ATL07 ATL10	ATL07 ATL10
	MIZ	ATL07 ATL10	ATL07 ATL10	ATL07 ATL10	ATL07 ATL10

7.2.2 Southern Hemisphere Sea Ice Cover

Table 17 Coverage of ICESat-2 Products in the Southern Hemisphere

Southern Hemisphere		**Seasons**			
		Winter May-Oct	**Transition Nov-Dec**	**Summer Jan-Mar**	**Transition Apr**
Weddell Sea, Bellingshausen/Amundsen Seas, Ross Sea, Western Pacific Sector, Indian Ocean Sector	Interior	ATL07 ATL10	ATL07 ATL10	ATL07 ATL10	ATL07 ATL10
	MIZ	ATL07 ATL10	ATL07 ATL10	ATL07 ATL10	ATL07 ATL10

.

7.2.3 Seasonal and Regional definitions

The seasonal descriptors of "Winter", "Spring transition", "Summer" and "Fall transition" are used for both hemispheres. The seasonal boundaries are defined by start and stop days as follows (the ice classification control parameters in Table 7 have seasonal dependencies that are also defined by start and stop days for both the Arctic and Antarctic regions) :

	Arctic start	Arctic stop	Antarctic start	Antarctic stop
Winter	305 (Nov1)	120 (Mar31)	91 (Apr1)	273 (Sep30)
Spring transition	121 (Mar31)	165 (Jun14)	274 (Oct1)	318 (Nov14)
Summer	166 (Jun15)	257 (Sep14)	319 (Nov15)	31 (Jan31)
Fall transition	258 (Sep15)	304 (Oct31)	32 (Feb1)	90 (Mar31)

Shapefiles are geographical regions defined to control the intervals for processing of different regions of the ice-covered oceans. In the Arctic, we define 11 shapefiles, including the Central Arctic Ocean and lower latitude regions (Bering Sea, Sea of Okhotsk, Kara Sea, Barents Sea, Greenland/Norwegian Sea, Labrador Sea, Hudson Bay, Foxe Basin, Baffin Bay, the Canadian Archipelago). In the Antarctic, we define 5 shapefiles: Ross Sea, Bellingshausen/Amundsen Sea, Weddell Sea, Antarctic / Indian Ocean, Antarctic / West Pacific Ocean.
The shapefiles will be used to control the production and the distribution of the ATL10 products. The Central Arctic Ocean will always be activated and creating ATL10 products. As the period after launch progresses, Antarctic and other Arctic and sub-Arctic regions will be analyzed and parameters adjusted so that valid ATL10 products for those regions can be created and distributed. The following table defines the start and stop days for ATL10 processing within each region:

	start	stop
Central Arctic	1 (Jan1)	365 (Dec31)
Bering Sea	305 (Nov1)	166 (Jun15)
Sea of Okhotsk	319 (Nov15)	152 (Jun1)
Kara Sea	1 (Jan1)	365 (Dec31)
Barents Sea	1 (Jan1)	365 (Dec31)
Greenland/Norwegian Sea	1 (Jan1)	365 (Dec31)
Labrador Sea	274 (Oct1)	213 (Aug1)
Hudson Bay	274 (Oct1)	213 (Aug1)
Foxe Basin	274 (Oct1)	213 (Aug1)
Baffin Bay	1 (Jan1)	365 (Dec31)
Canadian Archipelago	1 (Jan1)	365 (Dec31)
Ross Sea	1 (Jan1)	365 (Dec31)
Bellingshausen/Amundsen Sea	1 (Jan1)	365 (Dec31)
Weddell Sea	1 (Jan1)	365 (Dec31)
Antarctic / Indian Ocean	1 (Jan1)	365 (Dec31)
Antarctic / West Pacific Ocean	1 (Jan1)	365 (Dec31)

7.3 Parameters Required from ATLAS

7.3.1 System impulse response

This information comes from the ATL03 product.

Table 18 Parameters from ICESat-2

Parameters	Sampling	Source
System Impulse Response	1 cm	ATL03 product

7.4 Parameters from Ancillary Sources

The parameters listed in Table 18 are from external sources.

7.4.1 Gridded ice concentration

Daily 25 km gridded ice concentration fields from the Near-Real-Time NOAA/NSIDC Climate Data Record of Passive Microwave Sea Ice Concentration (https://nsidc.org/data/g10016).

7.4.2 Mean Sea Surface (Arctic and Antarctic)

2.5 km gridded data provided as a static field (see Appendix F).

7.4.3 Distance from Land Maps (Arctic and Antarctic)

2.5 km gridded data provided as a static field (see Appendix F).

Table 19 Parameters from Ancillary Sources

Parameters	Sampling	Source
Gridded Ice Concentration (*IC*)	Daily (25 km) – Northern and Southern hemisphere ice covers	NOAA/NSIDC CDR (https://nsidc.org/data/g10016)
Mean sea surface (MSS)	2.5 km gridded data. Static, unless there are needed product updates – which are expected to be infrequent.	CryoSat-2/DTU13 (see Table 24 in Appendix F)
Distance to Land Map	2.5 km gridded data. Static.	(see Table 25 in Appendix F)

8 BROWSE PRODUCTS

8.1 ATL07

8.1.1 Line plots (beams)

- height of segment
- width of best fit Gaussian
- height segment surface type
- length of segment
- height fit quality flag
- ice concentration
- Apparent Surface Reflectivity (25 Hz)

8.1.2 Histogram

- height of segment
- width of best fit Gaussian
- length of segment

8.2 ATL10

8.2.1 Line plots (beams)

- estimate of freeboard height for the entire swath
- estimate of freeboard height for individual beams
- Number of leads (per swath)
- Number of leads (per beam)
- reference mean surface (per swath)
- reference mean surface (per beam)

8.2.2 Histogram

- freeboard height distribution (swath)
- freeboard height distribution (per beam)
- distribution of reference mean surface (swath)
- distribution of reference mean surface (per beam)

8.3 ATL20

Image of monthly composite of freeboard.

8.4 ATL21

Image of monthly composite of SSH anomalies.

9 DATA FILTERING

9.1 Filtering of granules

ATL07 and ATL10 granules can 'fail' for a number of reasons. Failed granules are generated by SIPS but not sent to the NSIDC for public dissemination. An ATL10 granule is not generated if the underlying ATL07 granule has failed. The pass/fail flag is given in the /quality_assesment/qa_granule_pass_fail variable (0 = fail, 1 = pass) and the reason in the qa_granule_fail_reason flag variable (0 = no failure, 1 = processing error, 2 = insufficient output). An insufficient output fail is determined by the following: i) ATL07 granules with less than a certain number of valid height segments, and ii) ATL10 granules with less than a certain number of valid freeboard segments or (*new for rel005 data production)* 10 km reference surface heights (as summarized in Table 20). Note that failed granules are not sent to the NSIDC (but have been produced by SIPS and can be requested through the NSIDC).

Table 20 Data filters (ATL07, ATL10).

Filter	threshold	ATL07	ATL10
Minimum # ATL07 valid height segment count (total of the 3 strong beams)	1500	Fail	Not generated
Minimum # ATL10 valid freeboard segment count (total of the 3 strong beams)	1500	-	Fail
Minimum # ATL10 reference surface heights (not interpolated, total from the 3 strong beams)	*9*	-	*Fail*

In R001 to R003 data, manual QA checks were carried out post-production to hold granules undergoing calibration scans (e.g. Round-The-World (RTW) scans) – i.e. not publicly disseminate these through the NSIDC. As of rel005, this information was integrated into ATL03 and used by the sea ice products to invalidate the freeboards during the off-pointing/calibration maneuver as explained in Section 4.3.1.5. Please also see the Known Issues document on the NSIDC ATL07/10 data portal for updated information about the data hold procedure and calibration scans/off-pointing issues.

Finally, ATL20 and ATL21 are manually QAd before dissemination to ensure complete ingestion of ATL10 input data.

9.2 Test Data

This section describes the test data sets that have been derived to verify the performance of the ATL07 surface-finding code.

Table 21 Current Test Data Sets

Instrument	Date	Location
MABEL	April 2012	Nares Strait/North of Greenland/Fram Strait
MABEL	July 2014	Beaufort Sea

10 CONSTRAINTS, LIMITATIONS, AND ASSUMPTIONS

In this section, we list the notable constraints, limitations, and assumptions (germane to this sea ice ATBD) that affect the coverage, quality and interpretation of the retrievals based on our current understanding of the instrument and geophysics of sea ice. These topics have been discussed throughout the ATBD. Over sea ice, two parameters are derived directly from the ATLAS acquisitions (surface height and type) and the brief remarks that follow focus on these variables. All other parameters (freeboard and thickness) that stem from these estimates are not discussed.

10.1 Constraints

The following are constraints imposed by the inherent capability of the instrument.

- At 532 nm, clouds will affect visibility of the sea ice cover in the Arctic and Southern Oceans. Based on ICESat-1 observations, the reduction in coverage will be significant during the summer after the spring-to-summer seasonal transitions.
- Height retrievals. The first-photon bias is an inherent problem with the photon-counting detectors selected for ATLAS. Even though the biases are at centimeter to sub-centimeter levels for most sea ice surfaces, the effect is large for intense pulses and for pulses from flat surfaces where the return energy is concentrated over a short duration. Procedures (with certain assumptions about the return – see below) are available to correct for these biases.

10.2 Limitations

These limitations stem from on our current understanding of the altimetric returns from the sea ice cover.

- Height retrievals. Quantification of the impact of subsurface scattering on height retrievals due to multiple scattering within the ice or snow volume remains to be addressed. For sea ice, these effects are mitigated in the surface-finding process via windowing of the photon height distributions to avoid potential tails in the distributions. Since snow properties may not be known at the time of ATLAS acquisitions, determination of a height correction due to subsurface scattering (if so desired) must be determined independently using external information about the snow cover, and the effectiveness of such an approach remains to be demonstrated.
- Surface Classification. Several surface types are provided by the retrieval procedure but the unambiguous identification of the sea surface in the height segments is critical to the subsequent calculations of freeboard and ice thickness. The design of the surface type retrieval procedure has focused on sea surface signatures and thus there are uncertainties associated with the labeling of the other ice types.

10.3 Assumptions

These are assumptions made by the retrieval routines.

- Height retrievals.
  1) The surface-finding procedure assumes that the sampled photon heights (or surface heights) are random realizations from a normal distribution. Potentially, there could be mixture distributions within the photon aggregate and these are indicated in the higher moments of the surface photon cloud.

2) The first-photon bias correction assumes that the photon statistics at a given height remains stationary over the time interval used to construct the photon distribution. For sea ice, where mixture distributions are expected due to variability in surface types over short length scales (especially near the ice margins), these corrections (even though small in most cases) may not be effective.

11 REFERENCES

Abdalati, W., and Coauthors, 2010: The ICESat-2 laser altimetry mission. Proc. IEEE, 98, 735–751.

Abshire, J.B., X. Sun, H. Riris, J.M. Sirota, J.F. McGarry, S. Palm, D. Yi, P. Liiva, 2005: Geoscience Laser Altimeter System (GLAS) on the ICESat Mission: On-orbit measurement performance, Geophy. Res. Letts, 32, L21S02.

Bilmes, J. A. 1998: A Gentle Tutorial of the EM Algorithm and its Application to Parameter Estimation for Gaussian Mixture and Hidden Markov Models, International Computer Science Institute, TR-97-021.

Dempster, A. P., N. M. Laird, and D. B. Rubin, 1977: Maximum likelihood from incomplete data via the em algorithm. Journal of the Royal Statistical Society: Series B, 39(1):1–38.

Grenfell, T. C., and D. K. Perovich, 1984:, Spectral albedos of sea ice and incident solar irradiance in the Southern Beaufort Sea, J. Geophys. Res., 89, 3573– 3580.

Kwok, R., G. F. Cunningham, H. J. Zwally, and D. Yi (2006), ICESat over Arctic sea ice: Interpretation of altimetric and reflectivity profiles, J. Geophys. Res., 111, C06006, doi:10.1029/2005JC003175.

Kwok, R., G. F. Cunningham, M. Wensnahan, I. Rigor, H. J. Zwally, and D. Yi, 2009: Thinning and volume loss of Arctic sea ice: 2003-2008, J. Geophys. Res., doi:10.1029/2009JC005312.

Kwok, R., T. Markus, J. Morison, S. P. Palm, T. A. Neumann, K. M. Brunt, W. B. Cook, D. W. Hancock, and G. F. Cunningham. (2014), Profiling sea ice with a Multiple Altimeter Beam Experimental Lidar (MABEL), J. Atmos. Oceanic. Technol., 31(5), doi: 10.1175/JTECH-D-13-00120.1.

Kwok, R., and J. Morison (2015), Sea surface height and dynamic topography of the ice-covered oceans from CryoSat-2: 2011–2014, J. *Geophys. Res. Oceans*, 121, doi:10.1002/2015JC011357

Kwok, R., G. F. Cunningham, J. Hoffmann, and T. Markus (2016), Testing the ice-water discrimination and freeboard retrieval algorithms for the ICESat-2 mission, *Remote Sens. Environ.*, 183, 13-25, doi: 10.1016/j.rse.2016.05.011.

McGill, M., T. Markus, V. S. Scott, T. Neumann., 2013: The Multiple Altimeter Beam Experimental Lidar (MABEL): An Airborne Simulator for the ICESat-2 Mission, J. Atmos. Oceanic. Technol., 30(2), doi: 10.1175/JTECH-D-12-00076.1.

Perovich, D. K., T. C. Grenfell, B. Light, and P. V. Hobbs, 2002: Seasonal evolution of the albedo of multiyear Arctic sea ice, J. Geophys. Res., 107(C10), 8044, doi:10.1029/2000JC000438.

Schutz, B.E., H.J. Zwally, C.A. Shuman, D. Hancock, and J.P. DiMarzio, 2005: Overview of the ICESat Mission, Geophy. Res. Letts, 32, L21S01.

Warren, S.G., R.E. Brandt and T.C. Grenfell 2006. Visible and near-ultraviolet absorption spectrum of ice from transmission of solar radiation into snow. Applied Optics, 45(21): 5320-5334.

Yang, Y., A, Marshak , S. P. Palm. T. Varanai, and W. J. Wiscombe, 2011: Cloud Impact on Surface Altimetry from a Spaceborne 532-nm Micropulse Photon-Counting Lidar: System Modeling for Cloudy and Clear Atmospheres, Trans. Geosci. Remote Sens., 49(12), doi: 10.1109/TGRS.2011.2153860.

Zwally, H. J., and Coauthors, 2011: Greenland ice sheet mass balance: Distribution of increased mass loss with climate warming; 2003-07 versus 1992-02. J. Glaciol., 57, 88–102.

List of Acronyms

ASAS	ATLAS Science Algorithm Software
ATBD	Algorithm Theoretical Basis Document
ATLAS	Advance Topographic Laser Altimeter System
CF	Center-of-Figure
CM	Center of Mass
CM	Configuration Manager
DAC	Dynamic Atmospheric Correction
DEM	Digital Elevation Model
DOT	Dynamic Ocean Topography
ECMWF	European Center for Medium-Range Weather Forecasts
EOSDIS	Earth Observing System Data and Information System
GEUS	Geological Survey of Denmark and Greenland
GLAS	Geoscience Laser Altimeter System
GLIMS	Global Land Ice Measurements from Space
GSFC	Goddard Space Flight Center
GMAO	Global Modeling and Assimilation Office
GMT	Greenwich Mean Time
GOCE	Gravity field and steady-state Ocean Circulation Explorer
GSHHG	Global Self-consistent, Hierarchical, High-resolution Geography database
GT	Ground Tracks
HDF	Hierarchical Data Format
IB	Inverted Barometer
IBCAO	The International Bathymetry Chart of the Arctic Ocean
ICESat-2	Ice, Cloud, and Land Elevation Satellite-2
IDL	Interactive Data Language
IERS	International Earth Rotation and Reference Systems
JPL	Jet Propulsion Laboratory
MABEL	Multiple Altimeter Beam Experimental Lidar
MDT	Mean Dynamic Topography
MIS	Management Information System
MOA	Mosaic of Antarctica
MODIS	Moderate Resolution Imaging Spectroradiometer
MSS	Mean Sea Surface
NASA	National Aeronautics and Space Administration
NCEP	National Center for Environmental Prediction
NSIDC	National Snow and Ice Data Center

OMCT	Ocean Model for Circulation and Tides
RFA	Request for Action
RGI	Randolph Glacier Inventory
RGT	Reference Ground Track
POD	Precision Orbit Determination
PPD	Precision Pointing Determination
PSO	ICESat-2 Project Science Office
RGT	Reference Ground Track
SCoRe	Signature Controlled Request
SDMS	Scheduling and Data Management System
SIPS	ICESat-2 Science Investigator-led Processing System
SLA	Sea Level Anomaly
SLP	Sea Level pressure
SLR	Satellite Laser Ranging
SSH	Sea Surface Height
TBD	To Be Determined
TMR	TOPEX Microwave Radiometer
TOPEX	Topography Experiment
UTC	Coordinated Time Universal

Glossary

This is not in alphabetical order.

Spots. The ATLAS instrument creates six spots on the ground, three that are weak and three that are strong, where strong is defined as approximately four times brighter than weak. These designations apply to both the laser-illuminated spots and the instrument fields of view. The spots are numbered as shown in Figures 22 and 23. At times, the weak spots are leading (when the direction of travel is in the ATLAS +x direction) and at times the strong spots are leading. However, the spot number does not change based on the orientation of ATLAS. The spots are always numbered with 1L on the far left and 3R on the far right of the pattern.

Laser pulse. Individual pulses of light emitted from the ATLAS laser are called laser pulses. As the pulse passes through the ATLAS transmit optics, this single pulse is split into 6 individual transmit pulses by the diffractive optical element. The 6 pulses travel to the earth's surface (assuming ATLAS is pointed to the earth's surface). Some attributes of a laser pulse are the wavelength, pulse shape and duration.

Laser Beam. The sequential laser pulses emitted from the ATLAS instrument that illuminate spots on the earth's surface are called laser beams. ATLAS generates 6 laser beams. The laser beam numbering convention follows the ATLAS instrument convention with strong beams numbered 1, 3, and 5 and weak beams numbered 2, 4, and 6 as shown in the figures.

Transmit Pulse. Individual pulses of light emitted from the ICESat-2 observatory are called transmit pulses. The ATLAS instrument generates 6 transmit pulses of light from a single laser pulse. The transmit pulses generate 6 spots where the laser light illuminates the surface of the earth. Some attributes of a given transmit pulse are the wavelength, the shape, and the energy. Some attributes of the 6 transmit pulses may be different.

Reflected Pulse. Individual transmit pulses reflected off the surface of the earth and viewed by the ATLAS telescope are called reflected pulses. For a given transmit pulse, there may or may not be a reflected pulse.

Photon Event. Some of the energy in a reflected pulse passes through the ATLAS receiver optics and electronics. ATLAS detects and time tags some fraction of the photons that make up the reflected pulse, as well as background photons due to sunlight or instrument noise. Any photon that is time tagged by the ATLAS instrument is called a photon event, regardless of source.

Reference Ground Track (RGT). The reference ground track (RGT) is the track on the earth at which a specified unit vector within the observatory is pointed. Under nominal operating conditions, there will be no data collected along the RGT, as the RGT is spanned by GT2L and GT2R (which are not shown in the figures, but are similar to the GTs that are shown). During spacecraft slews or off-pointing, it is possible that ground tracks may intersect the RGT. The precise unit vector has not yet been defined. The ICESat-2 mission has 1387 RGTs, numbered from 0001xx to 1387xx. The last two digits refer to the cycle number.

Cycle Number. Over 91 days, each of the 1387 RGTs will be targeted in the polar regions once. In subsequent 91-day periods, these RGTs will be targeted again. The cycle number tracks the number of 91-day periods that have elapsed since the ICESat-2 observatory entered the science orbit. The first 91-day cycle is numbered 01, the second 91-day cycle is 02, and so on. At the end of the first 3 years of operations, we expect the cycle number to be 12. The cycle number will be carried in the mid-latitudes, though the same RGTs will (in general) not be targeted more than once.

Sub-satellite Track (SST). The sub-satellite track (SST) is the time-ordered series of latitude and longitude points at the geodetic nadir of the ICESat-2 observatory. In order to protect the ATLAS detectors from damage due to specular returns, and the natural variation of the position of the observatory with respect to the RGT throughout the orbit, the SST is generally not the same as the RGT.

Ground Tracks (GT). As ICESat-2 orbits the earth, sequential transmit-pulses illuminate six ground tracks on the surface of the earth. The track width is approximately 10m wide. Each ground track is numbered, according to the laser spot number that generates a given ground track. Ground tracks are therefore always numbered with 1L on the far left of the spot pattern and 3R on the far right of the spot pattern.

Reference Pair Track (RPT). The reference pair track is the imaginary line half-way between the planned locations of the strong and weak ground tracks that make up a pair. There are three RPTs: RPT1 is spanned by GT1L and GT1R, RPT2 is spanned by GT2L and GT2R (and may be coincident with the RGT at times), and RPT3 is spanned by GT3L and GT3R. Note that this is the planned location of the midway point between GTs. We will not know this location very precisely prior to launch.

Pair Track (PT). The pair track is the imaginary line half way between the actual locations of the strong and weak ground tracks that make up a pair. There are three PTs: PT1 is spanned by GT1L and GT1R, PT2 is spanned by GT2L and GT2R (and may be coincident with the RGT at times), PT3 is spanned by GT3L and GT3R. Note that this is the actual location of the midway point between GTs, and will be defined by the actual location of the GTs.

Pairs. When considered together, individual strong and weak ground tracks form a pair. For example, GT2L and GT2R form the central pair of the array. The pairs are numbered 1 through 3: Pair 1 is comprised of GT1L and GT1R, pair 2 is comprised of GT2L and GT2R, and pair 3 is comprised of GT3L and 3R.

Along-track. The direction of travel of the ICESat-2 observatory in the orbit frame is defined as the along-track coordinate, and is denoted as the +x direction. The positive x direction is therefore along the Earth-Centered Earth-Fixed velocity vector of the observatory. Each pair has a unique coordinate system, with the +x direction aligned with the Reference Pair Tracks.

Across-track. The across-track coordinate is y and is positive to the left, with the origins at the Reference Pair Tracks.

Segment. An along-track span (or aggregation) of received photon data from a single ground track or other defined track is called a segment. A segment can be measured as a time duration (e.g. from the time of the first received photon to the time of the last received photon), as a distance (e.g. the distance between the location of the first and last received photons), or as an accumulation of a desired number of photons. Segments can be as short or as long as desired.

Signal Photon. Any photon event that an algorithm determines to be part of the reflected pulse.

Background Photon. Any photon event that is not classified as a signal photon is classified as a background photon. Background photons could be due to noise in the ATLAS instrument (e.g. stray light, or detector dark counts), sunlight, or mis-classified signal photons.

h_.** Signal photons will be used by higher-level products to determine height above the WGS-84 reference ellipsoid, using a semi-major axis (equatorial radius) of 6378137m and a flattening of 1/298.257223563. This can be abbreviated as 'ellipsoidal height' or 'height above ellipsoid'. These heights are denoted by h; the subscript ** will refer to the specific

algorithm used to determine that elevation (e.g. is = ice sheet algorithm, si = sea ice algorithm, etc…).

Photon Cloud. The collection of all telemetered photon time tags in a given segment is the (or a) photon cloud.

Background Count Rate. The number of background photons in a given time span is the background count rate. Therefore, a value of the background count rate requires a segment of received photons and an algorithm to distinguish signal and background photons.

Noise Count Rate. The rate at which the ATLAS instrument receives photons in the absence of any light entering the ATLAS telescope or receiver optics. The noise count rate includes received photons due to detector dark counts or stray light from within the instrument.

Telemetry band. The subset of received photons selected by the science algorithm on board ATLAS to be telemetered to the ground is called the telemetry band. The width of the telemetry band is a function of the signal to noise ratio of the data (calculated by the science algorithm onboard ATLAS), the location on the earth (e.g. ocean, land, sea ice, etc…), and the roughness of the terrain, among other parameters. The widths of telemetry bands are adjustable on-orbit. The telemetry band width is described in ATL03 or the ATLAS Flight Science Receiver Algorithms document. The total volume of telemetered photon events must meet the data volume constraint (currently 577 GBits/day).

Window, Window Width, Window Duration. A subset of the telemetry band of received photons is called a window. If the vertical extent of a window is defined in terms of distance, the window is said to have a width. If the vertical extent of a window is defined in terms of time, the window is said to have a duration. The window width is always less than or equal to the telemetry band.

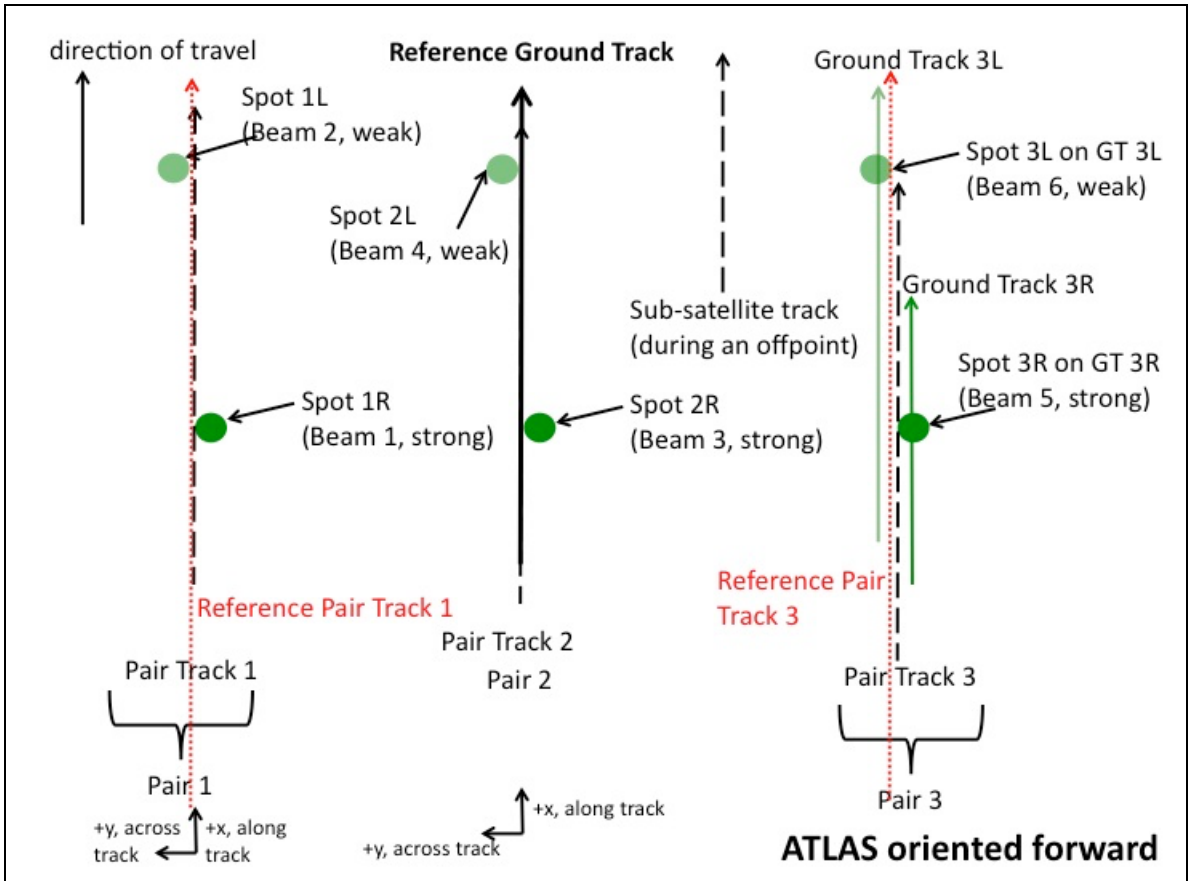

Figure 22 Spot and track naming convention with ATLAS oriented in the forward (instrument coordinate +x) direction.

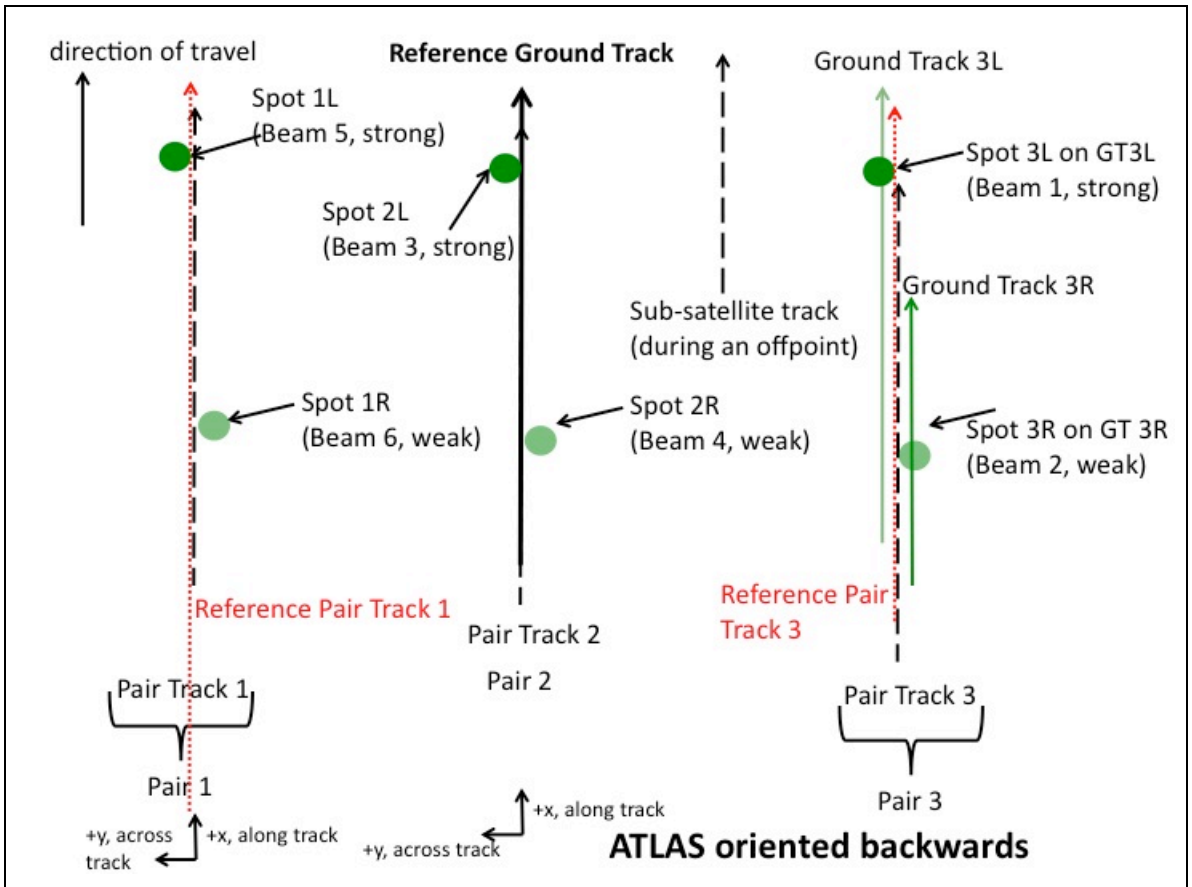

Figure 23 Spot and track naming convention with ATLAS oriented in the backward (instrument coordinate -x) direction.

APPENDIX A: Data dictionaries

ATL07 Data Dictionary can be found in:
https://nsidc.org/sites/nsidc.org/files/technical-references/ICESat2_ATL07_data_dict_v005.pdf
ATL10 Data Dictionary can be found in:
https://nsidc.org/sites/nsidc.org/files/technical-references/ICESat2_ATL10_data_dict_v005.pdf
ATL20 Data Dictionary can be found in:
https://nsidc.org/sites/nsidc.org/files/technical-references/ICESat2_ATL20_data_dict_v003.pdf
ATL21 Data Dictionary can be found in:
https://nsidc.org/sites/nsidc.org/files/technical-references/ICESat2_ATL21_data_dict_v002.pdf

APPENDIX B: Expectation-Maximization (EM) Procedure

<u>EM algorithm for estimating the parameters of two-component normal mixtures</u>
The EM algorithm estimates the parameters of a two-component normal mixture that best describe a distribution of random variables (Dempster et al., 1977; Bilmes, 1998).
The two-component mixture model:

$$f(x_i) = \alpha\phi_1(x_i;\mu_1,\sigma_1) + (1-\alpha)\phi_2(x_i;\mu_2,\sigma_2)$$

$$\phi_i(x;\mu_i,\sigma_i) = \frac{1}{\sqrt{2\pi}\sigma_i} e^{\frac{-(x-\mu_i)^2}{2\sigma_i^2}} \quad \text{(Normal distribution)}$$

The EM steps to compute the parameters of the mixture model with T random variates x_t $(\alpha,\mu_1,\sigma_1,\mu_2,\sigma_2)$ are:

1. Initialize with: $\alpha,\mu_1,\sigma_1,\mu_2,\sigma_2$.
2. Expectation (**E**) step: compute:

$$\gamma_t = \frac{\alpha\phi_1(x_t;\mu_1,\sigma_1)}{\alpha\phi_1(x_t;\mu_1,\sigma_1) + (1-\alpha)\phi_2(x_t;\mu_2,\sigma_2)}$$

$$for\ t = 1,\ldots,T.$$

3. Maximization (**M**) step. compute:

$$\mu_1 = \frac{\sum_{t=1}^{T}\gamma_t x_t}{\sum_{t=1}^{T}\gamma_t}, \quad \sigma_1^2 = \frac{\sum_{t=1}^{T}\gamma_t (x_t-\mu_1)^2}{\sum_{t=1}^{T}\gamma_t},$$

$$\mu_2 = \frac{\sum_{t=1}^{T}(1-\gamma_t)x_t}{\sum_{t=1}^{T}(1-\gamma_t)}, \quad \sigma_2^2 = \frac{\sum_{t=1}^{T}(1-\gamma_t)(x_t-\mu_2)^2}{\sum_{t=1}^{T}(1-\gamma_t)}, \textit{and}$$

$$\alpha = \sum_{t=1}^{T}\frac{\gamma_t}{T}.$$

Iterate the **E** and **M** steps until the parameters converge.

APPENDIX C: Construction of table $(\tilde{g})$ to correct biases Δh_{corr} due to skews in the height distributions

In the table $\tilde{g}$, the corrections Δh_{corr} are expressed as a function of the observed distribution parameters – $\tilde{\alpha}, \Delta\tilde{\mu}, \tilde{\sigma}_1, \tilde{\sigma}_2$ (two-component mixture) – from the Expectation-Maximization procedure described in Appendix C.

There are two sets of steps in the construction of the table $\tilde{g}(\tilde{\alpha}, \Delta\tilde{\mu}, \tilde{\sigma}_1, \tilde{\sigma}_2)$:

1. Compute the differences between the estimated heights ($\tilde{h}$ - obtained using the surface finding scheme described in this ATBD) and the mean heights $\overline{h}_{2G}$ of a mixture of two Gaussians ($\alpha, \mu_1, \sigma_1, \mu_2, \sigma_2$) used to model the skewed distributions. These differences are then tabulated as a function of the observed parameters $(\tilde{\alpha}, \Delta\tilde{\mu}, \tilde{\sigma}_1, \tilde{\sigma}_2)$ of the skewed distribution estimated by the Expectation-Maximization procedure, i.e., $\Delta h_{2G} = \overline{h}_{2G} - \tilde{h} = g(\tilde{\alpha}, \Delta\tilde{\mu}, \tilde{\sigma}_1, \tilde{\sigma}_2)$. The set of parameters ($\alpha, \mu_1, \sigma_1, \mu_2, \sigma_2$) is not directly observable because the mixtures have been convolved with the system impulse response.

   In more detail, the table $g(\tilde{\alpha}, \Delta\tilde{\mu}, \tilde{\sigma}_1, \tilde{\sigma}_2)$ is constructed as follows. For a set of $\alpha, \mu_1, \sigma_1, \mu_2, \sigma_2$ $(where\ \alpha : [0.1, 0.9];\ \Delta\mu : [-1.5, 0]m;\ \sigma_1, \sigma_2 : [0.0, 0.8]m)$:

   a. Convolve the two-component mixture distribution $f(x)$ with the system impulse response, viz:
   $s_{2G}(h) = s_t(h) * f(h)$, where
   $f(x) = \alpha\phi_1(x; \mu_1, \sigma_1) + (1-\alpha)\phi_2(x; \mu_2, \sigma_2)$ and $\overline{h}_{2G} = \alpha\mu_1 + (1-\alpha)\mu_2$

   b. Find the surface height ($\tilde{h}$) of the mixture distribution, $s_{2G}(h)$, using the surface finding routine described in Section 4 of this ATBD.

   c. Use the Expectation-Maximization procedure to provide the estimated two-component parameters ($\tilde{\alpha}, \tilde{\mu}_1, \tilde{\sigma}_1, \tilde{\mu}_2, \tilde{\sigma}_2$) of $s_{2G}(h)$. (See Appendix C)
   (Note that, in general, $(\tilde{\alpha}, \tilde{\mu}_1, \tilde{\sigma}_1, \tilde{\mu}_2, \tilde{\sigma}_2) \neq (\alpha, \mu_1, \sigma_1, \mu_2, \sigma_2)$ because of the convolution process).

   d. Compute $\Delta h_{2G} = \overline{h}_{2G} - \tilde{h}$.

   The result is a table of $\Delta h_{2G} = g(\tilde{\alpha}, \Delta\tilde{\mu}, \tilde{\sigma}_1, \tilde{\sigma}_2)$.

2. Weigh the corrections ($\overline{h}_{2G} - \tilde{h}$) to account for the transition from a single Gaussian (negative-skewed due to system impulse response) to two Gaussian mixtures:

$$\Delta h_{corr} = \Psi(\tilde{\alpha})\tilde{g}(\tilde{\alpha}, \Delta\tilde{\mu}, \tilde{\sigma}_1, \tilde{\sigma}_2)$$

   where $\Psi(\tilde{\alpha}) = \dfrac{1}{1 + e^{-\beta(\tilde{\alpha})}}$ *and* $\beta(\tilde{\alpha}) = \left(\dfrac{\tilde{\alpha} - \tilde{\alpha}_o}{\tilde{\alpha}_1 - \tilde{\alpha}_o}\right)c^2 - c$

Value of Δh_{corr} is computed using quadrilinear interpolation of the table $\tilde{g}(\tilde{\alpha}, \Delta\tilde{\mu}, \tilde{\sigma}_1, \tilde{\sigma}_2)$.

APPENDIX D: Source/calculation of background rates

Background rates (in MHz, with signal photons removed) are available in two IS-2 products:

1. ATL03 provides the following background rates:
   a) derived from the altimetry histograms (from up to 6 km range windows) constructed onboard at 200 Hz, or every 50-shots or minor frame (i.e., one-fourth of the Major Frame rate. (for strong and weak beams)
   b) derived from the altimetry histograms in the interval (up to 6 km range windows) formed onboard at 50 Hz, or every 200-shots; i.e. the Major Frame rate. (for strong and weak beams)
2. ATL09 provides background rates estimated from 400 shots (~280 m on the ground; 25 Hz) using a much wider atmospheric range window of [-1 km, 13 km]. (but only for strong beams)

These ATL03 and ATL09 rates are, in general, not aligned with the variable length height segments used by the surface-finding procedure in ATL07; thus these fixed-length rates are not entirely representative of the background rates of the variable length height segments discussed here.

Alternatively, we can compute the background rates with only the telemetered photon events used to form the height histogram for the sea-ice surface-finding procedure. The photon counts in the telemetered window of N_{pulses} can be converted into background rate estimates using the following equation:

$$B_S^{seg} = \frac{c(N_{aw} - N_{sw})}{2N_{pulses}(H_{aw} - H_{sw})}.$$

H_{aw} and H_{sw} are the heights of the telemetered and surface windows and N_{aw} and N_{sw} are the photon counts in the altimetry and surface windows. The accuracy of the background rate depends on the magnitude of the background rate itself and, in the case of the high-resolution segment, on the height of the window. We can use the high-resolution count only if there are enough photons to give a background rate accurate to 5% (*i.e.* if 400 background photons are detected in the window, the fractional Poisson counting error is $400^{-1/2}$, or about 20 counts, for an accuracy of 5%.) As the telemetered window size is much smaller (30 m to 1 km) than the onboard counting windows – even though that the number of shots can vary with the segment width used in our surface finding procedure – we have decided not to use this approach.

Since we know the minor frame to which a shot belongs, the background rate (B_{hs}) of a given height segment with N shots is calculated as follows:

$$B_{hs} = \frac{1}{N}\sum_{i=1}^{N} B_{mf}(s_i)$$

where B_{mf} is the background rate of the minor frame to which shot (s_i) belongs. Here, we use the 200-Hz background rates in ATL03. As a consequence, because of the 50-shot resolution, the background rate of a given height segment is not purely for that segment; there will be contributions of background from shots that do not belong to the height segment of interest.

APPENDIX E: Polar Stereographic Projection and Grid

We use NSIDC's polar stereographic projection for defining the planimetric grid for constructing the gridded products (https://nsidc.org/data/polar-stereo/ps_grids.html). The Cartesian grid is on a projection plane tangent to the Earth's surface at 70° northern and southern latitude. This planar grid is designed so that the cells at 70° latitude are exactly the defined nominal grid resolutions (shown below). For more information on cartographic characteristics, please refer to Snyder (1987). To minimize the planimetric distortion, NASA and NSIDC made this polar stereographic projection true (scale) at 70° rather than at the poles so that little or no distortion would occur in the marginal ice zone; this increases the distortion at the poles by ~6%.

The polar stereographic formulae for converting between latitude/longitude and x-y grid coordinates have been taken from map projections used by the U.S. Geological Survey (Snyder 1982). Several different ellipsoids were compared to the Hughes ellipsoid; and in each case, differences were less than 1 km over the SSM/I grids. Thus, it is an explicit requirement that an ellipsoid be used in processing the data. The ellipsoid used in the Hughes software assumes a radius of 3443.992 nautical miles or 6378.273 km and an eccentricity (e) of 0.081816153. To properly convert these coordinates to a polar stereographic grid, the conversion should assume the Hughes ellipsoid. The transformation equations and procedures can be found: https://nsidc.org/data/polar-stereo/ps_grids.html.

Polar stereographic grid definitions

1. Grid Dimensions
The grid size varies depending on the region, as shown in the table below.

Table 22 Grid Dimensions

Region	Nominal Gridded Resolution (km)	Columns	Rows
North	25/2.5	304/3040	448/4480
South	25/2.5	316/3160	332/3320

2. Grid Coordinates
The origin of each x, y grid is the respective pole. The approximate outer boundaries of the Northern and Southern grids are defined below. Corner points are the top left corner of the grid.

Table 23Northern and Southern Hemisphere Grid Coordinates

X (km)	Y (km)	Latitude (deg)		Longitude (deg)	
North					
-3850	5850	~30.98	corner	~168.35	corner
South					
-3950	4350	-39.23	corner	317.76	corner

3. SSM/I grid coverage maps

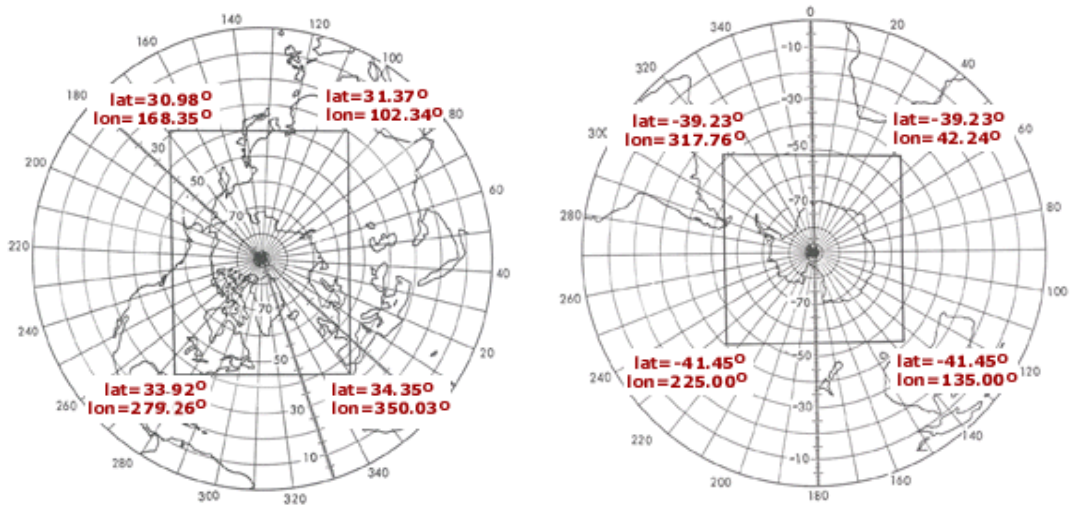

Figure 24 Coverage of SSM/I Grid.

Maslanik, J., and J. Stroeve. 1990. *DMSP SSM/I brightness temperature grids for the polar regions on CD-ROM: user's guide*. Boulder, CO USA: National Snow and Ice Data Center.

Snyder, J. P. 1987. *Map projections - a working manual.* U.S. Geological Survey Professional Paper 1395. U.S. Government Printing Office. Washington, D.C. 383 pages.

Snyder, J. P. 1982. Map Projections Used by the U.S. Geological Survey. U.S. Geological Survey Bulletin 1532.

APPENDIX F: Mean Sea Surface, Land Mask and Distance Map (Gridded fields)

Table 24 MSS of the Arctic and Southern Oceans (file)

	Specification	Remarks
Filename	Arctic: mss_arctic.2.5km Antarctic: mss_antarc.2.5km	MSS from CS-2 MSS (2011-2015, Kwok and Morison, 2015), gaps and lower- latitude marginal ice regions filled using the high resolution global DTU13 MSS product (Andersen et al., 2015). Smoothed using a 25 km Gaussian kernel.
Variable	Mean Sea Surface (MSS) height in meters above WGS-84 ellipsoid in a mean-tide system. Land/missing data: -888/-999	Reference ellipsoid bias correction applied before blending (WGS-84 for CryoSat-2 and Topex/Poseidon for DTU13).
Sample spacing	2.5 km	
File size	Arctic: 3040 x 4480 Antarctic: 3160 x 3320	Covers areas defined by DMSP SSM/I grid
Map projection	SSM/I Polar Stereographic	see Appendix E
Corner point (top left x,y)	Arctic: (-3848.75, 5848.75) km Antarctic: (-3948.75, 4348.75) km	Locations at center of corner bin
Format	Binary w/ ASCII header	Header: xul,yul,ni,nj,binsz,missval,landval Body: Real*4
Data	https://doi.org/10.5281/zenodo.4294047.	Converted to NetCDF for public access. Land/missing data: NaN.

Table 25 Land Mask and distance map

	Specification	Remarks
Filename	Arctic: distmap_arctic.2.5km Antarctic: distmap_antarc.2.5km	Created using 1km land mask
Variable	Distance of bin center to closest 1km land sample	Ocean: distance in kilometers Land code: -888. Missing code: -999.
Sample spacing	2.5 km	
File size	Arctic: 3040 x 4480 Antarctic: 3160 x 3320	Covers areas defined by DMSP SSM/I grid
Map projection	SSM/I Polar Stereographic	see Appendix E
Corner point (top left x,y)	Arctic: (-3848.75, 5848.75) km Antarctic: (-3948.75, 4348.75) km	Locations at center of corner bin
Format	Binary w/ ASCII header	Header: xul,yul,ni,nj,binsz,missval,landval Body: Real*4

APPENDIX G: First Photon Bias

We use the system engineering tables supplied in the ATL03 to obtain the first-photon biases for given photon height distributions. The bias tables (in CAL-19) are accessed using the average dead time of the detectors (*fpb_avg_dt*), apparent width and apparent strength for a given photon height distribution. Width of the return (see below) is calculated as the time (or range) interval between the time of 10% cumulative energy and 90% cumulative energy. Strength is the average events/shot or photon rate of a given height segment. A procedure in ATL07 calculates the three parameters (width, strength, and average dead time of height distribution) for accessing the ATL03 first photon bias tables.

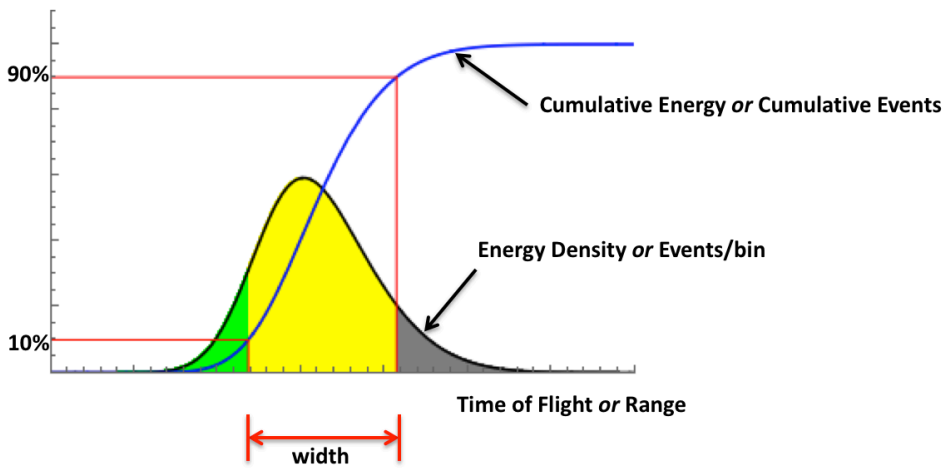

APPENDIX H: Organization of lead data in ATL10

The following diagram is presented to help the user understand the organization of the lead information in the ATL10 product. Although the swath segment (gold color in figure) and beam segment (light green in figure) lengths are fixed within a product, the number and size of the height segments vary within each beam. A sea surface height segment is a height segment with *ssh_flag* = 1. A lead is defined as a contiguous set of sea surface height segments. The lead information is contained in 3 levels of folders:
The group '/gtxx/leads' keeps track of all leads within a beam in along-track order. The parameter 'ssh_n' indicates the number of sea surface height segments which comprise the lead, while 'ssh_ndx' is the index which references the height segment id (found in '/freeboard_swath_segment/gtxx/swath_freeboard' and '/gtxx/freeboard_beam_segment/beam_freeboard) of the first sea surface height segment of the lead.
The '/freeboard_swath_segment' group contains information for a swath segment, which covers all beams. The lead heights across all beams are used to define a reference surface used in swath freeboard calculations. The data is organized using two parameters for each beam. Each element of 'fbswath_lead_n_gtxx' indicates the number of leads within each beam segment, while the 'fbswath_lead_ndx_gtxx' index points to the '/gtxx/leads' list location of

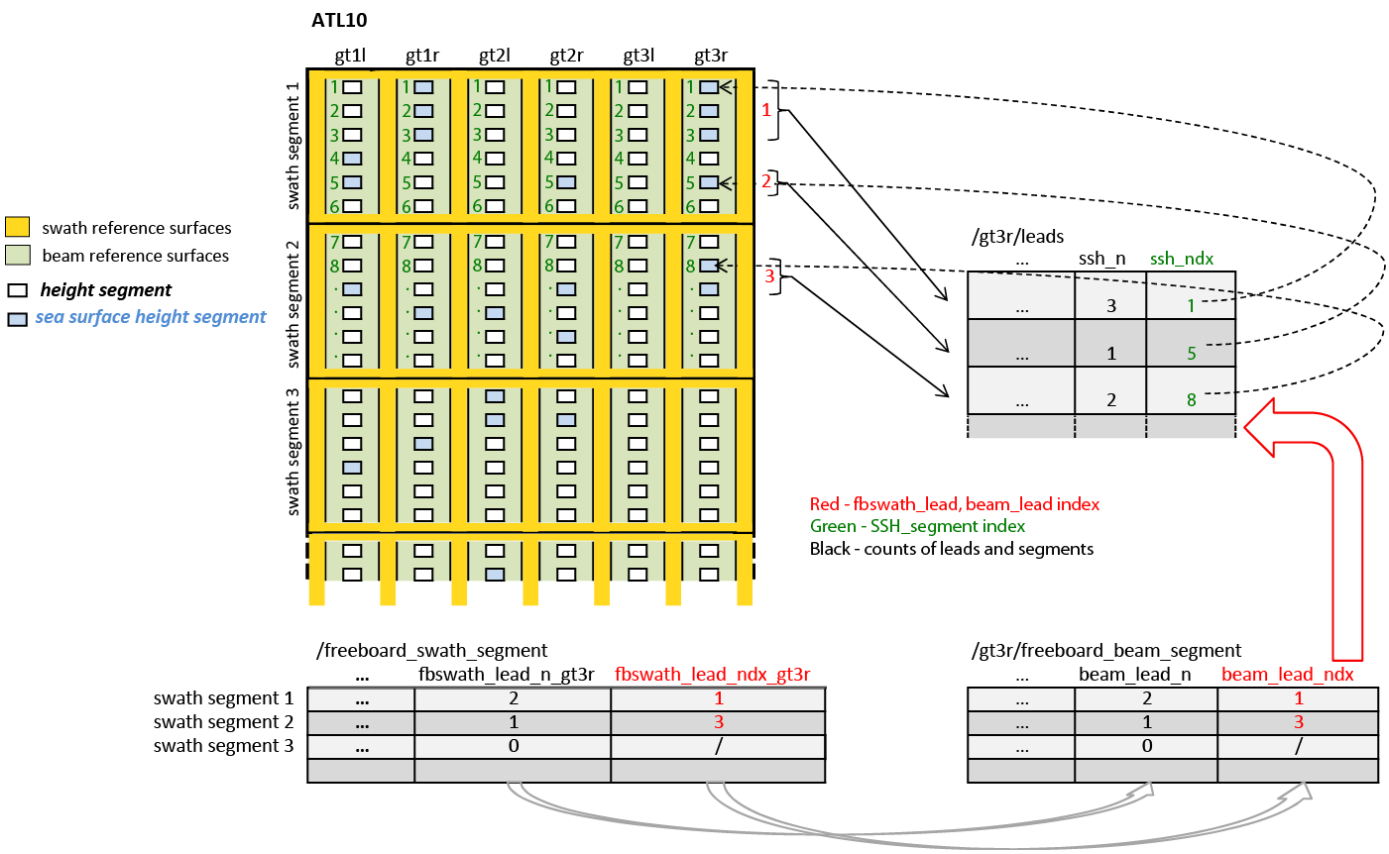

the first lead in each beam segment.
Similarly, the '/gtxx/freeboard_beam_segment' group contains information for a beam segment, where the lead heights across each beam segment are used to define a reference surface for the beam freeboard calculations. The parameter 'beam_lead_n' indicates the

number of leads within each beam segment, and the index 'beam_lead_ndx' points to the list location in '/gtxx/leads' of the first lead in each beam segment. Note: for corresponding beams, 'beam_lead_n' and 'beam_lead_ndx' will always be identical to 'fbswath_lead_n_gtxx' and 'fbswath_lead_ndx_gtxx' from the '/freeboard_swath_segment' group.

The times and locations of the freeboard swath (and beam) segment boundaries can be determined by using the parameter '/gtxx/freeboard_beam_segment/beam_freeboard/beam_refsurf_ndx'. This index identifies the swath segment that each height segment resides in: the time and location of the first and last height segments found within a freeboard swath or beam segment swath defines its boundaries.

APPENDIX I: Surface finding waveforms and TEP averaging

As discussed in Section 4.2.2, the expected return $s_e(h)$, from a surface with a Gaussian height distribution (width *w* or two times standard deviation) with a height offset of h_o (i.e., $G(h; h_o, w)$) is modeled as,

$$s_e(h; h_o, w) = s_t(h) * G(h; h_o, w),$$

where $s_t(h)$ is the system impulse response of the system and * is the convolution operator. That is, the expected return is assumed to be the convolution of the system impulse response with a Gaussian surface height distribution of width *w*.

The minimum in an error surface, $e^2(h_o, w)$, is used as the best estimate of the height offset, $\hat{h}_o$, of a surface with a Gaussian distribution of width $\hat{w}$ is written as,

$$\{\hat{h}_o, \hat{w}\} = \operatorname{argmin} e^2(h_o, w) \quad h_o \in [h_1, h_2] \quad w \in [w_1, w_2]$$

where the error surface is defined as the mean-squared difference between the normalized received signal (or height distribution), $\tilde{s}_{rec}(h)$, and the normalized expected return, $\tilde{s}_e(h)$,

$$e^2(h_o, w) = \frac{1}{N}\sum_N (\tilde{s}_{rec}(h_i) - \tilde{s}_e(h_i; h_o, w))^2$$

$$\sum_N \tilde{s}_{rec}(h_i) = 1$$

$$\sum_N \tilde{s}_e(h_i; h_o, w) = 1.$$

In order to allow for the narrower system impulse responses of the system when the photon rates are high (i.e., $s_t(h)$ is dependent on photon rate – the system is non-linear due to first photon bias), we model the narrower impulse response with,

$$s_t(h) = s'_{TEP}(h)$$

where $s'_{TEP}(h)$ is a height-scaled version of $s_{TEP}(h)$ (by a factor of two). $s_{TEP}(h)$ is the measured transmit echo pulse (TEP) that is available in ATL03. Effectively, the set of expected returns (or templates used in the surface finding) written as,

$$s_e(h; h_o, w) = s'_{TEP}(h) * G(h; h_o, w),$$

now covers the range of returns with responses that are narrower than those characterized by the nominal linear behavior characterized by the TEP.

Notes:

1) TEP Selection: The TEP used here will be based on the recommendation in ATL03.
2) Reminder: In the implementation, the height-scaled TEP (i.e., $s_t(h) = s'_{TEP}(h)$) should be re-centered at the centroid.